



저작자표시-비영리-변경금지 2.0 대한민국

이용자는 아래의 조건을 따르는 경우에 한하여 자유롭게

- 이 저작물을 복제, 배포, 전송, 전시, 공연 및 방송할 수 있습니다.

다음과 같은 조건을 따라야 합니다:



저작자표시. 귀하는 원저작자를 표시하여야 합니다.



비영리. 귀하는 이 저작물을 영리 목적으로 이용할 수 없습니다.



변경금지. 귀하는 이 저작물을 개작, 변형 또는 가공할 수 없습니다.

- 귀하는, 이 저작물의 재이용이나 배포의 경우, 이 저작물에 적용된 이용허락조건을 명확하게 나타내어야 합니다.
- 저작권자로부터 별도의 허가를 받으면 이러한 조건들은 적용되지 않습니다.

저작권법에 따른 이용자의 권리는 위의 내용에 의하여 영향을 받지 않습니다.

이것은 [이용허락규약\(Legal Code\)](#)을 이해하기 쉽게 요약한 것입니다.

[Disclaimer](#)

공학박사 학위논문

Biorheological Microfluidics and Energy Harvesting System

바이오유변학적 미세 유체 및
광전변환 시스템

2019년 2월

서울대학교 대학원
재료공학부
김민정

**Biorheological Microfluidics and
Energy Harvesting System**

**바이오유변학적 미세 유체 및
광전변환 시스템**

지도 교수 윤 재 루

이 논문을 공학박사 학위논문으로 제출함
2018년 12월

서울대학교 대학원
재료공학부
김 민 정

김 민 정 의 공학박사 학위논문을 인준함
2018년 12월

위 원 장 _____ (인)
부위원장 _____ (인)
위 원 _____ (인)
위 원 _____ (인)
위 원 _____ (인)

Biorheological Microfluidics and Energy Harvesting System

by

Min Jung Kim

Advisor: Professor Jae Ryoun Youn

February 2019

Department of Materials Science and Engineering
Graduate School
Seoul National University

Abstract

Biorheological Microfluidics and Energy Harvesting System

Min Jung Kim

Department of Materials Science and Engineering

The Graduate School

Seoul National University

Development of renewable energy sources has received much attention in recent years. Natural photosynthesis is a profound source of inspiration for energy conversion and storage systems because it harnesses the most abundant source of energy. Biological photovoltaics (BPV) are “living solar cells” that generates electric current from the photosynthetic activity of photoautotrophs. However, BPV demonstrated so far have achieved low efficiency. The objective of this dissertation is to overcome the limitations of the BPV by designing various energy harvesting systems based on biorheology knowledge.

Preliminary studies of BPV, the biorheological systems, are presented in chapter 2 and 3. In chapter 2, manipulation of photosynthetic organisms in a microfluidic device using extracellular polymeric substances (EPS) is remarked in order to select proper cells for energy harvesting. We extracted EPS from photosynthetic organisms and explored the non-Newtonian rheological behavior of EPS with the help of cell focusing and separation in confined microchannels. It was found that the cell showed a ‘self-ordering’ behavior in the ‘self-secreted’ substances. Moreover, autonomous cell-sorting was demonstrated.

In chapter 3, a new phenomenon, optorheology of photosynthetic bacterium suspended liquid operated by light was reported. It was revealed that the change in

the rheological feature of the cell suspension was induced by the generated electrons. The results showed that the photoelectrons generated by light enhanced the dispersion of the cyanobacteria in the solution, thus leading to a significant increment in the viscosity. For further understanding on this phenomenon, numerical simulation was carried out using finite element method. Overall, we reported that the rheological properties of the living cell suspension can be controlled by using light, which is a new area of rheology.

Based on the biorheology knowledge, the cyanobacterial flow battery (CFB) is reported in chapter 4, which provides a new direction for harvesting solar energy by using photosynthetic organisms in a sustainable manner. Developed CFB facilitates one species of photosynthetic organism having different concentrations of bicarbonate ions in the anode and cathode chambers without any mediator or metal. The cell is responsible for electron generation at the anode while the cell successfully acts as a terminal electron acceptor at the cathode. That is, both light and dark reactions of the photosynthesis are simultaneously utilized in this battery. The flow dependent performance of the device was evaluated by changing fluid flow conditions. When the cell solution is infused at 0.05 ml/min, the effective electron transfer to the electrode is observed, and 4.8 times higher power density is obtained than the case of the batch mode. For in depth understanding, the oxygen concentration in the cathode chamber is modeled using a finite element method. It is noteworthy that the eco-friendly energy conversion system was implemented by manipulating a metabolism of the cell.

Moreover, the bioinorganic hybrid systems were introduced to enhance the performance of BPV (chapter 5 and 6). In chapter 5, *Synechococcus* sp. – iron oxide nanoparticle – neodymium iron boride magnet complexes are designed to enable high performance via a long electron transfer conduit to the electrode. In the system, nanomaterials can convert light into electricity and transfer the photosynthetic electrons from the photosynthetic cells to external electrode. That is, bioinorganic hybrid system provides synergistic combination of a natural

photocatalyst and an artificial photocatalyst that leads to a high performance by forming effective electron transfer conduits to the electrode in a very short time. A conventional green LED bulb was turned on as the result of the energy harvesting. The approach introduced in this study can boost solar energy harvesting remarkably by combining natural photocatalysts with artificial ones.

In chapter 6, a novel broadband multiplex living solar cell consisting of *Synechocystis* sp. / Gold nanoparticle (Au NP) / Zinc oxide nanorod (ZnO NR) / ITO is developed. The hybrid nanostructure (Au NP / ZnO NR) acts as a stimulant for the photoactivity of the cell through the far-field scattering effect in the broadband region, leading to an anomalous enhanced bioinorganic photovoltaic cell. We obtained the peak power density of 6.148 mW/m² for the multiplex living solar cell, whereas *Synechocystis* sp. onto ITO electrode generated the peak power density of about 0.353 mW/m² only during the light irradiation. The power density is eventually increased by about 17.3-fold. The far-field scattering effects were verified by performing 3D numerical analysis of electromagnetic field. We envision that it provides a potential for enhanced performance of biophotovoltaics on conversion solar energy.

Keywords: Biorheological System, Photosynthetic Organism, Viscoelastic Fluid, Microfluidics, Optorheology, Suspension, Biophotovoltaics (BPV), Bioinorganic Hybrid System

Student Number: 2014-31051

CONTENTS

| | |
|--------------------------------------|-------|
| Abstract | i |
| List of Figures | vii |
| List of Tables | xviii |
| | |
| Chapter 1. Introduction | 1 |
| 1.1 Biorheological system | 1 |
| 1.2 Biophotovoltaics (BPV) | 4 |
| 1.3 Objectives of present work | 7 |
| 1.4 Bibliography | 9 |

Part I

Biorheological Microfluidics

| | |
|---|----|
| Chapter 2. Autonomous cell-sorting in a microfluidic device using self-secreted macromolecules | 12 |
| 2.1. Introduction | 12 |
| 2.2. Experimental | 15 |
| 2.3. Numerical analysis | 20 |
| 2.4. Results and discussion | 21 |
| 2.4.1. Characterization of the EPS | |

| | |
|-------------------|---|
| 21 | |
| 2.4.2. | Manipulation of particle in the microchannel 33 |
| 2.4.3. | ‘Self-ordering’ behavior in the ‘self-secreted’ substances 45 |
| 2.4.4. | Autonomous cell-sorting in the microchannel 49 |
| 2.5. | Conclusion 54 |
| 2.6. | Bibliography 55 |
| Chapter 3. | Optorheology of photosynthetic bacterium suspension 57 |
| 3.1. | Introduction 57 |
| 3.2. | Experimental 60 |
| 3.3. | Numerical analysis 65 |
| 3.4. | Results and disscusion 67 |
| 3.4.1. | Photosynthetic bacterium suspension..... 67 |
| 3.4.2. | Electrophoretic surface properties of photosynthetic bacterium suspension 69 |
| 3.4.3. | Rheological properties of photosynthetic bacterium suspension 75 |
| 3.4.4. | Network formation of the photosynthetic bacterium suspension under the AC-electric field 75 |

| | |
|------|--------------------|
| 80 | |
| 3.5. | Conclusion |
| 84 | |
| 3.6. | Bibliography |
| 85 | |

Part II
Biorheological Energy Harvesting System

| | | |
|-------------------|---|----|
| Chapter 4. | Sustainable cyanobacterial flow battery using simultaneous light-dependent and -independent reactions by cellular metabolism | |
| 87 | | |
| 4.1. | Introduction | 87 |
| 4.2. | Experimental | |
| 90 | | |
| 4.3. | Numerical analysis | |
| 95 | | |
| 4.4. | Results and discussion | |
| 100 | | |
| 4.4.1. | Design and construction of CFB | |
| 100 | | |
| 4.4.2. | Oxygen production at different bicarbonate concentrations | |
| 102 | | |
| 4.4.3. | Current and power analyses in the batch mode | |
| 105 | | |
| 4.4.4. | Effect of flow rate in CFB | |
| 107 | | |
| 4.4.5. | Numerical analysis of the mass transfer effect | |

| | |
|---|-----|
| | 112 |
| 4.5. Conclusion | 115 |
| 4.6. Bibliography | 116 |
| Chapter 5. Anomalous power enhancement of biophotovoltaic cell | |
| 118 | |
| 5.1. Introduction | 118 |
| 5.2. Experimental | |
| 121 | |
| 5.3. Results and discussion | |
| 131 | |
| 5.3.1. A new light-harvesting structure based on biological-inorganic hybrid system | |
| 131 | |
| 5.3.2. Characterization of the new light-harvesting structure | |
| 140 | |
| 5.3.3. Photoelectrochemical activity of the BPV | |
| 146 | |
| 5.3.4. Comparison with other BPV | |
| 150 | |
| 5.4. Conclusion | |
| 152 | |
| 5.5. Bibliography | |
| 153 | |
| Chapter 6. A broadband multiplex living solar cell | |
| 155 | |
| 6.1. Introduction | 155 |
| 6.2. Experimental | |

| | |
|--------|---|
| 160 | |
| 6.3. | Results and discussion |
| 170 | |
| 6.3.1. | Characterization of the photoanode |
| 170 | |
| 6.3.2. | Photoelectrical properties of photoanode |
| 172 | |
| 6.3.3. | Current and power analyses |
| 175 | |
| 6.3.4. | Viability of the <i>Synechosystis</i> onto the photoanode |
| 184 | |
| 6.3.5. | Broadband mutiplex living solar cell |
| 187 | |
| 6.4. | Conclusion |
| 189 | |
| 6.5. | Bibliography |
| 190 | |

| | |
|------------------------------|-----|
| Korean abstract | 192 |
|------------------------------|-----|

List of Figures

Figure 1.1 Microscale biorheological systems. (a) Centrifugal microfluidic system [3], (b) Electrokinetic platform for DNA [4], (c) Malaria infected erythrocyte separation system [5], (d) Robotic pump system [6], (e) DNA based focuser [7], (f) blood plasma separation system [9], (g) flow focusing structure [10], and (h) microfluidic system for manipulation in a single bovine capillary endothelial cell [11].

Figure 1.2 Schematic image of bioelectrochemical systems (BESs) [20]. (a) Microbial fuel cell (MFC), (b) Photosynthetic microbial fuel cell, (c) Complex photosynthetic microbial fuel cell, and (d) Biophotovoltaic system.

Figure 2.1 Schematic structure of the extracellular polymeric substances (EPS) secreted from *Chlorella vulgaris*. The biosynthetic macromolecules are mainly composed of polysaccharides, proteins and DNA, which are attached to the cell membrane. The components of EPS form three-dimensional networks providing mechanical stability of biofilms.

Figure 2.2 Schematic diagram of the microfluidic chips used in this study. (a) Schematic illustration for Elasto-inertial particle focusing under the EPS solution in a square channel. As the distance from the inlet increases, the Elasto-inertial particle focusing within the channel appears as a line. (b) Schematic illustration for Dean-coupled Elasto-inertial particle focusing under the EPS solution in a spiral channel. In a confined microchannel, different sized particles show different equilibrium positions at an outlet due to elastic force and Dean drag force.

Figure 2.3 Scanning electron micrograph of *Chlorella vulgaris* in biofilm. The scale bar denotes the length of 1 μm .

Figure 2.4 UV–Vis spectra of *Chlorella vulgaris* and EPS.

Figure 2.5 FT-IR spectrum of the EPS extracted from *Chlorella vulgaris*.

Figure 2.6 Rheological properties of the EPS for shear rates ranging from 1 to 1000 s^{-1} . The Carreau-Yasuda model was used to fit the EPS.

Figure 2.7 Storage modulus (G') and loss modulus (G'') of extracted EPS as a function of angular frequency.

Figure 2.8 Rheological measurements of the 0.9 wt% PEO solution. Viscosity and shear stress in the range of shear rate from 1 to 1000 s^{-1} .

Figure 2.9 Storage modulus (G') and loss modulus (G'') of the 0.9 wt% PEO solution as a function of angular frequency.

Figure 2.10 AFM images of the exopolysaccharide of the extracted EPS. The height of fibrils was in the range of 0.6 – 2 nm, which indicated the presence of a single molecular polysaccharide chain.

Figure 2.11 Lateral particle migration in the EPS solution. (a) Particle focusing of 6.27 μm fluorescent PS particles with a flow rate of 50 $\mu l hr^{-1}$. The hashed lines indicate the channel walls. The scale bar implies 50 μm . (b) Probability distribution function of the PS particles with a flow rate of 50 $\mu l hr^{-1}$.

Figure 2.12 Particle behavior of the different concentration of EPSs at a position of 5cm downstream from the inlet for 6.27 μm fluorescent PS particles with a flow rate of 50 $\mu l hr^{-1}$ ($Re = 0.0191$, $Wi = 22.2$). The scale bar is 50 μm .

Figure 2.13 Analysis of particle focusing phenomena. (a) Predicted distribution of the first normal stress difference (N_1) and schematic expression of forces exerted on a rigid particle under viscoelastic flows. (b) The value of the normalized first normal stress difference (N_1) shows symmetry at the cross-section of the channel.

Figure 2.14 (a) Particle focusing behavior of the EPSs in a straight channel at flow rates of 50 - 3000 $\mu l hr^{-1}$ ($Re = 0.0191 - 1.14$, $Wi = 22.2 - 1330$). The scale bar is 50 μm . (b) Probability distribution function of PS particles under flow rates of 50 – 3000 $\mu l hr^{-1}$ ($Re = 0.0191 - 1.14$, $Wi = 22.2 -$

1330).

Figure 2.15 (a) Particle focusing behavior of the 0.9 wt% of PEO solution in a straight channel at flow rates of 50 - 3000 $\mu\text{l hr}^{-1}$ ($Re = 0.0191 - 1.14$, $Wi = 22.2 - 1330$). The scale bar is 50 μm . (b) Probability distribution function of PS particles under flow rates of 50 - 3000 $\mu\text{l hr}^{-1}$ ($Re = 0.0191 - 1.14$, $Wi = 22.2 - 1330$).

Figure 2.16 Particle separation using the self-secreted biomaterials. Microscopic images for (a) the 3 μm PS particles and (c) the 10 μm PS particles in the EPSs solution with a flow rate of 400 $\mu\text{l hr}^{-1}$ ($Re = 0.122$, $Wi = 88.9$). Probability distribution functions for (b) the 3 μm PS particles and (d) the 10 μm PS particles after 1, 5 and 10 turns, showing particle focusing at the center and at the off-center, respectively. (e) Microscopic images illustrating the position and separation of the 3 and 10 μm PS particles at the outlet of the channel. (f) Probability distribution function of the 3 and 10 μm PS particles at the outlet.

Figure 2.17 (a) Experimental results of *Chlorella vulgaris* in the self-secreted EPSs with a flow rate of 50 $\mu\text{l hr}^{-1}$ ($Re = 0.0191$, $Wi = 22.2$). (b) Probability distribution function of *chlorella vulgaris* at a 5 cm position away from the entrance, showing cell focusing at the center. (c) Schematic illustration of the force balance in the cross-section of channel when *Chlorella vulgaris* migrates under viscoelastic flow. (d) Experimental results of PS particles in the EPS with a flow rate of 50 $\mu\text{l hr}^{-1}$ ($Re = 0.0191$, $Wi = 22.2$). (e) Probability distribution function of PS particles at a 5 cm position away from the entrance, showing random positions. (f) Schematic illustration of the force balance in the cross-section of channel when rigid particle migrates under viscoelastic flow.

Figure 2.18 (a) Experimental results of *Chlorella vulgaris* in the EPSs with a flow rate of 400 $\mu\text{l hr}^{-1}$ ($Re = 0.122$, $Wi = 88.9$). (b) Probability distribution function of *Chlorella vulgaris*, showing enhanced focusing behavior

along the centerline of the channel.

Figure 2.19 Autonomous cell-sorting using the self-secreted macromolecules. (a) Microscopic images of the cells in the EPS solution with a flow rate of $400 \mu\text{l hr}^{-1}$ ($Re = 0.122$, $Wi = 88.9$). The superimposed images illustrate the distribution and position of the cells with different sizes in the channel. (b) Probability distribution function of the cells at the outlet of the channel. (c) Separation efficiency of the cells. The graph demonstrates the ratio of the cells moving to a specific area (area 1: 540 to 300 μm , area 2: 300 to 100 μm , area 3: 100 to -100 μm , area 4: -100 to -300 μm , and area 5: -300 to -540 μm).

Figure 3.1 Schematic diagram of the optorheology introduced in this study.

Figure 3.2 Schematic diagram of the electrochemical device. The light is irradiated to the side of the anodic chamber with an intensity of 48.75 W/m^2 .

Figure 3.3 Irradiance spectrum of the halogen lamp employed in this experiments.

Figure 3.4 Geometry specification for numerical simulations. (a) Cell structure developed for modeling. Different configuration of *Synechocystis* self-assembly in the external AC-electric field. (b) System geometry for modeling.

Figure 3.5 Characterization of the cell. (a) Absorption spectrum of *Synechocystis* sp. PCC 6803. It denotes that both chlorophyll (Chl) a and b pigments accumulate in a *Synechocystis* sp. PCC 6803 strain. (b) Scanning electron microscopy (SEM) of *Synechocystis* sp. PCC 6803 showing extracellular appendages. It is peanut-shaped particle composed of two-partially fused spherical lobes in shape. The scale bar represents the length of 200 nm.

Figure 3.6 Electrophoretic properties characterization of the cell. (a) Zeta potential, (b) Conductivity, and (c) Mobility under dark, light condition. Results demonstrate that surface properties of cell is changed during photosynthesis.

Figure 3.7 Electrophoretic properties of photosynthetic bacterium suspension change under the light irradiation. (a) Surface potential of the cells calculated from the soft particle theory. Impedance spectra of the bacterium suspension according to the light condition. (b) Bode plot and (c) Nyquist plot of the photosynthetic bacterium suspension. The inset represents the equivalent circuit model.

Figure 3.8 Photoresponse of the electrochemical device loaded with *Synechocystis* sp.. The measurement was made for 400 s light/dark interval.

Figure 3.9 Rheological properties of the cell suspensions under different light conditions. (a) Viscosity and (b) shear stress as a function of shear rate.

Figure 3.10 Rheological properties of the cell solution under the AC-electric field. (a) Viscosity and (b) shear stress in the range of shear rate from 1 to 1000 s⁻¹.

Figure 3.11 Rheological characterization of the cell suspensions. (a) Viscosity and shear stress under the electric field. (b) Schematic diagram of the spatial arrangement change of the cell suspension under the electric field.

Figure 3.12 Self-assembly of cells under the AC-electric field. (a) Schematic diagram of the experimental setup. (b) Microscopic images of the cells.

Figure 3.13 Self-alignment of *Synechocystis* under the electric field. (a) Optical microscopy images of the distinct configuration change of the cell for 80 s. (b) Total electric energy of cell is changed during self-assembly in the AC-electric field.

Figure 3.14 Total electric energy with respect to the cell orientation under AC-electric field. The decrease total electric energy is in accordance with the experimental results of cell assembly.

Figure 4.1 Scanning electron microscopy (SEM) of *Synechocystis* sp. PCC 6803 showing extracellular appendages. It is peanut-shaped particle composed of two-partially fused spherical lobes in shape. The scale bar denotes a length of 1 μm.

Figure 4.2 Absorption spectrum of *Synechocystis* sp. PCC 6803 and irradiance spectrum of the halogen lamp used in this study. The light source provided a full spectrum of visible light for natural photosynthesis of *Synechocystis* sp. PCC 6803.

Figure 4.3 Dissolved oxygen (DO) variation of *Synechocystis* sp. PCC 6803 with 0.05 M NaHCO₃ during light condition. A polynomial fit with a cubic equation fits to all the data.

Figure 4.4 Rheological measurements of cell solution under the light. (a) Viscosity in the range of shear rate from 0.1 to 100 s⁻¹. The measured viscosity data were fitted to the Carreau model.

Figure 4.4 Schematic illustration of the CFB introduced in this study. The cyanobacteria embedded energy electrolytes are circulated through the flow system.

Figure 4.5 Characterization of the culture with different concentrations of sodium bicarbonate (NaHCO₃). (a) Dissolved oxygen (DO) and (b) pH of the cell suspension with respect to time.

Figure 4.6 Growth of *Synechocystis* sp. PCC 6803 with different concentrations of NaHCO₃ as a carbon source. The data were measured 7 days after supplying NaHCO₃. (a) Optical density of samples. (b) Real image of samples. (Sample 1: 0 M NaHCO₃, Sample 2: 0.005 M NaHCO₃, Sample 3: 0.01 M NaHCO₃, Sample 4: 0.05 M NaHCO₃, Sample 5: 0.1 M NaHCO₃, Sample 6: 0.2 M NaHCO₃, Sample 7: 0.25 M NaHCO₃, and Sample 8: 0.5 M NaHCO₃)

Figure 4.7 Photoelectrochemical behavior of the BPV in the batch mode. (a) Cyclic photo-response measured with respect to time. The light irradiation was imposed after 100 s, and the measurement was made for every 300s light/dark interval. (b) Power density and polarization results of the cell under light.

Figure 4.8 Photoelectrochemical behavior of the CFB. (a) Cyclic photo-response

of the cell measured using a 510 Ω resistance. The light was irradiated after 100 s, and the measurement was made for every 300s light/dark interval. (b) Dark current result and (c) photoresponse current of the cell with respect to the flow rate.

Figure 4.9 Photo-electrochemical performance of the CFB. (a) Power density and (b) polarization results with respect to the flow rate.

Figure 4.10 Effect of the flow rate on the CFB. The max peak power changes according to the flow rate, and the frictional loss was calculated analytically.

Figure 4.11 Results of numerical analysis for the CFB. (a) Velocity profiles in the cathodic chamber according to the flow rate. (b) Distribution of oxygen concentration on the cathode depending on the flow rate.

Figure 4.12 Simulation of oxygen concentration profiles of the electrode surface at 0 ml /min (a), 0.03 ml /min (b), 0.05 ml /min (c), 0.1 ml /min (d), and 0 ml /min (e). The results are the concentration profiles of 0 s, 100 s, 200 s, 300 s, and 400 s after light on.

Figure 5.1 Characterization of the IONPs used in the experiment. (a) SEM images of *Synechococcus* sp., γ -Fe₂O₃, Fe₃O₄. (b) X-ray powder diffraction (XRD) curves of the IONPs. The insets represent the atomic arrangement of magnetite (upper) and maghemite (lower). (c) UV-vis Kubelka-Munk absorbance. The inset is the relation between the band gap energy and $[F(R)h\nu]^{1/2}$ of iron oxide nanoparticles with estimated band gap energy values.

Figure 5.2 Pictures of the bio-photovoltaic device used in the experiment. Detailed dimensions are shown in the schematic illustration of the device and has a unit of mm.

Figure 5.3 Absorption spectrum of *Synechococcus* sp. and irradiance spectrums of the halogen lamp used in this study. The light source provided a full spectrum of visible light for natural photosynthesis of *Synechococcus* sp.

Figure 5.4 Zeta potential of samples. The zeta potentials of *Synechococcus* sp., maghemite, and magnetite were analyzed as a function of pH.

Figure 5.5 Bio-photovoltaic cell proposed in this study. (a) Schematic illustration of the bio-photovoltaic device. (b) Photocurrent generation from the biological-inorganic hybrid system. (c) SEM images of the *Synechococcus* sp. – IONPs complexes and energy-dispersive X-ray spectroscopy (EDS) of the complex. (d) Schematic energy band diagrams for possible electron transfer.

Figure 5.6 The effect of NdFeB on the performance of the electrochemical. (a) Photoresponse of NdFeB. Inset: The observation of NdFeB after the experiments. The intensity of the light source was set to 48.75 W/m^2 . (b) X-ray photoelectron spectroscopy (XPS) spectra of Ni $2p_{3/2}$ for the NdFeB surface. (c) Cyclic photoresponse of cells with magnet and without magnet with the light intensity of 48.75 W/m^2 . (d) Amperometric measurement from cell – IONPs ($\gamma\text{-Fe}_2\text{O}_3$) – NdFeB (Ni-Ni_xO_y) complexes with 500Ω external load at room temperature. The device was first illuminated for 500 s and then in a light/dark cyclic manner per 1500/1000 s until 18000 s. After 18000 s, the light was not irradiated.

Figure 5.7 Bio-photoelectrochemical behavior of the bio-photovoltaic device with the light intensity of 48.75 W/m^2 . (a) Cyclic photoresponse of the complexes. Inset: the schematic image represents the architecture of the complexes (b) Dark current (N=5), (c) Light induced current (N=5). (d) Photoresponse of each component. (e) Enhanced photocurrent of the IONPs-NdFeB(Ni-Ni_xO_y) complex. The white and black bars indicate the light and the dark periods, respectively.

Figure 5.8 Bio-photoelectrochemical behavior of the bio-photovoltaic device. (a) Cyclic photoresponse of the cell – IONPs ($\gamma\text{-Fe}_2\text{O}_3$) – NdFeB (Ni-Ni_xO_y) complexes under different light conditions. (b) Cyclic photoresponse of

the cell – IONPs ($\gamma\text{-Fe}_2\text{O}_3$) – NdFeB ($\text{Ni-Ni}_x\text{O}_y$) complexes with different concentration. The intensity of the light source was set to 48.75 W/m^2 . Inset: Absorption spectra of the cell solution.

Figure 5.9 Bio-photoelectrochemical activities of the samples used. (a) Photocurrent density results. (b) Snapshot of the bio-photovoltaic device. The conventional green LED bulb was turned on using the harvested energy.

Figure 5.10 Photoelectrochemical performance of the bio-photovoltaic device with the light intensity of 48.75 W/m^2 . a) Power density results. b) Polarization curves of the device. c) Average peak power densities of the complexes ($N=3$). d) Ratio between the light and dark peak power densities.

Figure 5.11 Nyquist plot of the cell – IONPs ($\gamma\text{-Fe}_2\text{O}_3$ and Fe_3O_4) – NdFeB ($\text{Ni-Ni}_x\text{O}_y$) complexes. The intensity of the light source was set to 48.75 W/m^2 at the light condition. The inset shows the equivalent circuit model, and the table lists the charge transfer resistance obtained from the modelling.

Figure 5.12 Experimental results with a 1,000-fold concentrated cell solution a) Photoresponse current measured with different cell solutions with the light intensity of 48.75 W/m^2 . The white and black bars indicate the light and dark periods. b) Absorption spectra of the cell solution and concentrated cell solution.

Figure 6.1 Schematic illustration of the broadband multiplex living solar cell proposed in this study. Photocurrents are generated from multiple mechanism simultaneously: (1) the photosynthesis of the cell, (2) hot-electron generation from Au NP (PICS), and (3) interband transition in ZnO NR.

Figure 6.2 Characterization of the cell. (a) Scanning electron microscopy (SEM) of *Synechocystis* sp. PCC 6803 showing two-partially fused spherical lobes

in shape, about 1 to 3 μm in diameter. The scale bar denotes a length of 2 μm . (b) Absorption spectrum of *Synechocystis* sp. PCC 6803. It denotes that both chlorophyll (Chl) a and b accumulate in the light in a *Synechocystis* sp. PCC 6803 strain.

Figure 6.3 Schematic illustration of far-field scattering measurement. The schematic images show (a) side view and (b) top view of the optical set-up, respectively. The scattered light was detected by the spectrometer with respect to the rotating angles.

Figure 6.4 Schematic image of the device. The device is consist of three parts: a photoanode, an anodic chamber, and a MEA. The light is irradiated to the side of the anodic chamber with an intensity of 48.75 W/m^2 .

Figure 6.5 Irradiance spectrums of the halogen lamp used in this study. The light source provided a full spectrum of visible light for natural photosynthesis of *Synechocystis* sp. PCC 6803

Figure 6.6 Characterization of the photoanode. SEM images of the fabricated (a) ZnO NR, and (b) Au NP / ZnO NR. (c) Absorption spectrum of the photoelectrodes: ZnO NR and Au NP / ZnO NR. (d) X-ray powder diffraction (XRD) curves of the ZnO NR grown on an ITO substrate (*) Au NP / ZnO NR grown on an ITO substrate (*).

Figure 6.7 Electrochemical property of fabricated photoanode. (a) Cyclic voltammograms of the photoanode in the presence of the solution containing 50 mM potassium ferricyanide and a supporting electrolyte of 0.1 M KCl. (b) Cyclic photo-response of the photoanode measured with a 510Ω resistance in DI water. The light irradiation started when 100 s elapsed, and the measurement was made for 300s light/dark interval.

Figure 6.8 Bio-photoelectrochemical behavior of the bio-photovoltaic device loaded with *Synechocystis* sp.. Cyclic photo-response of the cyanobacteria flow cell measured with a 510Ω resistance. The light

irradiation started when 100 s elapsed, and the measurement was made for every 300s light/dark interval.

Figure 6.9 Photo-electrochemical performance of the broadband multiplex living solar cell. (a) Power density results. (b) Peak power densities of the systems. (c) Polarization curves of the device. (d) Schematic energy band diagrams of the photoanode complex for electron transfer. The arrows in the figure indicate possible flow of electrons.

Figure 6.10 Polar plots with respect to structure and wavelength. Scattered light intensity by three different photoanode structures at the wavelength of (a) 410 nm, (b) 500 nm, (c) 600 nm and (d) 700 nm, respectively.

Figure 6.11 Far-field scattering effect depending on the wavelength. (a) Normalized intensity of the halogen lamp (black), and the scattered light by ZnO NR (red) and Au NP / ZnO NR (blue) with respect to the wavelength. Notice that both ZnO NR and Au NP / ZnO NR show far-field scattering effect in the full range of the light source. (b) Comparison of the scattered light intensity by Au NP / ZnO NR and ZnO NR with respect to the wavelength. The light intensity was obtained by dividing each scattered light intensity by the halogen lamp intensity at each wavelength.

Figure 6.12 Bio-photoelectrochemical behavior of the electrochemical cell. Cyclic photo-response of the cyanobacteria flow cell measured with a 510 Ω resistance. The light irradiation started when 300 s elapsed, and the measurement was made under a 300 s light – 300 s dark cycle.

Figure 6.13 Viability test. (a) Concentration of viable cell. There is not a statistically notable difference between two groups. (b) A fluorescent optical image of the *Synechocystis* on the Au NP / ZnO NR electrode after an operation. Scale bar denotes 10 μm .

Figure 6.14 SEM image of the electrodes utilized in this experiments. SEM image of the Au NP / ZnO NR on the ITO substrate: (a) top view (b) side view.

SEM image of the cell / Au NP / ZnO NR nanowires on the ITO substrate: (c) top view (d) side view. The bacteria thrives onto the electrode.

Figure 6.15 Broadband multiplex living solar cell. The schematic diagram describing the working mechanisms of the hybrid plasmonic photoanode for the electron generation with respect to the wavelength.

List of Tables

Table 3.1 The equivalent circuit model, and the values of the electrochemical components.

Table 4.1 Parameter list for the Carreau model obtained from chapter 3.

Chapter 1

Introduction

1.1. Biorheological system

Biological fluids (e.g., blood, saliva, DNA, and microalgae) are generally homogeneous at macroscopic scales however disordered at microscopic scales due to its mesoscopic length scales of structures [1]. Biorheology is a generic term for the study of flow and deformation of materials of biological viscoelastic origin resulting from stimulation, mainly by inducing physical stimulations [2]. The aims of biorheology are to determine and characterize the dynamics of physiological processes at all levels of biological organization, and the inter-relationships between rheological properties of various biological systems.

The recent outstanding improvements of the biorheology related analytical methodologies, apparatus, and theories have been developed by adopting microfluidic devices which are dealing with flow behavior and precise control of fluid (**Figure 1.1**) [3-11]. The development sub-field of biorheology, which notably explores flow and deformation behavior on microscopic length scales, affords additional clarity to the connection between rheology and microstructure [12]. For example, it has been reported that under the pressure driven microflow, macromolecules are stretched and tumbled, thus changing the length scales of molecules dynamically, showing the focusing of macromolecules and bioparticles [13]. Thus, the system has provided promising tools for enhancing biorheological research since it has the ability to accurately manipulate the environment.

Moreover, the microfluidic devices can be provided not only mechanical stimuli but also acoustic, electric and magnetic stimuli [14-17]. Various types of stimuli cover the microscale ranges would be clarified the rheological perspective of the materials. Thus, the use of the microfluidic devices containing biological fluids have been developed rapidly in a wide range of applications in biochemistry, drug delivery, medical diagnosis [18, 19].

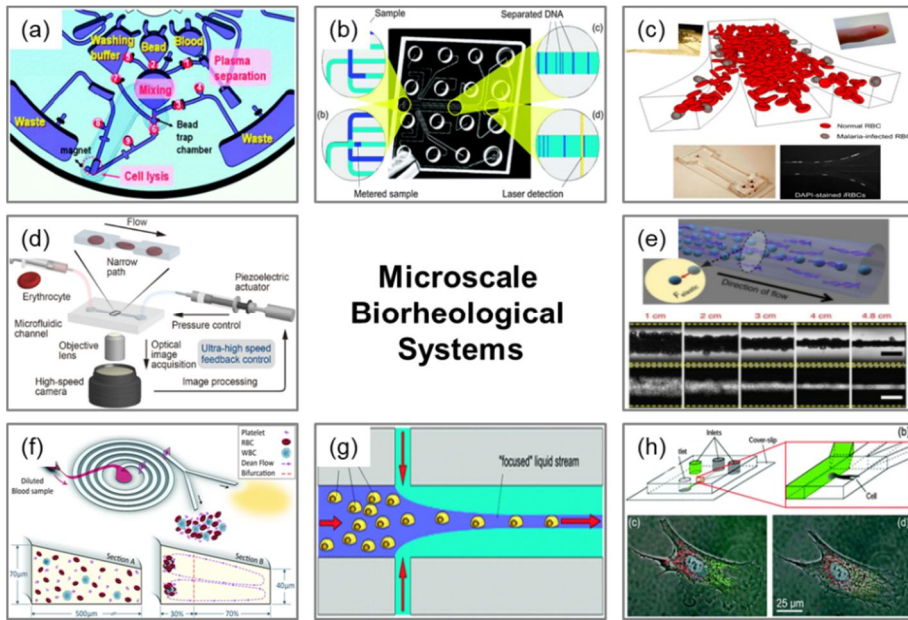


Figure 1.1 Microscale biorheological systems. (a) Centrifugal microfluidic system [3], (b) Electrokinetic platform for DNA [4], (c) Malaria infected erythrocyte separation system [5], (d) Robotic pump system [6], (e) DNA based focuser [7], (f) blood plasma separation system [9], (g) flow focusing structure [10], and (h) microfluidic system for manipulation in a single bovine capillary endothelial cell [11].

1.2. Biophotovoltaics (BPV)

The bioelectrochemical system (BES) includes a broad range of emerging technologies that employ organisms in order to catalyze anodic and/or cathodic reactions such as microbial fuel cell (MFC), photosynthetic microbial fuel cell, complex photosynthetic microbial fuel cell, and biophotovoltaics (BPV) (**Figure 1.2**) [20]. In particular, BPV have an advantage over other photovoltaic systems since BPV employ photosynthetic organisms to convert solar energy into electrical energy. BPV are “living solar cells” that can produce current from the photosynthetic activity of photoautotrophs unlike MFC harnessing heterotrophs which need the organic matter continuously [21]. In addition, BPV are able to generate electricity in both light dependent reaction (i.e., photophosphorylation) and light independent reaction (i.e., Calvin cycle). while common photovoltaics (PV) can generate only during the light period. In these respects, BPs are called a viable system for environmentally-friendly energy generation.

In photosynthetic organism, light is converted into high-energy charge-separated electron–hole pairs, and the excited electrons are transferred through the cytoplasmic membrane connected to the thylakoid membrane, and eventually transported to the exterior via the cell membrane [22-25]. In BPV, the electrons generated from the photosynthetic organism can be transferred to the anode through an external electrical circuit to the cathode, thus producing electricity. Simultaneously, hydrogen secreted from cells are passed through the proton exchange membrane (PEM) to the cathode chamber, where the two electrons are combined with the protons and oxygen to convert water at the cathode.

Current researches of BPV so far have focused on setting the cell physically close to the electrode by gravity in order to increase the efficiency of solar energy conversion. Bombelli *et al.* [26] allow cells to settle onto the electrode for 12h in order to facilitate biofilm for reducing electrochemical potential losses. Moreover,

Bombelli *et al.* [27] developed a microfluidic device BPV that operate without requiring a membrane or mediator. They permit cells to settle on the anode after injection for 24h, yielding high power density above 100 mW/m². These approaches have the disadvantage of being time consuming. Therefore, a different strategy is needed to improve the performance of BPV.

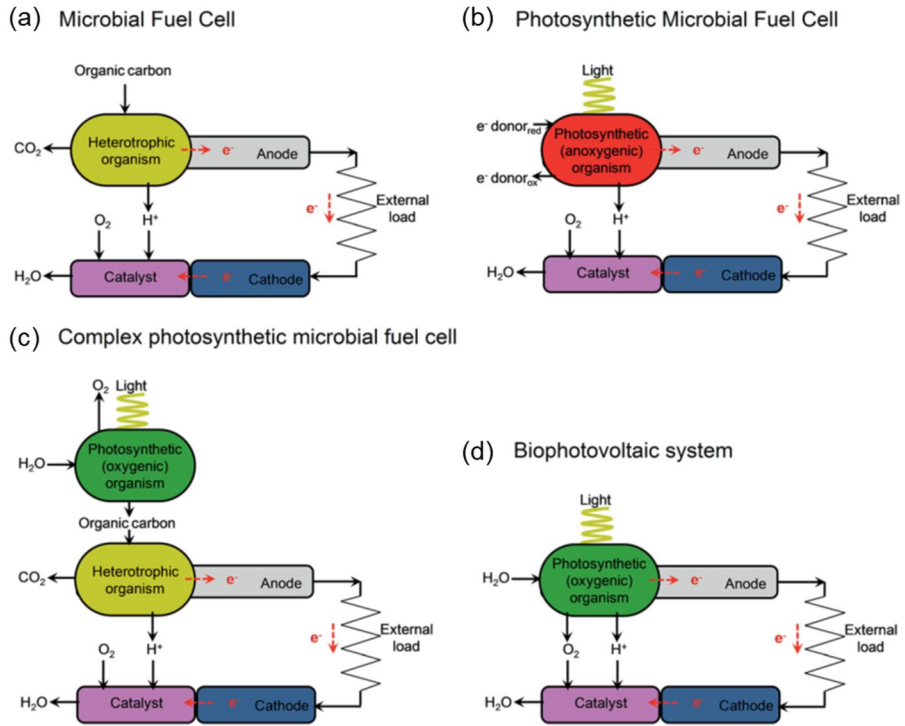


Figure. 1.2 Schematic image of bioelectrochemical systems (BESs) [20]. (a) Microbial fuel cell (MFC), (b) Photosynthetic microbial fuel cell, (c) Complex photosynthetic microbial fuel cell, and (d) Biophotovoltaic system.

1.3. Objectives of present work

The biorheological microfluidics and energy harvesting system will be the major topics of this work. Several novel biophotovoltaic systems will be proposed and analyzed based on biorheology knowledge. In detail, this thesis is organized in the following chapters:

Chapter 2. Autonomous cell-sorting in a microfluidic device using self-produced macromolecules is demonstrated. Extracellular polymeric substances (EPS) have three-dimensional architectures in bacterial biofilms, showing a long relaxation time due to their structural complexity. The ‘self-focusing’ and size-based separation of cells were determined depending on the intrinsic properties of the self-secreted biomolecules.

Chapter 3. Optorheology of the photosynthetic organism is announced. The type IV pili of the bacteria permits electron transport through the external environments, leading the change in the surface properties of the cells during photosynthesis. This boosts the viscosity by increasing the effective phase volume of the suspension. Thus, significant increment of viscosity under light irradiation is observed.

Chapter 4. Sustainable cyanobacterial flow battery using simultaneous light-dependent and -independent reactions by cellular metabolism is demonstrated. The photosynthetic activities of cyanobacteria (*Synechocystis* sp. PCC 6803) was controlled by using bicarbonate ion. Depending on the concentrations of bicarbonate ions, oxygen and electrons were generated in the cathode and anode reservoirs, respectively. Moreover, the cell suspensions containing electrochemical energy were circulated through the flow system in order to transfer electrons from

the cyanobacteria to the anode without using mediators.

Chapter 5. Anomalous power enhancement of biophotovoltaic cell is remarked by using biological inorganic hybrid system. It is reported that *Synechococcus* sp. – iron oxide nanoparticles (γ -Fe₂O₃ and Fe₃O₄) – neodymium iron boride magnet complexes enable great energy harvesting performance by both synergistic combination effect of the natural and artificial photocatalysts and formation of an effective electron transfer conduit to the electrode. Since the surface charges of *Synechococcus* sp. and IONPs are all negative in the range of pH 6 to 9, they repulse each other electrostatically. Therefore, cationic polymer binder is selected to bind them together and form the cell-IONPs complex without any pH adjustment.

Chapter 6. A broadband multiplex living solar cell is demonstrated. *Synechocystis* sp. PCC 6803 onto Au NP / ZnO NR / ITO electrode enable drastic power enhancement by harnessing the favorable spectral region of visible wavelength for photosynthesis of cells. A synthetic photoanode, Au NP / ZnO NR / ITO, is capable of not only generating electron itself, but also amplifying the photosynthetic activity of the cell via the far-field scattering effect in the broadband region of the light, resulting in multiplex living solar cell.

1.4. Bibliography

- [1] S. Haavisto, A.I. Koponen, J. Salmela, *Frontiers in chemistry*, 2 (2014) 27.
- [2] G. Astarita, G. Marrucci, L. Nicolais, *Late Papers*, in: *Rheology*, Springer, 1980, pp. 691-774.
- [3] Y.-K. Cho, J.-G. Lee, J.-M. Park, B.-S. Lee, Y. Lee, C. Ko, *Lab on a Chip*, 7 (2007) 565-573.
- [4] S. Haeberle, R. Zengerle, *Lab on a Chip*, 7 (2007) 1094-1110.
- [5] H.W. Hou, A.A.S. Bhagat, A.G.L. Chong, P. Mao, K.S.W. Tan, J. Han, C.T. Lim, *Lab on a Chip*, 10 (2010) 2605-2613.
- [6] H. Ito, R. Murakami, S. Sakuma, C.-H.D. Tsai, T. Gutschmann, K. Brandenburg, J.M. Pöschl, F. Arai, M. Kaneko, M. Tanaka, *Scientific reports*, 7 (2017) 43134.
- [7] K. Kang, S.S. Lee, K. Hyun, S.J. Lee, J.M. Kim, *Nature communications*, 4 (2013) 2567.
- [8] R. Kita, T. Dobashi, *Nano/Micro Science and Technology in Biorheology*, Springer, 2016.
- [9] M. Rafeie, J. Zhang, M. Asadnia, W. Li, M.E. Warkiani, *Lab on a Chip*, 16 (2016) 2791-2802.
- [10] L. Spielman, S.L. Goren, *Journal of Colloid and Interface Science*, 26 (1968) 175-182.
- [11] S. Takayama, E. Ostuni, P. LeDuc, K. Naruse, D.E. Ingber, G.M. Whitesides, *Nature*, 411 (2001) 1016.
- [12] J.P. Rich, in, *Massachusetts Institute of Technology*, 2012.
- [13] J.Y. Kim, S.W. Ahn, S.S. Lee, J.M. Kim, *Lab on a Chip*, 12 (2012) 2807-2814.
- [14] X. Ding, P. Li, S.-C.S. Lin, Z.S. Stratton, N. Nama, F. Guo, D. Slotcavage, X. Mao, J. Shi, F. Costanzo, *Lab on a Chip*, 13 (2013) 3626-3649.
- [15] M.J. Kim, D.J. Lee, J.R. Youn, Y.S. Song, *RSC Advances*, 6 (2016) 32090-32097.
- [16] M.J. Kim, J.R. Youn, Y.S. Song, *Lab on a Chip*, 18 (2018) 1017-1025.
- [17] S.H. Tan, B. Semin, J.-C. Baret, *Lab on a Chip*, 14 (2014) 1099-1106.
- [18] X. Cheng, D. Irimia, M. Dixon, K. Sekine, U. Demirci, L. Zamir, R.G. Tompkins, W. Rodriguez, M. Toner, *Lab on a Chip*, 7 (2007) 170-178.
- [19] T. Bayraktar, S.B. Pidugu, *International Journal of Heat and Mass Transfer*, 49 (2006) 815-824.
- [20] A.J. McCormick, P. Bombelli, R.W. Bradley, R. Thorne, T. Wenzel, C.J. Howe, *Energy & Environmental Science*, 8 (2015) 1092-1109.
- [21] R.A. Soni, K. Sudhakar, R. Rana, *International Journal of Environment and Sustainable Development*, 15 (2016) 313-325.
- [22] K.L. Saar, P. Bombelli, D.J. Lea-Smith, T. Call, E.-M. Aro, T. Müller, C.J. Howe, T.P. Knowles, *Nature Energy*, 3 (2018) 75.
- [23] K. Tanaka, R. Tamamushi, T. Ogawa, *Journal of Chemical Technology and Biotechnology. Biotechnology*, 35 (1985) 191-197.
- [24] M. Hambourger, G.F. Moore, D.M. Kramer, D. Gust, A.L. Moore, T.A. Moore,

Chemical Society Reviews, 38 (2009) 25-35.

[25] Y. Zou, J. Pisciotta, R.B. Billmyre, I.V. Baskakov, *Biotechnology and Bioengineering*, 104 (2009) 939-946.

[26] P. Bombelli, M. Zarrouati, R.J. Thorne, K. Schneider, S.J. Rowden, A. Ali, K. Yunus, P.J. Cameron, A.C. Fisher, D.I. Wilson, *Physical Chemistry Chemical Physics*, 14 (2012) 12221-12229.

[27] P. Bombelli, T. Müller, T.W. Herling, C.J. Howe, T.P. Knowles, *Advanced energy materials*, 5 (2015) 1401299.

Part I

Biorheological Microfluidics

Chapter 2

Autonomous cell-sorting in a microfluidic device using self-secreted macromolecules

2.1. Introduction

Extracellular polymeric substances (EPS) are biosynthetic macromolecules secreted by microalgae that participate in the formation of three-dimensional microbial biofilm. In this sense, EPS are responsible for structural and functional features of biofilms. They create a protective layer for cells against hostile external environment, that is, protection against toxins and adherence to surfaces for supporting cells with nutrient materials [1-3]. Therefore, the entanglement of the polymers determines the stability of the EPS matrix [4]. EPS also act as extracellular energy and carbon sinks. The formation and maintenance of microbial matrix depend on the characteristics of EPS [4]. Therefore, the multifunctional properties of EPS are affected by the collective features of the biosynthetic macromolecules mixture.

The major components of EPS: polysaccharide, protein and DNA are dispersed in extracellular region with weak physicochemical interactions. In principle, three types of weak interactions can be involved: (1) van der Waals interaction, (2) electrostatic interaction, and (3) hydrogen bond [5]. In many cases, polysaccharide molecules are charged, and can interact with themselves, DNA or proteins including glycoprotein molecules [6]. As a result, the EPS matrix can be regarded as a viscoelastic physical gel (non-permanent), where chemical cross-linking is excluded [7]. Unlike chemical cross-linked polymers, physical gel linked by physical interactions can be deformed by small perturbative forces. In this sense, the intrinsic three-dimensional structure of EPS can be dynamically deformed under the external force depending on their sizes and shapes [8, 9]. Specifically, the hydrodynamic force in the extensional and shear flows was found to lead to a change in the conformation

of semi and/or flexible molecules. It has been reported that under the pressure driven flow, macromolecules are stretched and tumbled, thus changing the length scales of molecules dynamically[10].

Photosynthetic microorganisms, eukaryotic (algae) or prokaryotic (cyanobacteria) are also capable of producing EPS, which is generally accumulated on the microbial cell surface. These microorganisms are the most abundant natural resource in earth and can convert solar energy into fuels such as biomass [11] and electrical energy [12, 13] by photosynthesis. As a matter of fact, microalgae secretes a tremendous amount of EPS representing a great deal of organic carbon [14]. While EPS can cause unwanted problems such as biofouling [15], they have various potentials for environmental applications such as self-mediated extracellular electron transfer for light-driven electrical power system, water treatment, wastewater flocculation and settling, color removal from waste water, metal removal from waste effluents, removal of toxic organic compounds, *etc* [12, 16].

In this work, self-produced biosynthetic macromolecules were analyzed using a microfluidic platform. We extracted EPS secreted from *Chlorella vulgaris* and examined their rheological properties. As shown in **Figure 2.1**, the biosynthetic macromolecules attached to the surface of the microbial cell are mainly composed of polysaccharides, proteins and DNA. We extracted abundant biosynthetic macromolecules from microalgae and investigated the strong elastic effect of EPS on the particle migration in a microfluidic device. We demonstrated autonomous cell-sorting phenomenon adopting the biosynthetic macromolecules secreted by algae. In addition, enhanced particle separation was achieved by using a spiral channel. *Sphaerocystis Schroeteri* with different size distributions was employed for the cell separation. It was found that the intrinsic properties (i.e., viscoelastic feature) of EPS can be utilized for self-sorting and -separation of cells.

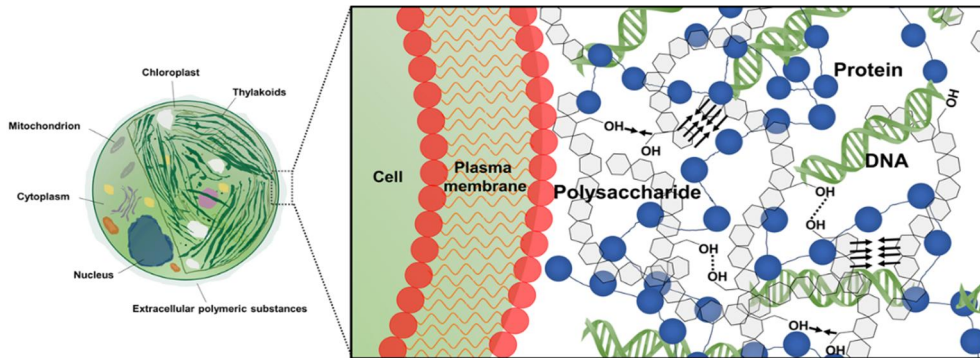


Figure 2.1 Schematic structure of the extracellular polymeric substances (EPS) secreted from *Chlorella vulgaris*. The biosynthetic macromolecules are mainly composed of polysaccharides, proteins and DNA, which are attached to the cell membrane. The components of EPS form three-dimensional networks providing mechanical stability of biofilms.

2.2. Experimental

2.2.1. EPS extraction and solution preparation

Extracellular polymeric substances (EPS) were obtained from *Chlorella vulgaris* (AG10052, KCTC, Korea), which was cultivated in two different environments: one is in the BG11 medium (C3061, Sigma Aldrich) for 3 months before usage and the other is on the surface of agar (1020-4405, Daejung Chemicals) plate in Petri dishes for 2 weeks before usage. In order to extract EPS from bacterial biofilm, chemical and physical methods were applied[17]. For the chemical method, 2% EDTA (15105, Daejung Chemicals) was employed to remove the cations that bridge the negatively charged groups of the polysaccharide and protein moieties of EPS [4, 18]. After mixing with EDTA, the sample was shaken at 50 rpm under red-blue LED light for 1 h, and then stored at 4 °C for 3 h. Thereafter, the sample was centrifuged at 3900 rpm and 25°C for 20 min as the physical method. Finally, the extracted EPS were purified using 0.2 µm membrane (C020A047A, Advantec MFS Inc., USA). The filtrates were used for the experiments in this study.

For the Newtonian solution, 13.8 wt% sucrose (S9378, Sigma Aldrich) was mixed into the DI water. 0.9 wt% PEO (Poly(ethylene oxide)) (372781, Sigma Aldrich) solution was used as a reference viscoelastic solution in order to be compared with the EPS solution. Three types of polystyrene particles with uniform sizes of 3 µm (79166, Sigma Aldrich), 6.27 µm (FP-6056, Spherotech) and 10.2 µm (C37259, Thermo Fisher Scientific) were suspended in the solution with a volume fraction of 0.1 %. For size-based separation, *Sphaerocystis schroeteri* was cultivated in BG11 for 14 days before use. Morphology of *Sphaerocystis schroeteri* was examined with an inverted optical microscope (IX53, Olympus).

2.2.2. Solution characterization

The sample was characterized in various ways [19]. The total amount of extracted EPS was estimated by measuring the weight of solids after lyophilization. The EPS were characterized through the following chemical, structural, and rheological analyses:

1. Chemical analysis: The composition of the EPS was analyzed by using the following colorimetric methods, which employ the phenol-sulfuric acid method [20], the Pierce® BCA protein assay (Thermo scientific, Rockford, IL, USA), and Nano-200 Nucleic Acid Analyzer (MEDCLUB, Tainan, Taiwan). The chemical structure of EPS was investigated through Fourier-transform infrared spectroscopy (FT-IR) analysis (Nicolet iS50, Thermo Fisher, Madison, USA). Solid samples were prepared via the lyophilization of aqueous solution. The degree of the cell destruction in EPS was examined by using a UV-vis spectrometer (V-770, JASCO, Japan).
2. Structural analysis: The morphology of the biofilms was characterized by using field emission scanning electron microscopy (FE-SEM; JSM-7600F, JEOL Ltd., Japan). Before the observation of biofilms, the biofilms were freeze-dried and mounted on a copper stub using an adhesive carbon tape. Atomic force microscopy (AFM, NX-10, Park Systems) was used to observe the topographic image of exopolysaccharides. The molecules are spread on freshly cleaved mica substrate (a hydrophilic aluminosilicate mineral).
3. Rheological analysis: Rheological properties were measured by using a stress-controlled rheometer (Discovery HR-3, TA Instruments, New Castle, USA) with a 60-mm diameter parallel plate. The steady-state shear rates were applied in the range of 0.1 through 1,000 s^{-1} , and the angular frequency range was 1 – 100 rad s^{-1} . All the shear viscosity data were fitted successfully by the Carreau–Yasuda model and allowed the estimation of elasticity of the samples.

The cross-over point between the loss modulus and the storage modulus gives the average relaxation time for EPS assuming the Maxwell model described by $G'(\omega) = \eta\lambda\omega^2/(1 + \lambda^2\omega^2)$ and $G''(\omega) = \eta\omega/(1 + \lambda^2\omega^2)$, where η is the viscosity, ω is the angular frequency, and λ is the total average relaxation time. According to the classical Zimm's polymer theory, the relaxation time of semi-flexible polymer in good solvent depends on the coil size [21]: $\lambda_z = F \frac{[\eta]M_w\eta_s}{N_A K_B T} \approx \frac{\eta_s R_g^3}{K_B T}$, where $[\eta]$ is the intrinsic viscosity of the solution, M_w is the polymer molecular weight, η_s is the viscosity of the solvent, N_A is Avogadro's number, K_B is the Boltzmann's constant, T is the absolute temperature, and R_g is the radius of gyration for semi-flexible polymer. $R_g \sim L^{\frac{3}{5}}(l_p d)^{\frac{1}{5}}$ is determined by the contour length (L), the persistence length (l_p) reflecting the chain stiffness, and the effective polymer diameter (d) [22]. That is, the total average relaxation time is determined by the linear combination of the chemical components constituting the EPS and the structural information of the EPS.

2.2.3. Microchip fabrication and imaging

The microchannel was fabricated on a 4-inch silicon wafer by using a standard soft lithography technique [23]. The microfluidic chip was composed of a poly(dimethylsiloxane) (PDMS, Sylgard 184, Dow Corning) replica and slide glass. The base and curing agent of PDMS (10:1) were thoroughly mixed and degassed in a vacuum chamber for 30 min. The mixture was poured onto the SU-8 photoresist mold and cured in an oven at 70°C for 12 h. The PDMS replica was bonded onto the slide glass after oxygen plasma treatment. Then, the devices were placed on a hotplate at 120 °C for 20 min to increase bonding strength. A straight square microchannel and a rectangular spiral microchannel were used in the experiments. The dimensions of the straight square microchannel were 50 μm \times 50 μm \times 5 cm. The rectangular spiral channel had ten loops, and its width and height were 100 and 25 μm (the channel aspect ratio, γ , is 0.25), respectively. Total arc-length was approximately 50 cm, and the initial radii of curvatures were 4, 6.6, 8.25 and 9.5 mm. The spiral channel was designed and fabricated to evaluate the elastic force and Dean drag force for particle migration according to the size of particles [24]. Schematic illustration of the microfluidic device is given in **Figure 2.2**.

Particle dynamics was observed using an inverted optical microscope (IX53, Olympus), and the images were acquired with a high-speed fluorescence camera (AcquCAM 23G, JNOPTIC co.,Ltd) using an image software package (JNOPTIC Capture 2.4). The ImageJ (NIH) software was used for image processing in order to determine the particle distribution in the microchannel. The images were stacked in the z direction using either the 'standard deviation' or 'min intensity' options. The size of the cells used in the microchannel experiments was obtained via the image processing. It was assumed that the cell has a spherical shape and the cell diameter was rounded off to the first decimal point.

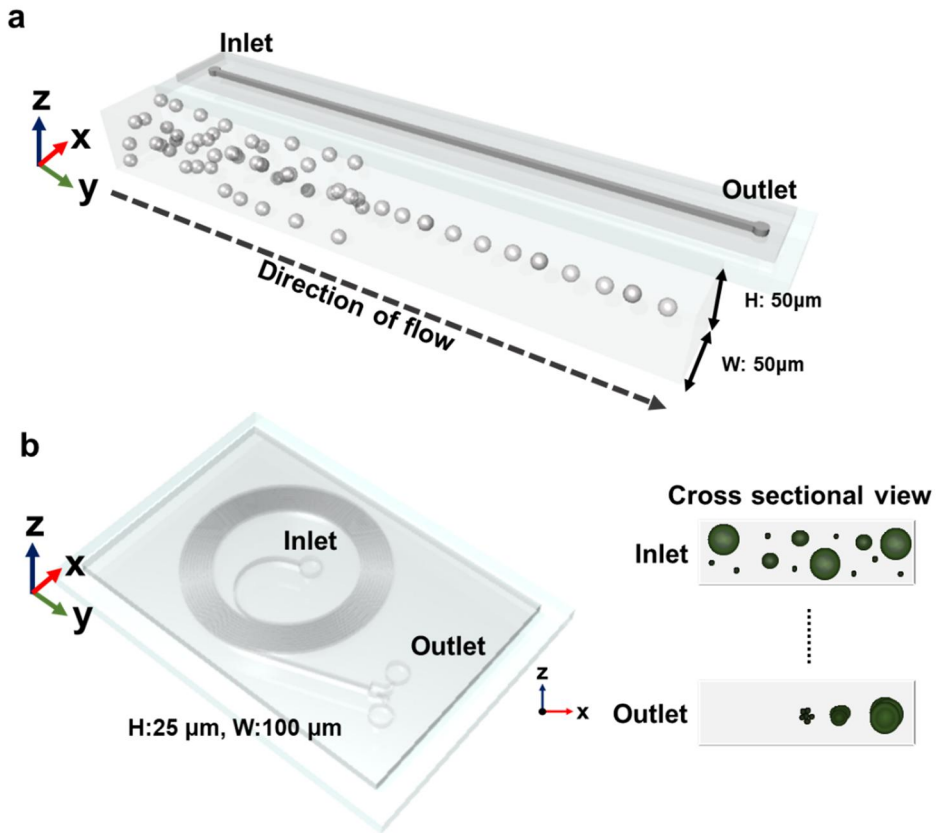


Figure 2.2 Schematic diagram of the microfluidic chips used in this study. (a) Schematic illustration for Elasto-inertial particle focusing under the EPS solution in a square channel. As the distance from the inlet increases, the Elasto-inertial particle focusing within the channel appears as a line. (b) Schematic illustration for Dean-coupled Elasto-inertial particle focusing under the EPS solution in a spiral channel. In a confined microchannel, different sized particles show different equilibrium positions at an outlet due to elastic force and Dean drag force.

2.3. Numerical analysis

Finite element simulation was carried out to analyze the particle focusing behavior by harnessing the Oldroyd-B model in the straight microchannel. For simulation, the steady-state momentum equation is expressed as $Re(u \cdot \nabla)u = \nabla \cdot (-pI + (\eta_s/\eta)[\nabla u + \nabla u^T] + T)$, and the extra stress contribution becomes $T + Wi \frac{\nabla}{T} = (\eta_p/\eta)[\nabla u + \nabla u^T]$. Here, Re and Wi are the Reynolds number and the Weissenberg number, respectively. η_s is the relative solvent viscosity, η_p is the relative polymer viscosity, and the total viscosity, $\eta = \eta_s + \eta_p$. $\frac{\nabla}{T}$ is the upper convected derivative operator expressed as $\frac{\nabla}{T} = \partial T / \partial t + (u \cdot \nabla)T - [(\nabla u) \cdot T + T \cdot (\nabla u)^T]$.

2.4. Results and discussion

2.4.1. Characterization of the EPS

To evaluate morphological microstructure of EPS, the biofilm of *Chlorella vulgaris* was freeze-dried and analyzed. The SEM observation showed that multilayer biofilm with complex structure was developed (**Figure 2.3**). The microorganisms were embedded and interconnected within the self-produced matrix. The immobilized cells were spherical, and their diameters varied from 2 to 4 μm . The SEM image confirmed the role of EPS as a structural support for the microbial aggregates.

In order to figure out physicochemical properties of the self-secreted biomaterials, various characteristics of the EPS were examined. The composition of the EPS obtained from the EDTA extraction method, i.e., based on colorimetric analysis. The concentrations of carbohydrate, protein and DNA were approximately 73400, 469 and 274 $\mu\text{g ml}^{-1}$, respectively. It was found that exopolysaccharides were a major component of the EPS matrix [25, 26]. It is generally known that the EDTA method is an ideal method for EPS extraction with minimal cell destruction. The ratio of protein/polysaccharide was below 1, which confirmed that the EPS extracted in this experiment was not contaminated much by intracellular matrix from cells [27, 28].

In addition, it was revealed that the content of the DNA was relatively low, suggesting that some degree of cell destruction had not occurred during the extraction process. If the cells were destroyed during the extraction, the absorption peak of EPS shows the peak near 650 – 700 nm indicating intracellular substances leaked out. In other words, the UV–visible spectrum could be employed to evaluate the cell-destroying degree caused by CER extraction. UV–visible spectrum of EPSs also demonstrated that the EDTA extraction method did not cause cell lysis (**Figure 2.4**) [29].

Figure 2.5 represents infrared spectrophotometry of the EPSs extracted from

Chlorella vulgaris. The broad band at 3392 cm^{-1} corresponded to -OH carbohydrates and/or -NH of proteins. The weak band at 3015 cm^{-1} was related to the $-\text{CH}_3$ stretching vibration of fatty acids, the band at 1619 cm^{-1} and 1347 cm^{-1} were attributed to the C=O anti-symmetric and symmetric stretching in the carboxylate [30] and/or stretching vibration of the amino acids of proteins [31], and the band at 1215 cm^{-1} was related to the C-N stretching vibration of amino acids of proteins. The bands in the frequency range of $900 - 1200\text{ cm}^{-1}$ resulted from stretching vibration in the sugar derivatives as well as DNA/RNA [32]. These results showed the presence of the carboxyl, hydroxyl and amino group. Therefore, the charged exopolysaccharides can form physical gels by interacting with not only themselves but also proteins and DNAs.

Rheological behavior of the extracted EPSs is shown in **Figure 2.6** and **Figure 2.7**. In the considered shear-rate range, the aqueous solution exhibited a strong shear thinning behavior. From a rheological perspective, such behavior is attributed to the alignment of entangled molecules along the direction of the applied shear flow [8, 9]. The Carreau-Yasuda model was used to describe the relation between viscosity and shear rate (**Figure 2.6**). The predicted zero-shear viscosity was approximately $0.015\text{ Pa}\cdot\text{s}$. Furthermore, dynamic oscillatory shear experiments were conducted to analyze rheological behavior of the EPSs. The storage and loss moduli were measured as a function of the angular frequency (**Figure 2.7**). The cross-over point between the loss modulus and the storage modulus could characterize the average relaxation time of the order of 0.1 s . In comparison with a viscoelastic fluid with similar zero-shear viscosity, it was found that the EPSs had a relaxation time approximately twice as long as that of the viscoelastic fluid (**Figure 2.8** and **Figure 2.9**). The viscoelastic property of the solution can be evaluated by using the Weissenberg number ($Wi \equiv \lambda\dot{\gamma}$), which is defined by the relaxation time of a polymer solution (λ) and the strain rate of flow ($\dot{\gamma}$). Hence, the EPSs are expected to be more elastic than the synthetic polymer solution at the same strain rate. These results are attributed to the structural characteristics of the EPSs.

According to the classical Zimm's polymer theory, the relaxation time of the

polymer in good solvent depends on the coil size [21]: $\lambda_z = F \frac{[\eta]M_w\eta_s}{N_A K_B T} \approx \frac{\eta_s R_g^3}{K_B T}$, where $[\eta]$ is the intrinsic viscosity of the solution, M_w is the polymer molecular weight, η_s is the viscosity of the solvent, N_A is the Avogadro's number, K_B is the Boltzmann's constant, T is the absolute temperature, and R_g is the radius of gyration. The Flory theory gives the R_g for a semi-flexible polymer as follows: $R_g \sim L^{\frac{3}{5}}(l_p d)^{\frac{1}{5}}$, where L is the contour length of the polymer, l_p is the persistence length which is reflecting the chain stiffness, and d is the effective polymer diameter. Thus, both M_w and R_g are strongly related to the relaxation time of polymer. In addition, the effects of chemical composition of the EPSs on the viscoelasticity were evaluated as follows: Polysaccharide, protein and DNA were dissolved in the solution, and their fractions were 0.99, 0.0063 and 0.037, respectively. Depending on the proportion of each material in the solution, the total average relaxation time is determined by the linear combination of relaxation times for each substances.

In order to obtain the nanostructural information of exopolysaccharide with the highest proportion in the solution, the sample was analyzed by using AFM. The topographical structures of exopolysaccharides are shown in **Figure 2.10**. It was observed that the height of the fibril was in the range of 0.6 to 2 nm corresponding to the dimension of a single molecular polysaccharide chain [33]. In the present study, the exopolysaccharide molecules had long molecules (over hundreds of nanometers) with linear or branched conformation, resulting in a shear-thinning behavior [34]. More specifically, the networks encompassed fibrils interconnecting spherical nanoparticles and globules. The globules can represent positively charged proteins [35]. Therefore, it is speculated that the relaxation time of the exopolysaccharide is quite long.

In addition, the previous results revealed that the structural characteristics of DNA resulted in relatively large coil size in equilibrium, thus leading to longer relaxation time than a synthetic polymer [21, 22, 36]. For example, λ -DNA has a long

relaxation time of 140 ms [37]. That is, eDNA can strongly affect the viscoelasticity of the solution although the concentration of the eDNA in the solution is low [37]. Therefore, the three components of the EPS, which were connected by weak physical forces, had long relaxation time due to their structural features and enhanced viscoelastic effect.

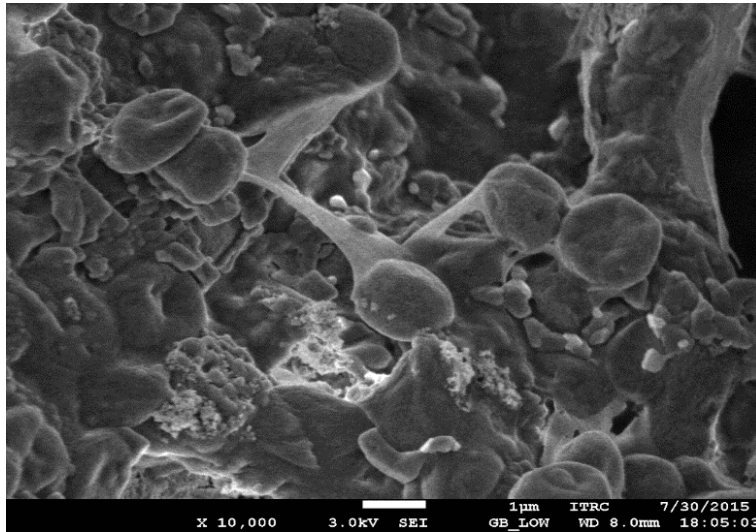


Figure 2.3 Scanning electron micrograph of *Chlorella vulgaris* in biofilm. The scale bar denotes the length of 1 µm.

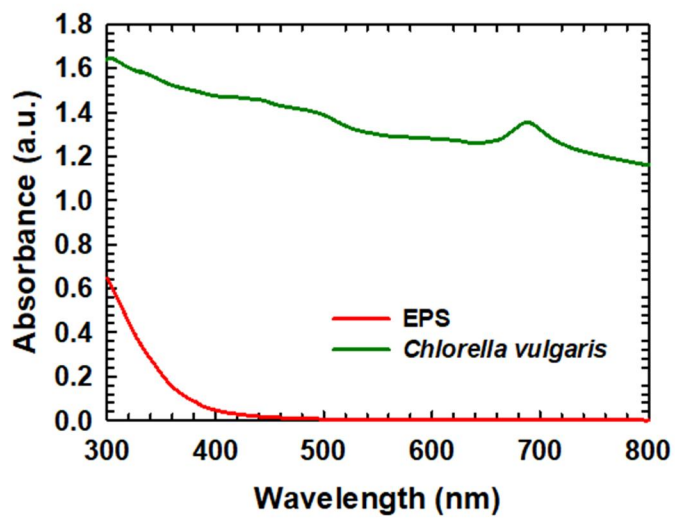


Figure 2.4 UV-Vis spectra of *Chlorella vulgaris* and EPS.

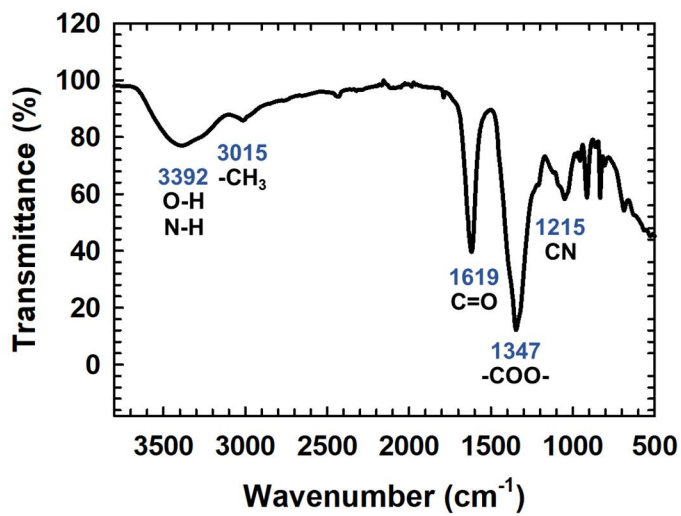


Figure 2.5 FT-IR spectrum of the EPS extracted from *Chlorella vulgaris*.

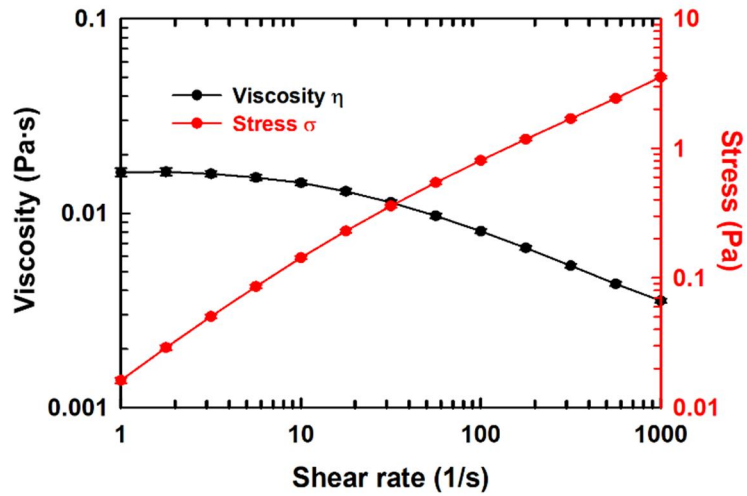


Figure 2.6 Rheological properties of the EPS for shear rates ranging from 1 to 1000 s^{-1} . The Carreau-Yasuda model was used to fit the EPS.

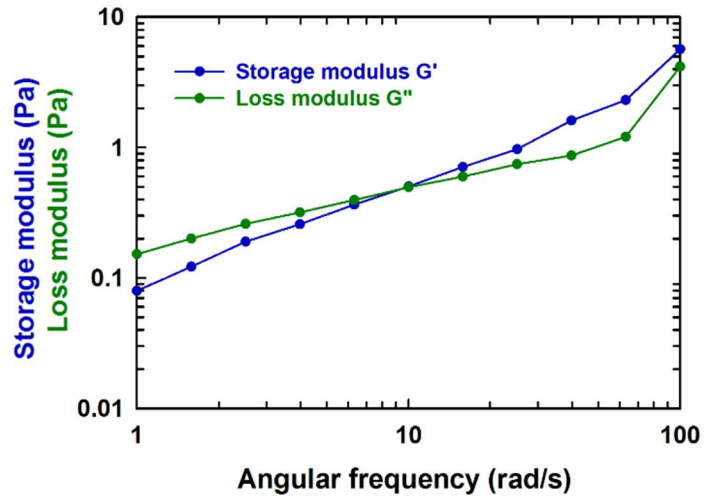


Figure 2.7 Storage modulus (G') and loss modulus (G'') of extracted EPS as a function of angular frequency.

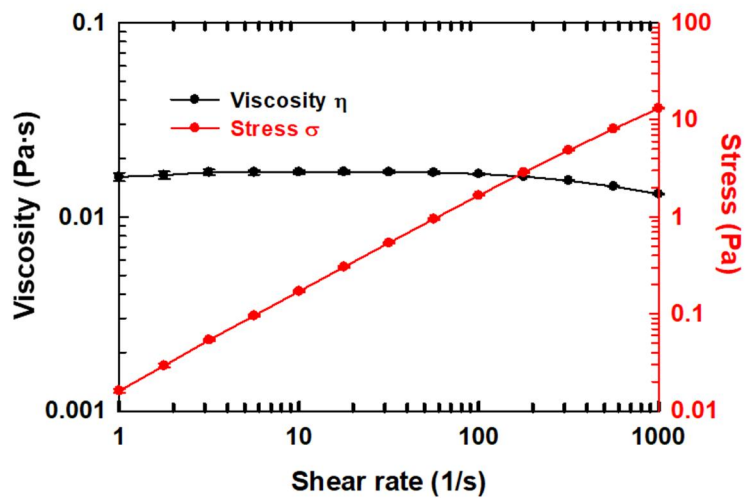


Figure 2.8 Rheological measurements of the 0.9 wt% PEO solution. Viscosity and shear stress in the range of shear rate from 1 to 1000 s^{-1} .

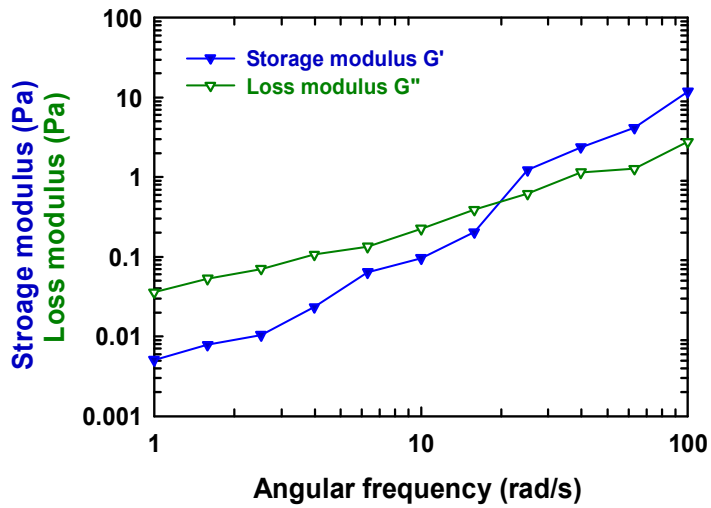


Figure 2.9 Storage modulus (G') and loss modulus (G'') of the 0.9 wt% PEO solution as a function of angular frequency.

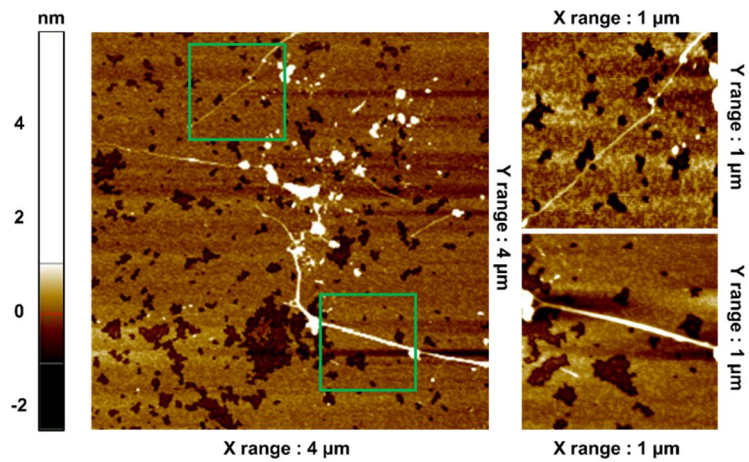


Figure 2.10 AFM images of the exopolysaccharide of the extracted EPS. The height of fibrils was in the range of 0.6 – 2 nm, which indicated the presence of a single molecular polysaccharide chain.

2.4.2. Manipulation of particle in the microchannel

We exploited the properties of extracted EPSs to manipulate particle motion in pressure driven microflow. The migration of particles (diameter = 6.27 μm) within a straight channel (length: 5cm; width \times height: 50 μm \times 50 μm) was examined under a flow rate of 50 $\mu\text{l hr}^{-1}$ ($Re = 0.019$, $Wi = 22.2$). Overlaid fluorescent images were acquired to show the lateral migration of particles at six different axial locations of the microchannel. Once particles were injected into the channel, they were subsequently subject to the elastic force and gradually aligned along the centerline of the straight channel. This phenomenon is called the ‘elasto-inertial particle focusing’ (**Figure 2.11a**). As the distance from the inlet increases, the particle focusing area within the channel appears as a line with intense intensity. **Figure 2.11b** presents the probability density function determined across the channel width. **Figure 2.11** shows the influence of distance from the inlet on particle focusing. Thus, we infer that the self-secreted EPS with polysaccharide, protein and DNA can highly enhance the particle focusing behavior.

In order to investigate the effect of EPS concentration on particle focusing, we conducted the experiments with diluted EPS in three different concentration conditions: 2/3 times dilution; 2 times dilution; 4 times dilution (**Figure 2.12**). At a position of 5cm downstream from the inlet, images were obtained with a flow rate of 50 $\mu\text{l hr}^{-1}$. 3-line particle focusing was observed at all three fluidic conditions. This is due to a decrease in elastic force as the solution is diluted.

Numerical simulation was carried out for the first normal stress difference in order to provide further physical insight into the elasto-inertial particle focusing in the EPS. The main force acting on the particles is elastic force, $\overrightarrow{F_E}$, where the elastic force is scaled as $\overrightarrow{F_E} \approx D_P^3 \nabla N_1$, which is proportional to the particle diameter (D_P) and the first normal stress difference (N_1). Since the normalized value of N_1 showed minimum values at four corners and at the center of the cross-section as shown in **Figure 2.13**, particles moved towards the center and four corners. We also affirmed

that the normalized first normal stress difference (N_1) shows the lowest values at the center of the cross-section ($x/L = 0$), as shown in **Figure 2.13b**.

For the purpose of evaluating the effect of flow rate on the particle focusing, we analyzed the dynamic behavior of particles (diameter = 6.27 μm) at a location of 5 cm away from the inlet at flow rates of 50 – 3000 $\mu\text{l hr}^{-1}$ ($Re = 0.0191 - 1.14$, $Wi = 22.2 - 1330$, $El = 1170$). **Figure 2.14** shows the overlapped fluorescent streak images of particle focusing at different flow rates. At a flow rate lower than 1000 $\mu\text{l hr}^{-1}$ ($Re = 0.381$, $Wi = 4.44$), single streamline was clearly observed in the channel. It was found that the particle focusing was achieved for wide range of flow rates, and the state of the particle focusing was stable when compared with the results of previous studies having a limitation at flow rates lower than 200 $\mu\text{l hr}^{-1}$ [38, 39]. This is attributed to the structural stability and high relaxation time of EPSs, compared with the synthetic polymer solution. When the flow rate became higher than 1000 $\mu\text{l hr}^{-1}$, particles began to defocus and made two streamlines in the channel. It can be explained by the fact that the inertial force becomes significantly higher than the elastic force, resulting in the distortion of particle focusing. For a more quantitative analysis, the normalized fluorescence intensity distribution of the particle focusing along the lateral position is demonstrated in **Figure 2.14b**. The single streamline particle focusing phenomena became clear with increasing velocity and showed a maximum intensity at a flow rate of 100 $\mu\text{l hr}^{-1}$. As the velocity increased, the distribution of particle is skewed toward both sides of the channel.

In order to investigate the effect of long relaxation time, we analyzed the dynamic behavior of particles (diameter = 6.27 μm) in 0.9 wt% PEO solution at a location of 5 cm away from the inlet at flow rates of 50 - 3000 $\mu\text{l hr}^{-1}$ ($Re = 0.0191 - 1.14$, $Wi = 22.2 - 1330$, $El = 1170$). **Figure 2.15** shows the overlapped fluorescent streak images of particle focusing at different flow rates. At 50 $\mu\text{l hr}^{-1}$ ($Re = 0.191$, $Wi = 222$), single streamline was clearly observed in the channel. In contrast to EPSs, particles began to defocus and showed random distribution when the flow rate became higher than 700 $\mu\text{l hr}^{-1}$. This is attributed to the relaxation time of PEO

solution.

Multiplex particle focusing was also examined with particles of 3 μm and 10 μm diameters in a spiral microchannel at a flow rate of 400 $\mu\text{l hr}^{-1}$ (**Figure 2.16**). In a spiral microchannel, the equilibrium position of particles moving within the non-Newtonian medium is determined by the combination of the Dean drag force ($\vec{F}_D \approx \rho U^2 D_h^2 D_p / \gamma$) and the viscoelastic force ($\vec{F}_E \approx D_p^3 \nabla N_1$). Therefore, the equilibrium position of particles is determined by the particle size. According to the previous report [24], the normalized Dean force is related to the channel aspect ratio (γ) and the blockage ratio (D_p/D_h). Lee *et al.* [24] showed that the Dean forces significantly increase with respect to the blockage ratio. We investigated the influence of particle size on the equilibrium position after ten turns. In **Figure 2.16a**, the 3 μm particle had an equilibrium position at the centerline of the channel, indicating that the viscoelastic force dominated the Dean drag force. However, in the case of the 10 μm size particles, the lateral displacement of the equilibrium position was observed due to the Dean drag force (**Figure 2.16c**). The probability distribution function for both particles indicated that the equilibrium positions were affected greatly by the particle size. In other words, as the number of turns increased, the larger particles were positioned closer to the outer channel wall. Therefore, the different sized particles could be separated and bifurcated at the outlet (**Figure 2.16e**).

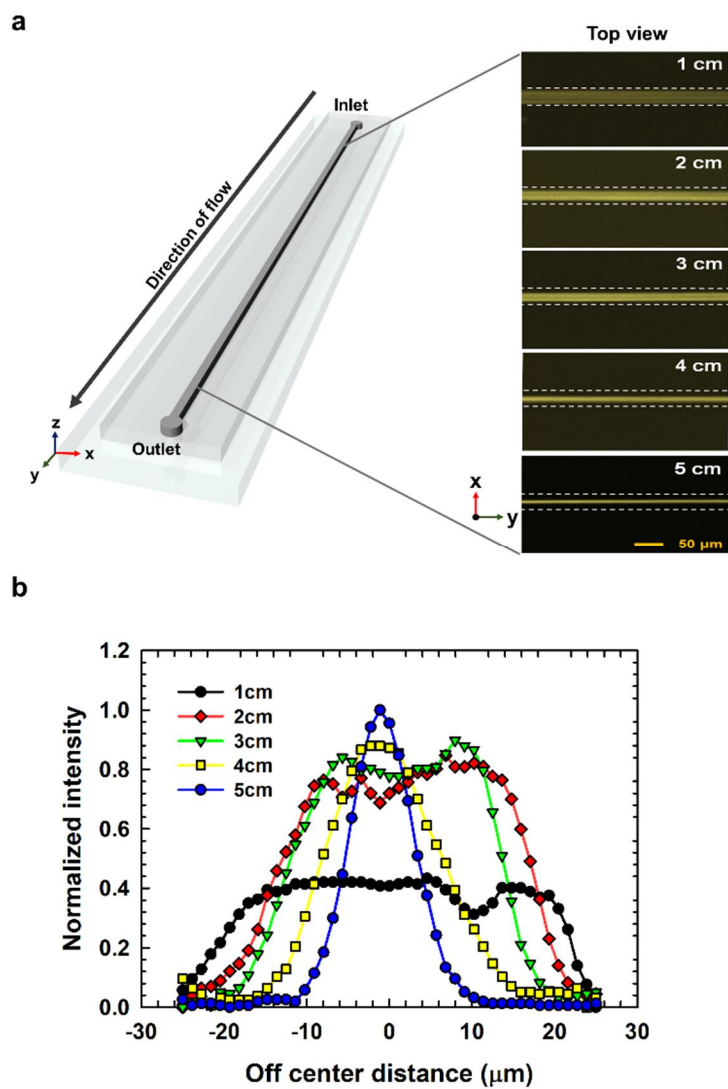


Figure 2.11 Lateral particle migration in the EPS solution. (a) Particle focusing of $6.27 \mu\text{m}$ fluorescent PS particles with a flow rate of $50 \mu\text{l hr}^{-1}$. The hashed lines indicate the channel walls. The scale bar implies $50 \mu\text{m}$. (b) Probability distribution function of the PS particles with a flow rate of $50 \mu\text{l hr}^{-1}$.

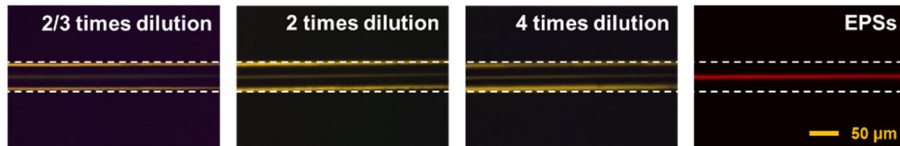


Figure 2.12 Particle behavior of the different concentration of EPSs at a position of 5cm downstream from the inlet for 6.27 μm fluorescent PS particles with a flow rate of 50 $\mu\text{l hr}^{-1}$ ($Re = 0.0191$, $Wi = 22.2$). The scale bar is 50 μm .

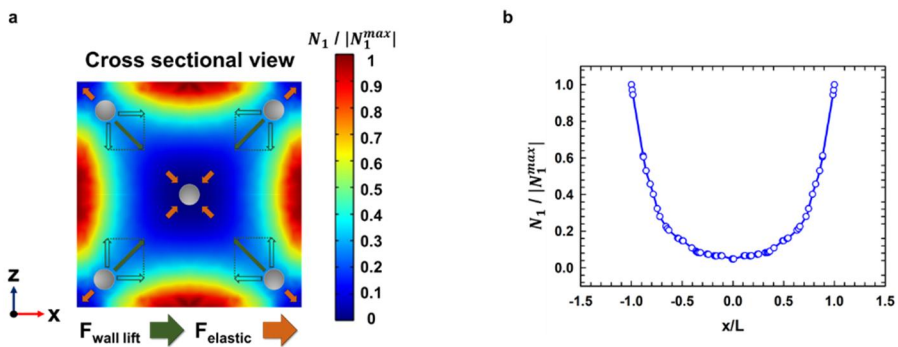


Figure 2.13 Analysis of particle focusing phenomena. (a) Predicted distribution of the first normal stress difference (N_1) and schematic expression of forces exerted on a rigid particle under viscoelastic flows. (b) The value of the normalized first normal stress difference (N_1) shows symmetry at the cross-section of the channel.

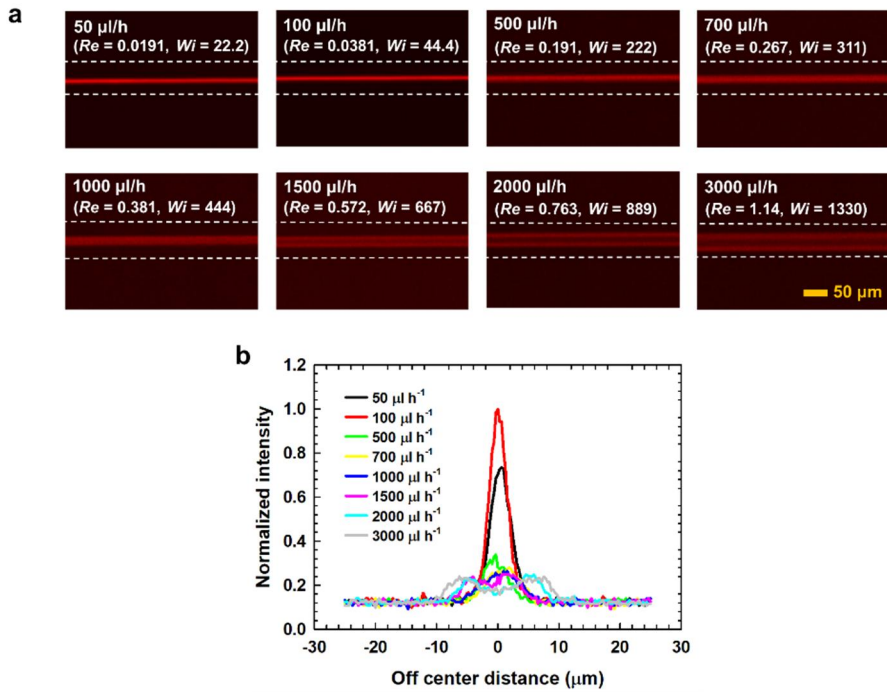


Figure 2.14 (a) Particle focusing behavior of the EPSs in a straight channel at flow rates of 50 - 3000 $\mu\text{l hr}^{-1}$ ($Re = 0.0191 - 1.14$, $Wi = 22.2 - 1330$). The scale bar is 50 μm . (b) Probability distribution function of PS particles under flow rates of 50 – 3000 $\mu\text{l hr}^{-1}$ ($Re = 0.0191 - 1.14$, $Wi = 22.2 - 1330$).

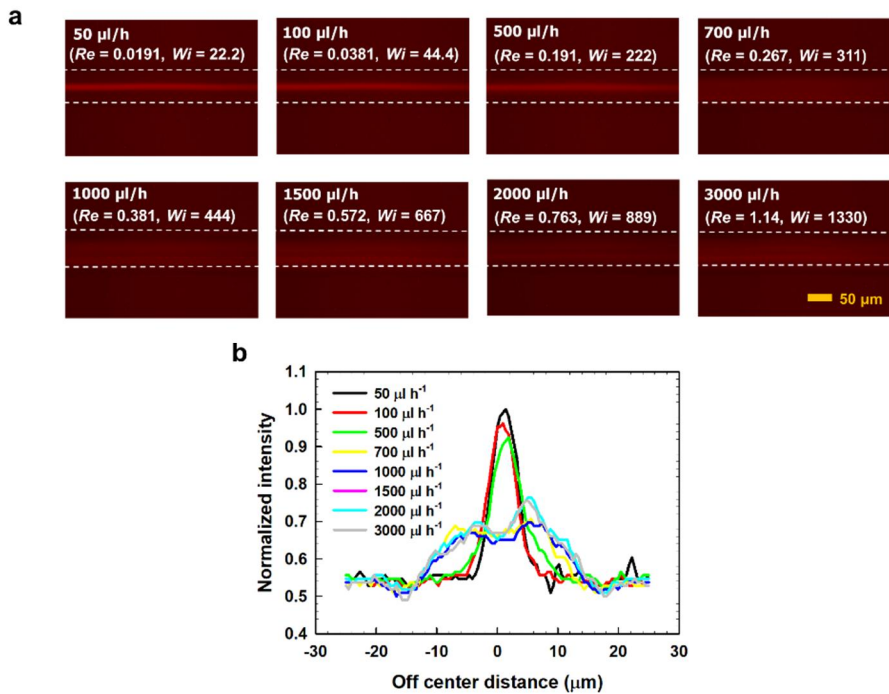


Figure 2.15 (a) Particle focusing behavior of the 0.9 wt% of PEO solution in a straight channel at flow rates of 50 - 3000 $\mu\text{l hr}^{-1}$ ($Re = 0.0191 - 1.14$, $Wi = 22.2 - 1330$). The scale bar is 50 μm . (b) Probability distribution function of PS particles under flow rates of 50 - 3000 $\mu\text{l hr}^{-1}$ ($Re = 0.0191 - 1.14$, $Wi = 22.2 - 1330$).

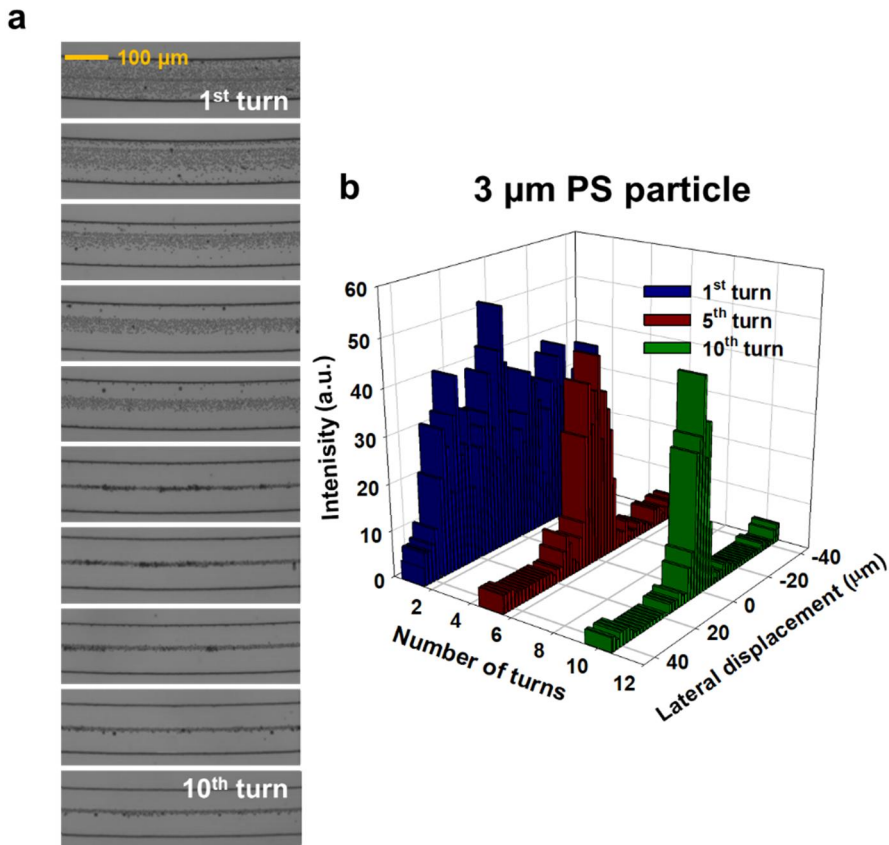


Figure 2.16 Particle separation using the self-secreted biomaterials. Microscopic images for (a) the 3 μm PS particles and (c) the 10 μm PS particles in the EPSs solution with a flow rate of $400 \mu\text{l hr}^{-1}$ ($Re = 0.122$, $Wi = 88.9$). Probability distribution functions for (b) the 3 μm PS particles and (d) the 10 μm PS particles after 1, 5 and 10 turns, showing particle focusing at the center and at the off-center, respectively. (e) Microscopic images illustrating the position and separation of the 3 and 10 μm PS particles at the outlet of the channel. (f) Probability distribution function of the 3 and 10 μm PS particles at the outlet.

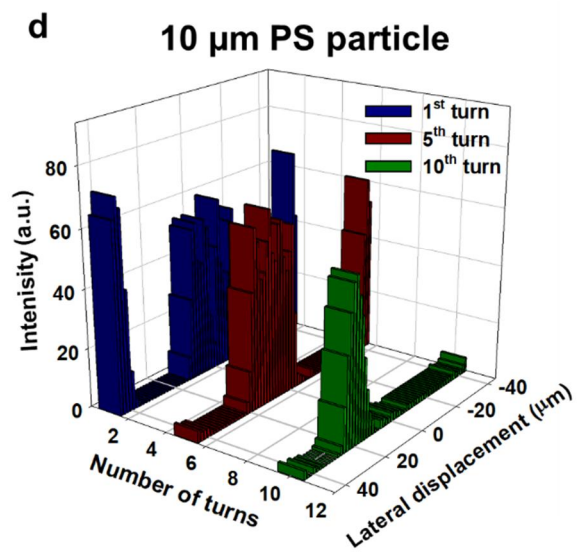
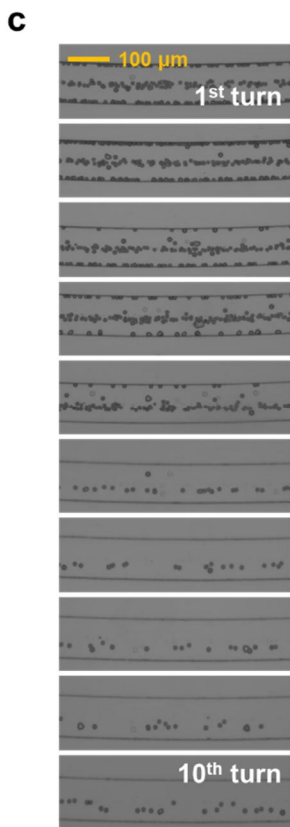


Figure 2.16 (continued.)

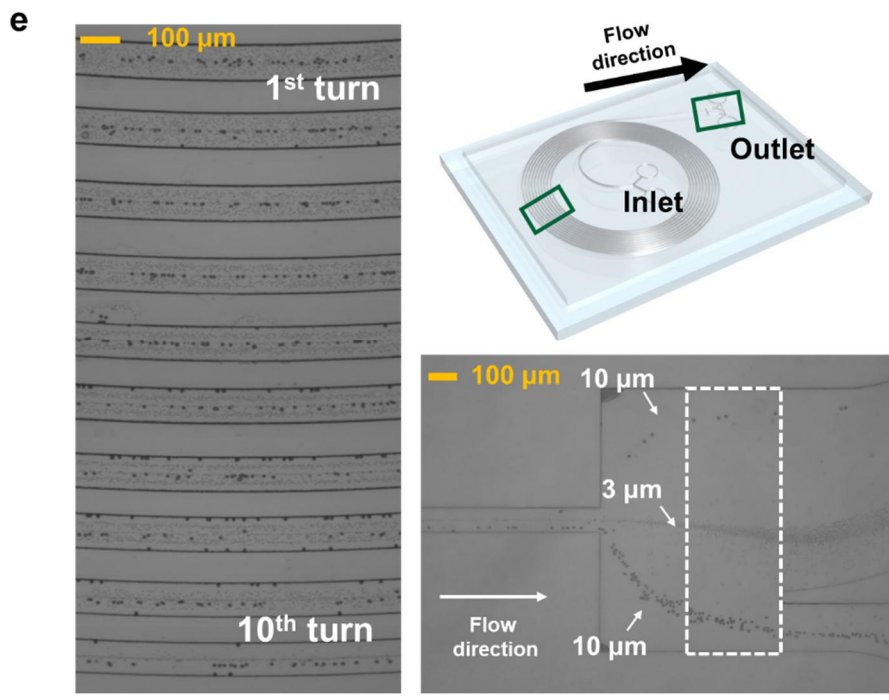


Figure 2.16 (continued.)

f

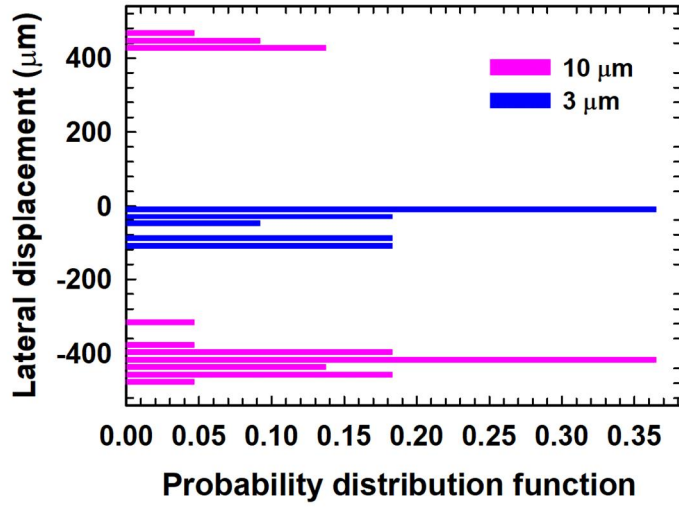


Figure 2.16 (continued.)

2.4.3. ‘Self-ordering’ behavior in the ‘self-secreted’ substances

The blockage ratio (D_p/D_h), which is defined as the ratio of the particle size to the hydrodynamic channel height, is also an important factor for the preferential particle focusing because particle focusing occurs at a blockage ratio larger than 0.07 [40]. Therefore, distribution of particles was compared with that of cells under the same experimental conditions to investigate the difference between the behavior of the rigid particles (diameter = 3 μm) and that of the deformable particles in the EPS. The deformable particle used in the experiment was a microbial cell, *Chlorella vulgaris* (diameter 2 – 4 μm) that was employed for the EPS extraction. At a position of 5 cm downstream from the inlet, images were obtained with a flow rate of 50 $\mu\text{l hr}^{-1}$ (**Figure 2.17**). There was no observable focusing behavior for the synthetic rigid particle since the particle had a blockage ratio of 0.06 as shown in **Figure 2.18a**. In contrast to the synthetic rigid particle, deformability of the particle can cause an additional wall lift force near the wall in the applied flow field [41-43]. The resulting ‘self-ordering’ phenomenon (**Figure 2.17a**) is originated from the asymmetric object driven flow disturbance [44] in the rectangular flow field (**Figure 2.17a**). **Figure 2.17c** and **Figure 2.17f** show the schematic illustration of the force balance in the cross-section of channel when *C. vulgaris* and PS particle migrate under viscoelastic flow, respectively. The deformable cell induces an additional wall lift force near the wall in the applied flow field in contrast to the particles.

Additional experiment was carried out with *Chlorella vulgaris* in order to expand the approach demonstrated in this study (**Figure 2.18**). Cell migration was examined under a flow rate of 400 $\mu\text{l hr}^{-1}$ in a spiral microchannel. In a confined spiral microchannel, the equilibrium position of particles flowing within the viscoelastic medium is determined by the balance between the Dean drag force ($\vec{F}_D \approx 6\pi\mu D_p v D e_p^2 / D_h$) and the viscoelastic force ($\vec{F}_E \approx D_p^3 \nabla N_1$). Therefore, the equilibrium position of particles changes depending on the particle size. According

to the previous report [24], the normalized Dean force is expressed with the channel aspect ratio (γ) and the blockage ratio (D_p/D_h). Here, the blockage ratio is a parameter to determine whether a particle migration occurs owing to the interaction between \vec{F}_D and \vec{F}_E or not. Lee *et al.*[24] demonstrated that the Dean force increases remarkably when the blockage ratio is higher than 0.06 with a channel ratio of 0.25 leading to lateral migration of the particle.

It turned out that *Chlorella vulgaris* was aligned at center after the first turn. The probability distribution function showed that there was no difference in the equilibrium positions of the cell after the first turn and the tenth turn. The deformation of the cell induced by the hydrodynamic force enhanced cell focusing phenomenon, compared with the rigid particles.

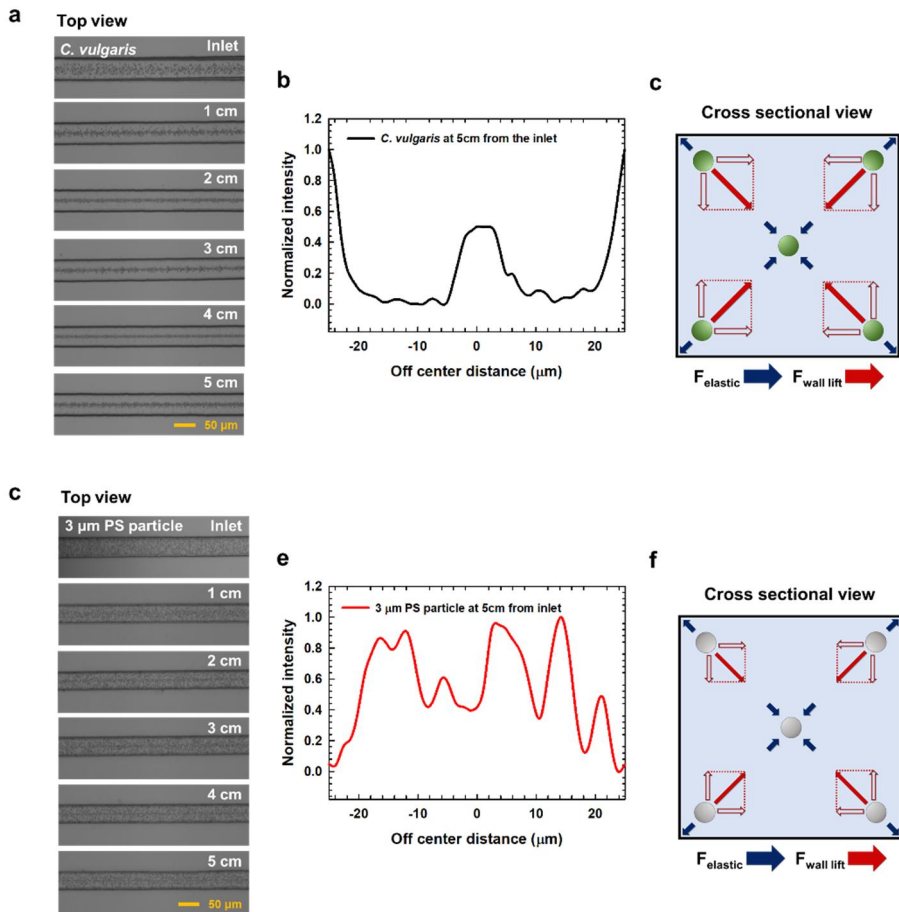


Figure 2.17 (a) Experimental results of *Chlorella vulgaris* in the self-secreted EPSs with a flow rate of $50 \mu\text{l hr}^{-1}$ ($Re = 0.0191$, $Wi = 22.2$). (b) Probability distribution function of *chlorella vulgaris* at a 5 cm position away from the entrance, showing cell focusing at the center. (c) Schematic illustration of the force balance in the cross-section of channel when *Chlorella vulgaris* migrates under viscoelastic flow. (d) Experimental results of PS particles in the EPS with a flow rate of $50 \mu\text{l hr}^{-1}$ ($Re = 0.0191$, $Wi = 22.2$). (e) Probability distribution function of PS particles at a 5 cm position away from the entrance, showing random positions. (f) Schematic illustration of the force balance in the cross-section of channel when rigid particle migrates under viscoelastic flow.

a

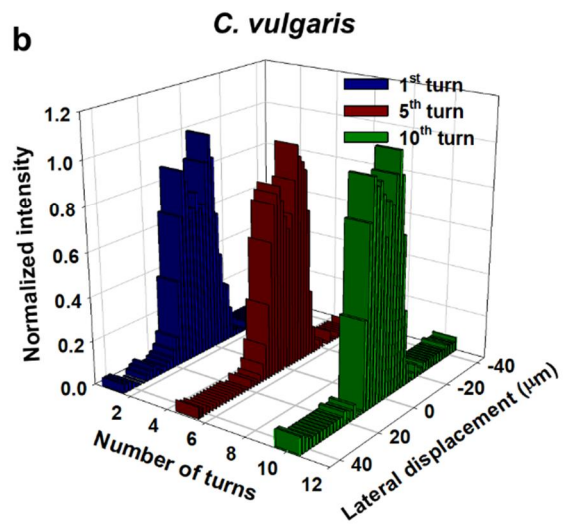
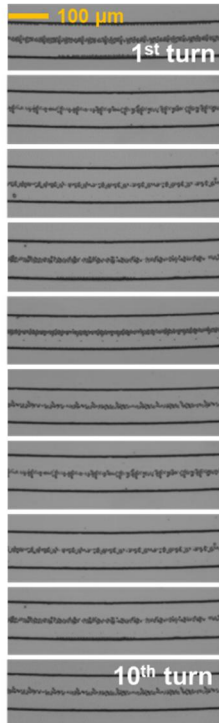


Figure 2.18 (a) Experimental results of *Chlorella vulgaris* in the EPSs with a flow rate of $400 \mu\text{l hr}^{-1}$ ($Re = 0.122$, $Wi = 88.9$). (b) Probability distribution function of *Chlorella vulgaris*, showing enhanced focusing behavior along the centerline of the channel.

2.4.4. Autonomous cell-sorting in the microchannel

For the separation of cells with a wide size distribution, *Sphaerocystis schroeteri*, a genus of green algae with 1 to 30 μm diameter was selected and employed. The cells with various sizes were injected into the spiral microchannel at a flow rate of $400 \mu\text{l hr}^{-1}$. It was observed in the first turn that the larger cells were located on the wall of the channel. The cells were focused by the hydrodynamic force faster than rigid particles due to the deformability and shape of cells [19]. The streak positions of the cells observed in the tenth turn indicated that multiplexing cell focusing was accomplished with respect to the size (**Figure 2.19**). The equilibrium position of the larger cell ($>16\mu\text{m}$) was situated at the outer side of the channel by the Dean Drag force. In addition, the equilibrium position was located at the middle or between the middle and the outside of the microchannel when diameter of the cells was smaller than $16 \mu\text{m}$. Consequently, autonomous cell-sorting was achieved using the self-secreted biomaterials. Indeed, this cell-focusing/sorting system is sustainable and efficient because the self-produced macromolecules are employed for the cell suspension.

Probability distribution of the cells at the outlet is illustrated in Figure 8b. The small cells were mostly distributed in area 3 (55.3%) due to the viscoelastic force. When the cells form a long cluster ($10 - 15 \mu\text{m}$), they were mainly placed in area 1 (28.5%) or in area 4 (42.85%). When the cells have a diameter larger than $16\mu\text{m}$, they were all located in area 5.

Live cells are deformable, which can lead to additional lift forces in contrast to rigid particles. The additional force originates from the flow disturbance due to the shape change of cells [45, 46]. In general, three dimensionless parameters can be used to characterize the relative deformation of a droplet: (1) the Weber number, $We = \frac{\rho U^2 a}{\sigma}$ (inertial stress vs. surface tension), where a is the droplet diameter, (2) the Capillary number, $Ca = \frac{\mu U a}{\sigma h}$ (viscous stress vs. surface tension), and (3) the viscosity ratio, $\lambda_d = \mu_d / \mu$, where μ_d is the dynamic viscosity of fluid inside the

droplet. The lift force induced by the deformability is given by $\overrightarrow{F_{L,d}} \approx Ca\mu Ua \left(\frac{a}{H}\right)^3 \left(\frac{d}{H}\right) f(\lambda_d)$, where d is the distance between the drop and the center of channel [47]. Here, $f(\lambda_d) = \frac{16\pi}{(\lambda_d+1)^3} \left[\frac{11\lambda_d+10}{140} (3\lambda_d^3 - \lambda_d + 8) + \frac{3}{14} \frac{19\lambda_d+16}{3\lambda_d+2} (2\lambda_d^2 - \lambda_d - 1) \right]$ [47-49]. When $\lambda_d < 1$ or $\lambda_d > 10$, the deformability-induced lift force is imposed towards the center of channel [49]. Green algae such as *Lactococcus lactis* have a cellular viscosity of 6 mPa·s [50], which implies that the viscosity ratio is 0.4. As a result, the cells tend to move towards the centerline of channel due to the deformability induced lift force. For this reason, the cells and PS particles have different range of sizes for separation.

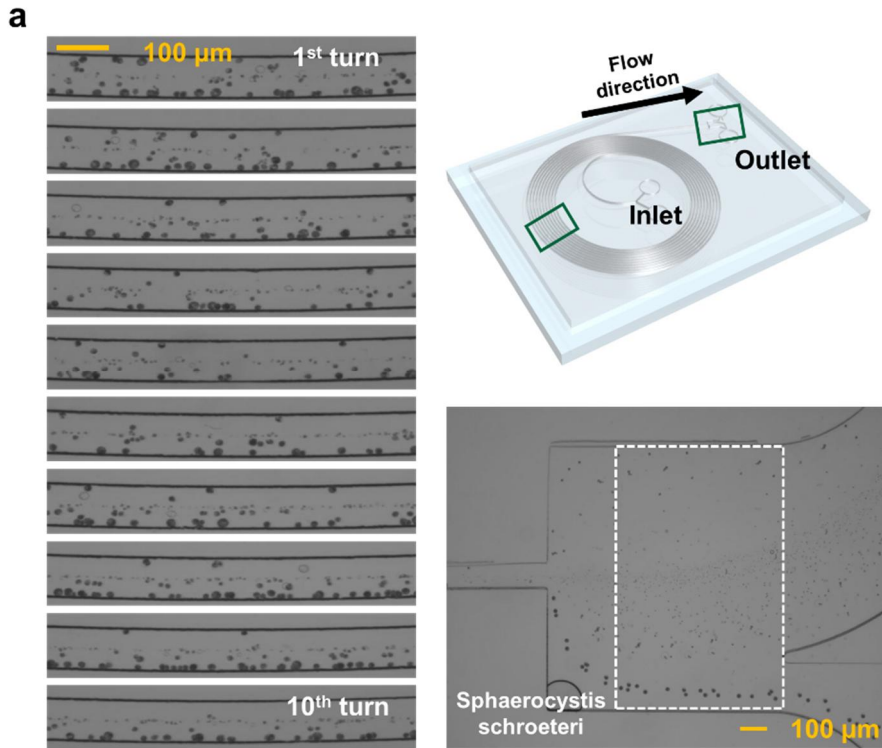


Figure 2.19 Autonomous cell-sorting using the self-secreted macromolecules. (a) Microscopic images of the cells in the EPS solution with a flow rate of $400 \mu\text{l hr}^{-1}$ ($Re = 0.122$, $Wi = 88.9$). The superimposed images illustrate the distribution and position of the cells with different sizes in the channel. (b) Probability distribution function of the cells at the outlet of the channel. (c) Separation efficiency of the cells. The graph demonstrates the ratio of the cells moving to a specific area (area 1: 540 to 300 μm , area 2: 300 to 100 μm , area 3: 100 to -100 μm , area 4: -100 to -300 μm , and area 5: -300 to -540 μm).

b

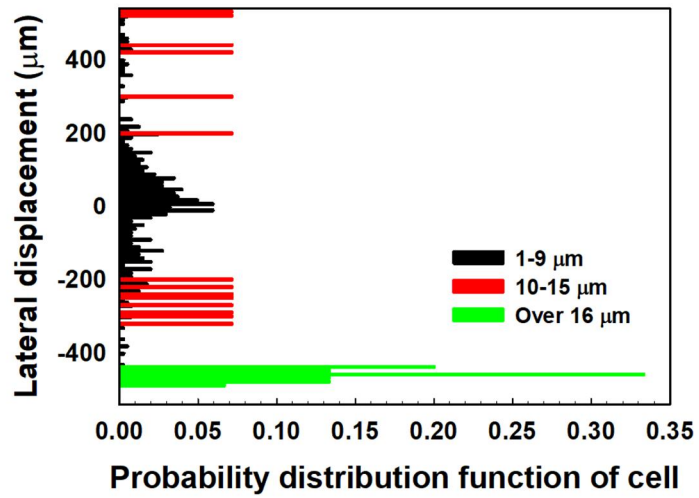


Figure 2.20 (continued.)

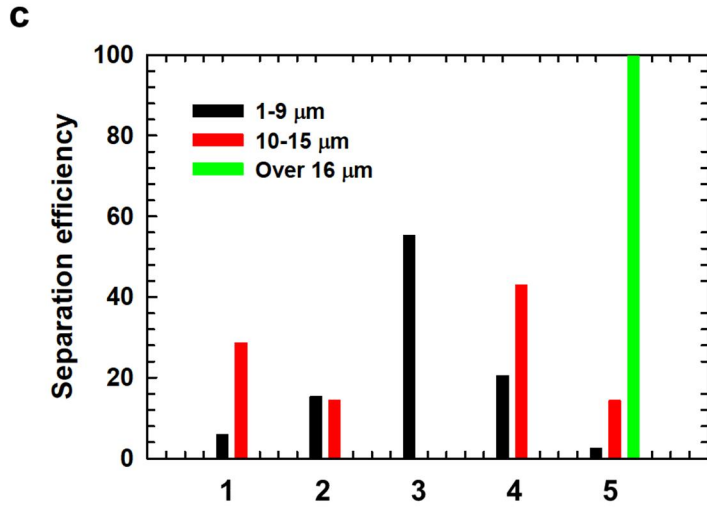


Figure 2.20 (continued.)

2.5. Conclusion

We demonstrated autonomous cell-sorting in a microfluidic device using the EPSs excreted by algae. Enhanced particle focusing and separation of rigid particles were also investigated with use of the self-secreted macromolecules. The extracted EPS were examined through chemical, structural, and rheological analyses. The correlation between the viscoelastic properties of EPS and the particle migration was explored. It was found that the EPS prepared in this study could induce the multiplex focusing of particles with different sizes in the microfluidic device. This is attributed to the viscoelasticity of EPS produced by microorganisms. More specifically, the experimental results verified that the EPSs had higher structural stability and longer relaxation time than synthetic polymers with a similar zero-shear viscosity. It is expected that this study will provide a promising method to deal with cells for biomedical, pharmaceutical, and clinical applications.

2.6. Bibliography

- [1] I.S. Roberts, *Annual Reviews in Microbiology*, 50 (1996) 285-315.
- [2] C. Whitfield, M.A. Valvano, *Advances in microbial physiology*, 35 (1993) 135-246.
- [3] T.K. Singha, *IOSR J Pharm*, 2 (2012) 271-281.
- [4] H.-C. Flemming, T.R. Neu, D.J. Wozniak, *Journal of bacteriology*, 189 (2007) 7945-7947.
- [5] C. Mayer, R. Moritz, C. Kirschner, W. Borchard, R. Maibaum, J. Wingender, H.-C. Flemming, *International journal of biological macromolecules*, 26 (1999) 3-16.
- [6] I.W. Sutherland, *Trends in microbiology*, 9 (2001) 222-227.
- [7] V. Körstgens, H.-C. Flemming, J. Wingender, W. Borchard, *Journal of microbiological methods*, 46 (2001) 9-17.
- [8] I.B. Bekard, P. Asimakis, J. Bertolini, D.E. Dunstan, *Biopolymers*, 95 (2011) 733-745.
- [9] D.E. Smith, H.P. Babcock, S. Chu, *Science*, 283 (1999) 1724-1727.
- [10] J.Y. Kim, S.W. Ahn, S.S. Lee, J.M. Kim, *Lab on a Chip*, 12 (2012) 2807-2814.
- [11] A.S. Hossain, A. Salleh, A.N. Boyce, P. Chowdhury, M. Naquiuddin, *American journal of biochemistry and biotechnology*, 4 (2008) 250-254.
- [12] A.J. McCormick, P. Bombelli, A.M. Scott, A.J. Philips, A.G. Smith, A.C. Fisher, C.J. Howe, *Energy & Environmental Science*, 4 (2011) 4699-4709.
- [13] P. Bombelli, M. Zarrouati, R.J. Thorne, K. Schneider, S.J. Rowden, A. Ali, K. Yunus, P.J. Cameron, A.C. Fisher, D.I. Wilson, *Physical Chemistry Chemical Physics*, 14 (2012) 12221-12229.
- [14] U. Passow, *Progress in oceanography*, 55 (2002) 287-333.
- [15] A. Drews, C.-H. Lee, M. Kraume, *Desalination*, 200 (2006) 186-188.
- [16] T. More, J. Yadav, S. Yan, R. Tyagi, R. Surampalli, *Journal of environmental management*, 144 (2014) 1-25.
- [17] H. Liu, H.H. Fang, *Journal of biotechnology*, 95 (2002) 249-256.
- [18] S. Jachlewski, W.D. Jachlewski, U. Linne, C. Bräsen, J. Wingender, B. Siebers, *Frontiers in bioengineering and biotechnology*, 3 (2015) 123.
- [19] M.J. Kim, J.R. Youn, Y.S. Song, *Lab on a Chip*, 18 (2018) 1017-1025.
- [20] M. DuBois, K.A. Gilles, J.K. Hamilton, P.t. Rebers, F. Smith, *Analytical chemistry*, 28 (1956) 350-356.
- [21] M. Doi, S.F. Edwards, *The theory of polymer dynamics*, oxford university press, 1988.
- [22] M. Rubinstein, R.H. Colby, *Polymer physics*, Oxford University Press New York, 2003.
- [23] J.C. McDonald, G.M. Whitesides, *Accounts of chemical research*, 35 (2002) 491-499.
- [24] D.J. Lee, H. Brenner, J.R. Youn, Y.S. Song, *Scientific reports*, 3 (2013).
- [25] J. Wingender, M. Strathmann, A. Rode, A. Leis, H.-C. Flemming, *Methods in enzymology*, 336 (2001) 302-314.
- [26] B. Frølund, R. Palmgren, K. Keiding, P.H. Nielsen, *Water research*, 30 (1996) 1749-1758.
- [27] Y. Liu, H.H. Fang, (2003).
- [28] S. Comte, G. Guibaud, M. Baudu, *Enzyme and Microbial Technology*, 38 (2006) 237-245.

- [29] G.-P. Sheng, H.-Q. Yu, Z. Yu, *Applied microbiology and biotechnology*, 67 (2005) 125-130.
- [30] S. Deng, R. Bai, X. Hu, Q. Luo, *Applied microbiology and biotechnology*, 60 (2003) 588-593.
- [31] K. Zhou, Y. Hu, L. Zhang, K. Yang, D. Lin, *Scientific reports*, 6 (2016).
- [32] A. Omoike, J. Chorover, *Biomacromolecules*, 5 (2004) 1219-1230.
- [33] N. Abu□Lail, T. Camesano, *Journal of Microscopy*, 212 (2003) 217-238.
- [34] E.R. Morris, *Carbohydrate Polymers*, 13 (1990) 85-96.
- [35] V. Svetličić, V. Žutić, T.M. Radić, G. Pletikapić, A.H. Zimmermann, R. Urbani, *Marine drugs*, 9 (2011) 666-679.
- [36] C.-C. Hsieh, A. Balducci, P.S. Doyle, *Nano letters*, 8 (2008) 1683-1688.
- [37] K. Kang, S.S. Lee, K. Hyun, S.J. Lee, J.M. Kim, *Nature communications*, 4 (2013) 2567.
- [38] S. Yang, J.Y. Kim, S.J. Lee, S.S. Lee, J.M. Kim, *Lab on a Chip*, 11 (2011) 266-273.
- [39] G. D'Avino, G. Romeo, M.M. Villone, F. Greco, P.A. Netti, P.L. Maffettone, *Lab on a Chip*, 12 (2012) 1638-1645.
- [40] M.J. Kim, D.J. Lee, J.R. Youn, Y.S. Song, *RSC Advances*, 6 (2016) 32090-32097.
- [41] A. Karnis, H. Goldsmith, S. Mason, *Nature*, 200 (1963) 159-160.
- [42] D. Di Carlo, D. Irimia, R.G. Tompkins, M. Toner, *Proceedings of the National Academy of Sciences*, 104 (2007) 18892-18897.
- [43] S. Yang, S.S. Lee, S.W. Ahn, K. Kang, W. Shim, G. Lee, K. Hyun, J.M. Kim, *Soft Matter*, 8 (2012) 5011-5019.
- [44] L. Leal, *Annual Review of Fluid Mechanics*, 12 (1980) 435-476.
- [45] H. Amini, W. Lee, D. Di Carlo, *Lab on a Chip*, 14 (2014) 2739-2761.
- [46] C.K. Tam, W.A. Hyman, *Journal of Fluid Mechanics*, 59 (1973) 177-185.
- [47] P.-H. Chan, L. Leal, *Journal of Fluid Mechanics*, 92 (1979) 131-170.
- [48] C.A. Stan, A.K. Ellerbee, L. Guglielmini, H.A. Stone, G.M. Whitesides, *Lab on a Chip*, 13 (2013) 365-376.
- [49] J. Zhang, (2015).
- [50] A. Cuecas, J. Cruces, J.F. Galisteo-López, X. Peng, J.M. Gonzalez, *Biophysical journal*, 111 (2016) 875-882.

Chapter 3

Optorheology of photosynthetic bacterium suspension

3.1. Introduction

It is critical to understand the characteristics of a complex fluid in science and engineering since they are closely correlated with internal structure of the matter. Rheology, a study about the deformation and flow of matters including both solids and liquids, can provide a key knowledge for optimal performance and processing conditions of materials. More specifically, the rheology of a suspension is capable of giving some information on the internal structure of the liquid based on continuum mechanics, such as particle size, polydispersity, shape, volume fraction, and charge. For example, the particle-particle interaction in colloidal systems acts as a major factor to determine the rheological behavior of the system. Depending on attractive and/or repulsive forces between particles, rheological behavior of the suspension is changed. In particular, at a low shear rate the interparticle interactions dominate the behavior of liquids, e.g., viscosity.

The viscosity of liquids generally varies with external fields such as electric field, magnetic field, temperature gradient, *etc.* [1]. For instance, the fluidic components in electrorheological (ER) or magnetorheological (MR) fluids align along with the corresponding external fields, resulting in increasing the fluid viscosity [2]. The effect of electric and/or magnetic fields on the viscosity of liquids has been studied for many applications such as damping, hydraulic valves, and energy harvesting technologies [3-5].

On the other hand, optical stimuli have not been focused on to control the rheological properties of matters thus far. Recently, it has been only reported that the mechanical properties of cell surface could be changed by using light [6]. *F. Wottawah et al.* [6] harnessed a laser beam as an optical stretcher in order to apply stress to cells, resulting in axial elongation along the laser axis.

The aim of this paper is to offer a new potential for manipulating the rheological features of a complex fluid with use of light. We report a light active colloid by employing *Synechocystis* sp. PCC 6803, where the fluid viscosity changes in response to light. The change in the light induced viscosity of the cell suspension is due to the electron produced by light and the resulting electron accumulation and transport (**Figure 3.1**). In order to maximize the effect of the charged electrons on the cell, an external electric field was applied. This is the first report to show the optorheological behavior of photosynthetic bacterium suspension.

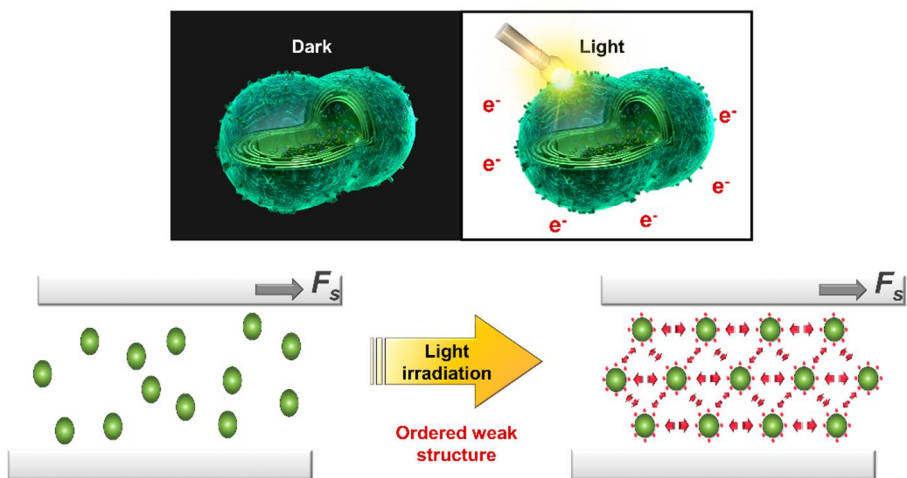


Figure 3.1. Schematic diagram of the optorheology introduced in this study.

3.2. Experimental

3.2.1. Bacterial culture

A wild-type strain of *Synechocystis* sp. PCC 6803 (Hereafter, *Synechocystis*) was obtained from Prof. Y.-I. Park of Chung-Nam National University, Daejeon, Korea. The cell was grown on 1% BG-11 agar plates buffered with 0.3% (w/v) sodium thiosulphate ($\text{Na}_2\text{S}_2\text{O}_3$) under white LED light for 14 days. After that, the cells were re-suspended in a 1% BG 11 medium. One week after the re-suspension process, the cell density was set to 1.5×10^8 cells/ml.

3.2.2. Characterization of photosynthetic bacterium suspension

The morphology of the cell was characterized by using field emission scanning electron microscopy (FE-SEM; JSM-7600F, JEOL Ltd., Japan). The absorption spectrum of the cell was examined by using a UV-vis spectrometer (V-770, JASCO, Japan). The zeta potential of the cell was measured using a Nano-ZS Zetasizer (Malvern Instruments Ltd., UK).

Electrochemical impedance spectroscopy (EIS) measurements were conducted with an electrochemical device which was composed of a Pt mesh anode (Ametek, TN, USA), an anodic chamber, and a membrane electrode assembly cathode (**Figure 3.2**). The cell suspension was injected into the anodic chamber. The impedance spectrum of the cell suspension was acquired using a potentiostat (VersaStat3, Princeton Applied Research, USA). The EIS measurement was made in the frequency range of 100 kHz to 100 Hz with an amplitude of 10mV. The Nyquist plots and EIS parameters were obtained by using the software Z-View. The amperometric response was obtained as a function of time with 510 Ω under alternative light and dark conditions.

The rheological properties were measured by using a rheometer (AR2000 Advanced Rheometer, TA Instruments) with a cup (diameter = 30.0 mm and height = 30.0 mm), a concentric cylinder conical geometry (diameter = 28.0 mm and internal height = 30.0 mm) and a function generator (Stanford Research Systems, DS345). The light was irradiated for 15 min by using a halogen lamp (**Figure 3.3**). We set two different light conditions with the light intensity of 48.75 and 11.55 W/m². The gap distance between the cup and the rotor of geometry was fixed at 1.00 mm.

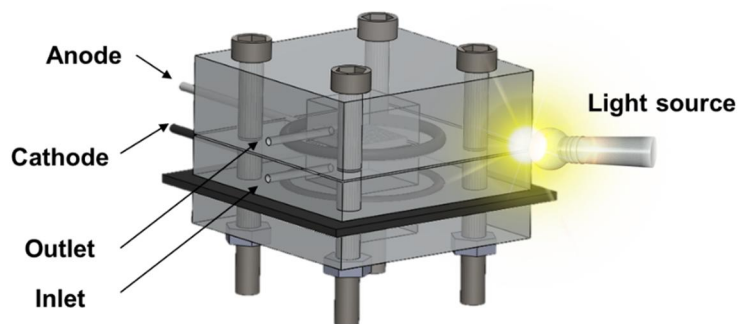


Figure 3.2 Schematic diagram of the electrochemical device. The light is irradiated to the side of the anodic chamber with an intensity of 48.75 W/m^2 .

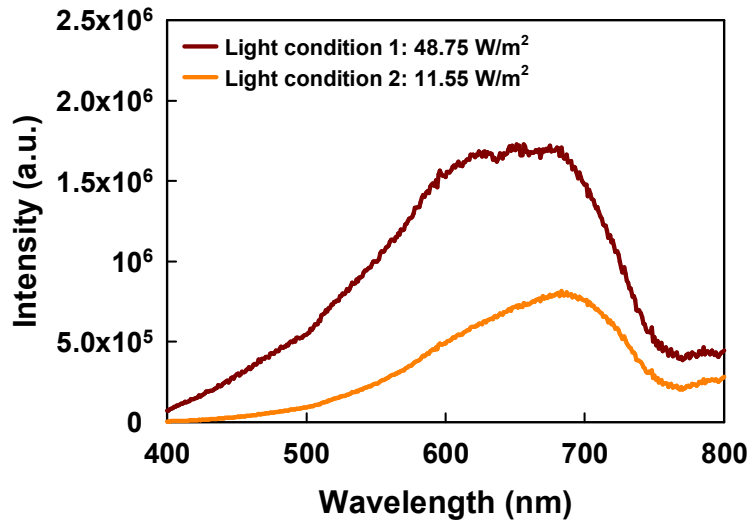


Figure 3.3 Irradiance spectrum of the halogen lamp employed in this experiments.

3.2.3. Microscopic characterization of photosynthetic bacterium suspension

The AC-electric field induced alignment of the cell was observed by using an inverted optical microscope (IX53, Olympus). The images were acquired with a high-speed fluorescence camera (AcquCAM 23G, JNOPTIC co.,Ltd) employing an image software package (JNOPTIC Capture 2.4). The ImageJ (NIH) software was used for image processing in order to determine the total electrical energy during cell assembly.

The experimental setup consisted of two coplanar gold electrodes separated by a 1 mm gap. The device was filled with the cell suspension, and an AC-electric field of 3 V mm^{-1} , 50 Hz was applied.

3.3. Numerical analysis

The total electrical energy of cell configuration under the AC-electric field was simulated by using Comsol Multiphysics 5.3a. The electric field distribution was calculated by solving the following Laplace equation:

$$\nabla^2 \varphi = 0$$

The local electric energy density is expressed as

$$w_{es} = \frac{1}{2} DE = \frac{1}{2} \varepsilon_0 E^2$$

where D is the electric displacement, E is the electric field, and ε_0 is the permittivity of vacuum. The total electrical energy was obtained by integrating the local electric energy density as shown below.

$$w_e = \int w_{es} dV$$

Here, the Carreau model was used to simulate the rheological behavior of non-Newtonian fluids.

$$\mu = \mu_\infty + (\mu_\infty + \mu_0)(1 + (\lambda + \dot{\gamma})^a)^{\frac{n-1}{a}}$$

where p is the pressure, u is the velocity, μ is the viscosity of liquid, μ_∞ is the infinite shear viscosity, μ_0 is zero shear viscosity, λ is a time constant, $\dot{\gamma}$ is a shear rate, and n is an exponent.

The cell dimensions are set to spherical spheres ($R = 1 \mu\text{m}$) fused in two parts with a center spacing of $1 \mu\text{m}$ (**Figure 3.4**). The three different configurations of the cell assembly were taken into account based on the experimental results. The system geometry is set to a rectangular box having two gold electrodes located at the both top and bottom. The AC-electric field is applied to the top layer of the electrode about 3v, 50 Hz. Electric insulation was assumed for the left and right sides of the simulation domain.

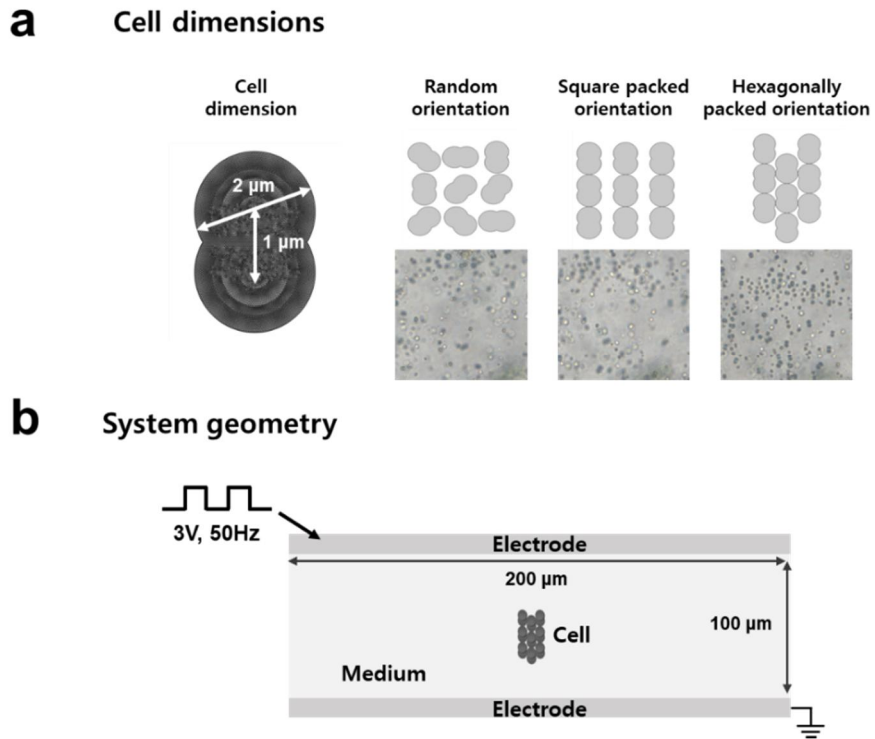


Figure 3.4 Geometry specification for numerical simulations. (a) Cell structure developed for modeling. Different configuration of *Synechocystis* self-assembly in the external AC-electric field. (b) System geometry for modeling.

3.4. Results and discussion

3.4.1. Photosynthetic bacterium suspension

Photosynthetic bacteria, which are the most numerous living organisms on Earth, obtain their power through photosynthesis. They employ light, water, and carbon dioxide to yield electrons by performing water photolysis. One of the photosynthetic bacteria, *Synechocystis* is capable of producing electron through photosynthesis. Two fundamental chlorophyll (Chl) pigments, mainly chlorophyll a (Chl a) and chlorophyll b (Chl b) were expressed in *Synechocystis* function as a light-harvesting antenna (**Figure 3.5**) [7]. The cell has a coccoid appearance with pili, and its size varies from 1 to 2 μm . By using the pili, it releases electron to the exterior. Therefore, the electrophoretic feature of *Synechocystis* changes depending on the surface properties during photosynthesis.

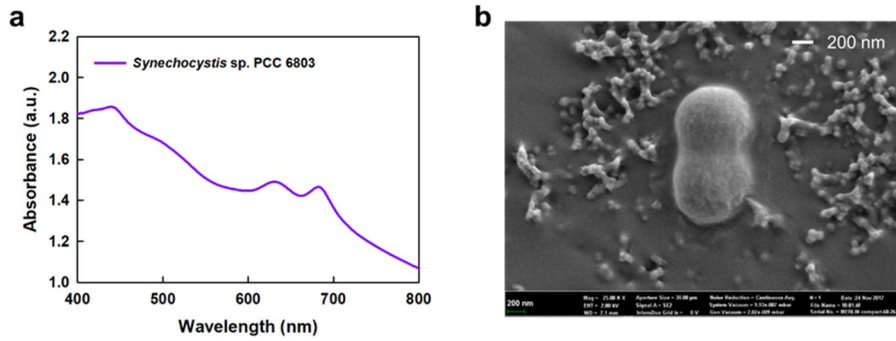


Figure 3.5 Characterization of the cell. (a) Absorption spectrum of *Synechocystis* sp. PCC 6803. It denotes that both chlorophyll (Chl) a and b pigments accumulate in a *Synechocystis* sp. PCC 6803 strain. (b) Scanning electron microscopy (SEM) of *Synechocystis* sp. PCC 6803 showing extracellular appendages. It is peanut-shaped particle composed of two-partially fused spherical lobes in shape. The scale bar represents the length of 200 nm.

3.4.2. Electrophoretic surface properties of photosynthetic bacterium suspension

Zeta potential, a key indicator of the stability of particle suspensions, generally represents the surface property of particles [8]. Since the cells are covered with extracellular polymeric substances (EPS), the classical electric double layer concept is not appropriate for *Synechocystis* [9, 10]. Consequently, the zeta potential cannot directly indicate the surface property of the cell. *Ohshima et al.* [9] introduced the “soft-particle theory”, and *Planchon et al.* [10] revealed that the magnitude of the surface potential of cell is roughly 1/20 of the zeta potential of the cell. Therefore, we measured the zeta potential to determine the surface potential in this study (**Figure 3.6**). It was confirmed that the surface potential of the cell was varied according to the presence or absence of light (**Figure 3.7a**). It was also found that the surface potential was increased by 1.14 folds in light condition compared to dark condition. In other words, the physical properties of the cell suspension are changed when the light is applied. This is attributed to a change in the states of the cell dispersed in the fluid as a result of the photosynthetic activity and the light-induced response as aforementioned.

Additional investigation into the photosynthetic bacterium suspension was carried out with use of electrochemical impedance spectroscopy (EIS). **Figure 3.7b** shows the Bode plots in the light and dark conditions. In the low frequency region below 100 Hz, the Warburg impedance was detected. As a result, the frequency region above 100 Hz was plotted in the figure. It was found that the impedance of the suspension was varied depending on the existence or absence of light. The electrochemical reaction of the photosynthetic bacterium decreased the impedance apparently. The Nyquist plots also demonstrated the different states of cell suspension depending on the light condition (**Figure 3.7c**). The inset represents the equivalent electrical circuit obtained by the parametric analysis. Equivalent circuit modelling was carried out in order to figure out the change in the internal structure of the bacterium suspension when light was applied. **Table 3.1** lists the electrochemical components of the equivalent circuit from Figure 2c, where R_{ct} is the charge transfer resistance, CPE_E is the constant phase

element, C_{DL} is the double layer capacitance for the working electrode, R_s is the resistance for cell suspension. The results demonstrated that when the light was applied, the resistance of the suspension had a lower resistance than the sample in the dark condition. This result is consistent with the electrical conductivity results described in **Figure 3.6**. Moreover, the amperometric response indicated the dependence of the cell surface properties on the light (**Figure 3.8**). As the light intensity increased, it simulated the photosynthetic activity of cells, resulting in a higher photoresponse current. That is, the amount of electrons emitted by the cells was determined according to the intensity of the light. The results validated that the bacteria generate and transfer electrons to the exterior under light, which results in decreasing the electric surface resistance of the cells. It also confirmed that the surface properties of cells depended on the light intensity.

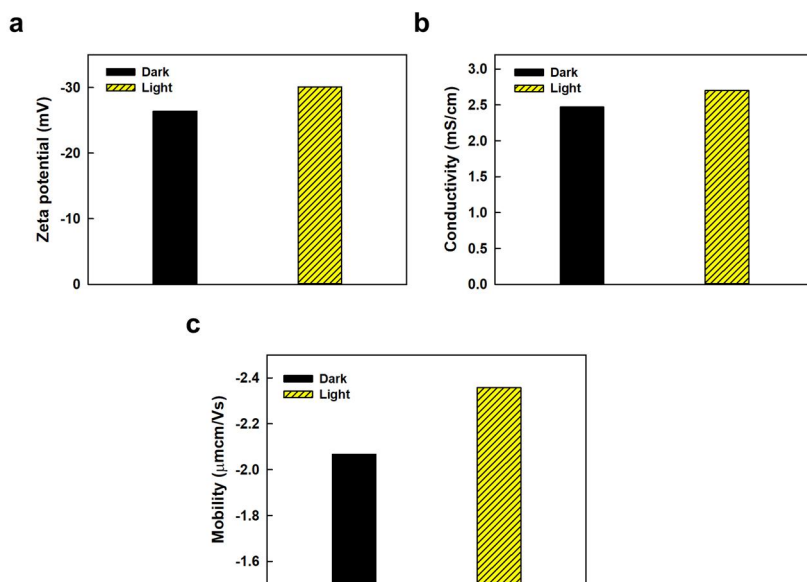


Figure 3.6 Electrophoretic properties of the cell: (a) zeta potential, (b) electrical conductivity, and (c) mobility under dark and light conditions. The results demonstrate that the surface properties of the cell are changed due to photosynthesis.

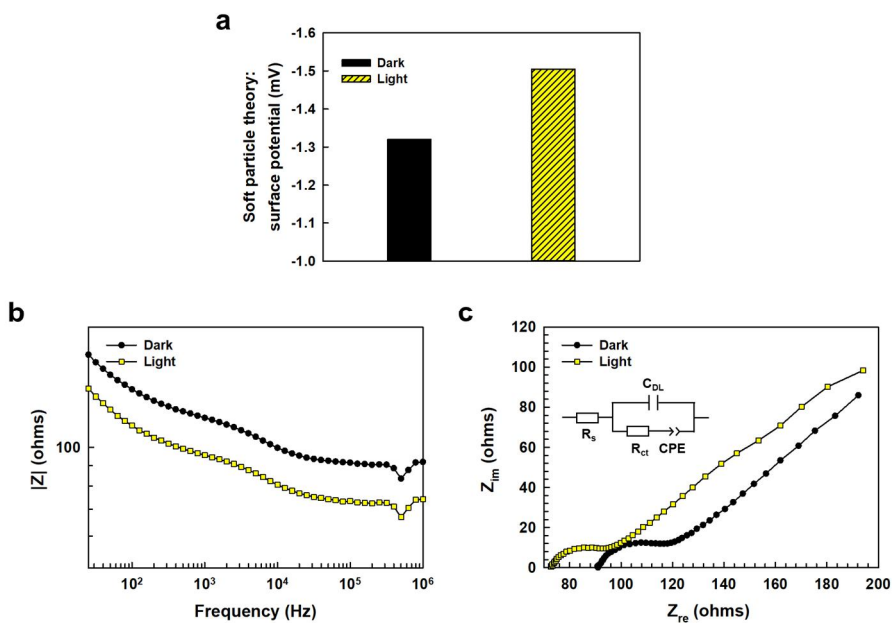
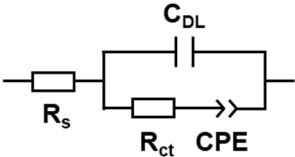


Figure 3.7 Electrophoretic properties of photosynthetic bacterium suspension change under the light irradiation. (a) Surface potential of the cells calculated from the soft particle theory. Impedance spectra of the bacterium suspension according to the light condition. (b) Bode plot and (c) Nyquist plot of the photosynthetic bacterium suspension. The inset represents the equivalent circuit model.

Table 3.1 The equivalent circuit model, and the values of the electrochemical components.

| Equivalent circuit | Calculated impedance data | Light condition | | |
|---|---------------------------|-------------------|-------------------------|-------------------------|
| | | Dark | Light | |
|  | Working electrode | $R_{ct} (\Omega)$ | 21.34 | 17.88 |
| | | $CPE_E - C (F)$ | 0.0010025 | 0.001162 |
| | | $CPE_E - P$ | 0.5186 | 0.52074 |
| | | $C_{DL} (F)$ | 1.0473×10^{-6} | 1.1401×10^{-6} |
| | Cell suspension | $R_s (\Omega)$ | 92.74 | 73.75 |

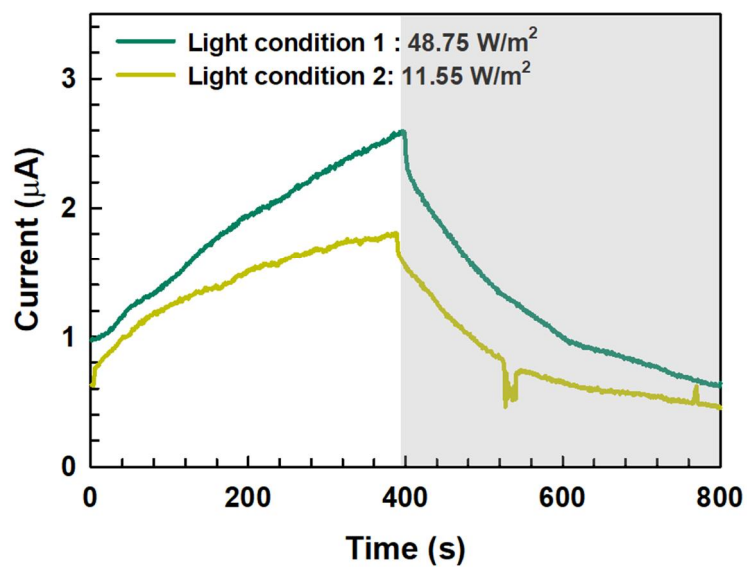


Figure 3.8 Photoresponse of the electrochemical device loaded with *Synechocystis* sp.. The measurement was made for 400 s light/dark interval.

3.4.3. Rheological properties of photosynthetic bacterium suspension

The change in the electrophoretic properties of *Synechocystis* leads to changing the rheological property of the cell suspension. **Figure 3.9a** shows the light effect on the viscosity of the cell suspension. The sample suspensions all showed the non-Newtonian behaviors. When light was on, the viscosity of the suspension dramatically increased. In particular at a low shear rate, viscosity significantly increased due to the change of electrophoretic properties induced by the photosynthesis. This observation indicates that photoelectrochemically generated electrons enhance the stability and dispersity of cells, which results in an increase in viscosity. At a high shear rate, the viscosity difference between the presence and absence cases of light was reduced due to the collapse of the spatial arrangement. In colloidal systems, when the magnitude of the zeta potential is increased, particles themselves are repelled, resulting in restricting the movement of the particles (**Figure 3.9b**). In this sense, the viscosity is increased in the low shear rate region. Therefore, it can be seen that the change in the physical properties of the cell by the light affects the spatial arrangement, thus boosting the viscosity.

In addition, further experiments were carried out to investigate the effect of the light intensity on the viscosity. For measurements, a different light intensity, 11.55 W/m² was applied, which was about 4.2 times lower than that of the previous state. As mentioned earlier, the increased light intensity intensifies the photoactivity of cells, which enhanced the current production (**Figure 3.8**). It was revealed that the viscosity of the cell suspension increased with an increase in the light intensity (**Figure 3.10**). The influence of the light on the viscosity may be interpreted considering the net charges of the cells. The results suggest that the change in the electrophoretic properties of cell is a key factor for designing rheological behavior of suspensions.

In order to maximize the influence of the surface feature on the viscosity, AC-electric field was applied (**Figure 3.11a**). It turned out that the network structure in the suspensions was formed by the dielectrophoretic force (F_{DEP}) of electrons. On the other

hand, both the suspensions showed yield behavior rheologically. Since the polar group of the cell surface acts as an electrically active part, the cell is capable of aligning into linear chains along the direction of the electric field by dipole–dipole attraction. Under light, the cell possesses net charges, arising from photosynthesis. In other words, the increased conductivity or dielectric properties of cell enhance the polarization of cell. The more polarized dipoles in cells in the suspension generate higher ordered network structure under the electric field, inducing an increase in viscosity. That is, the light irradiation was found to act as an active stimulus to control the viscosity of the cell suspension. During photosynthesis reaction, mobile electrons are accumulated on the surface of the cells. Consequently, the rheological characteristics of the living cell suspension can be controlled using light. This implies “optorheology” of the photosynthetic cell suspension.

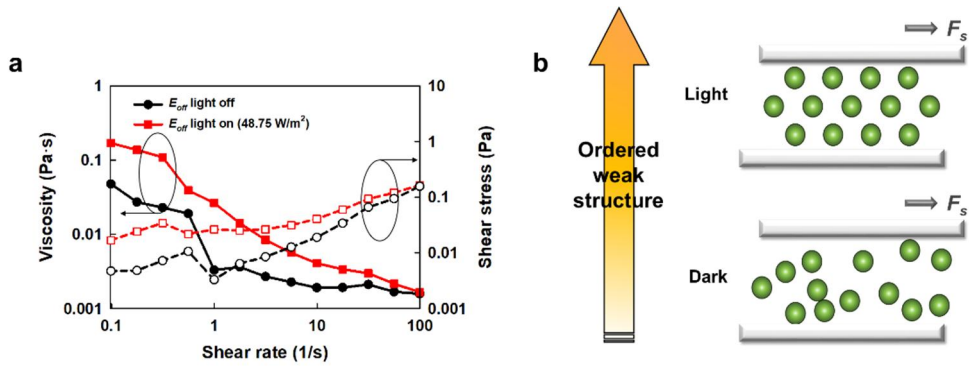


Figure 3.9 Rheological characterization of the cell suspensions. (a) Viscosity and shear stress as a function of shear rate. (b) Schematic diagram of the spatial arrangement change of the cell suspension.

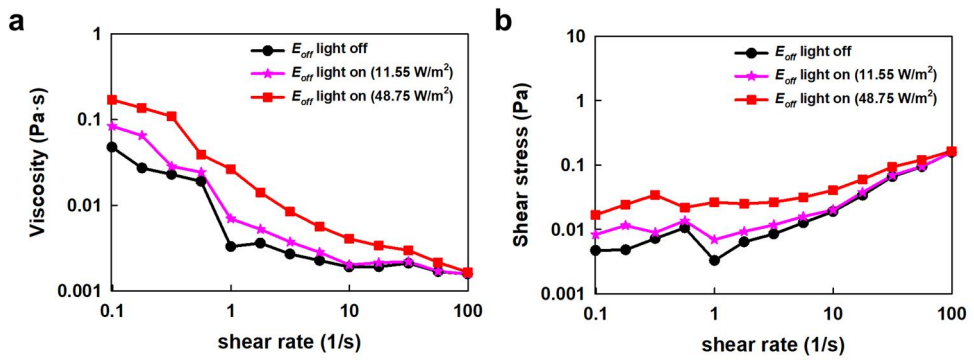


Figure 3.10 Rheological properties of the cell suspensions under different light conditions. (a) Viscosity and (b) shear stress as a function of shear rate.

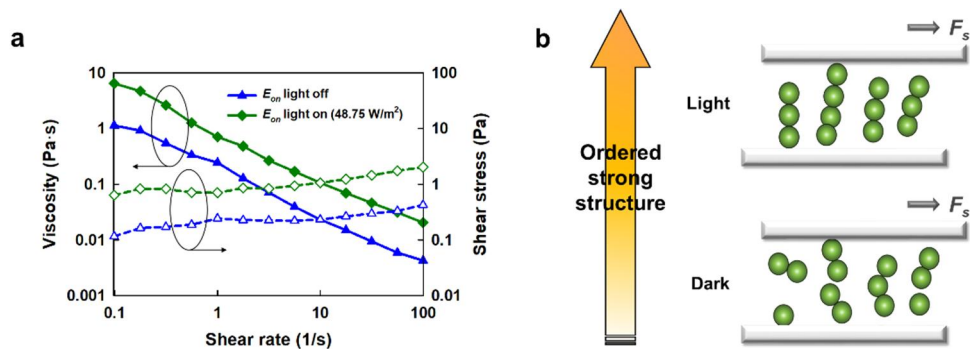


Figure 3.11 Rheological characterization of the cell suspensions. (a) Viscosity and shear stress under the electric field. (b) Schematic diagram of the spatial arrangement change of the cell suspension under the electric field.

3.4.4. Network formation of the photosynthetic bacterium suspension under the AC-electric field

To support these results, the network formation of *Synechocystis* under AC-electric field was observed by using a microscope (**Figure 3.12**). The spatial distribution of the cells was detected across the planar gold electrodes. Once the electric field was applied, the cells were rapidly assembled and aligned along the electric field. The cells tended to aggregate into network hexagonal configuration due to the interaction between near dipolar cell chains. The network structures were oriented over time in order to decrease the total electrical energy of the dispersion system (**Figure 3.13**) [11]. The numerical calculations elucidated the decrease in the total electrical energy induced by the formation of the network of *Synechocystis*. Three configurations of the cells under the electric field were considered: random packing, square packing, and hexagonal packing (**Figure 3.14**) [12].

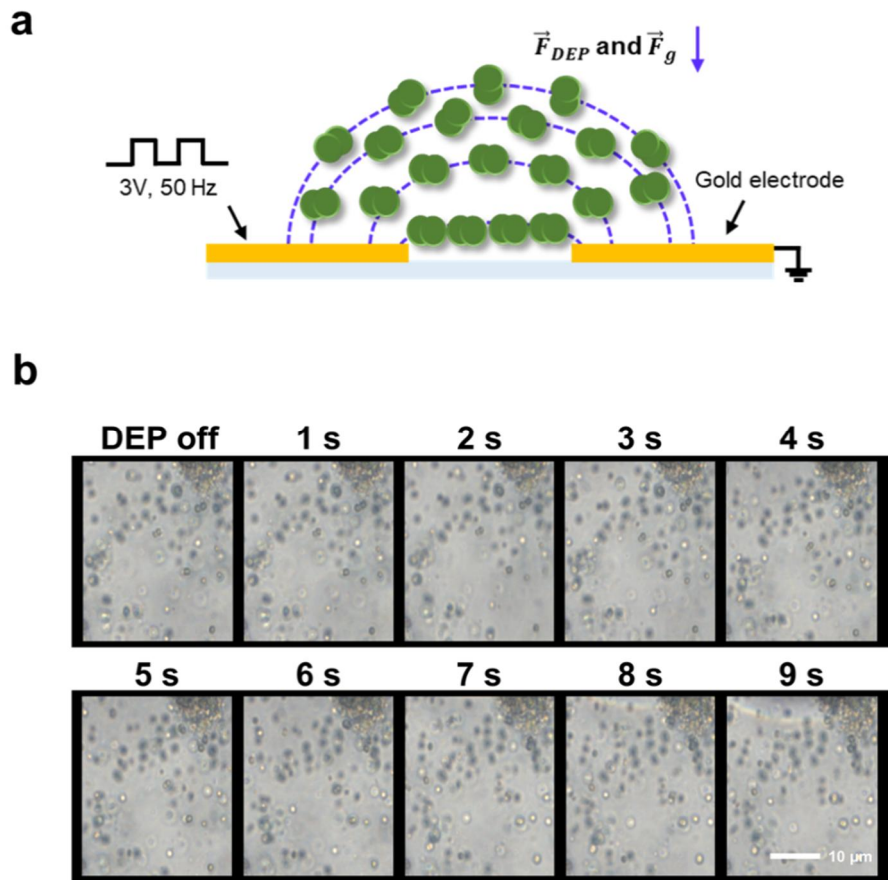


Figure 3.12 Self-assembly of cells under the AC-electric field. (a) Schematic diagram of the experimental setup. (b) Microscopic images of the cells.

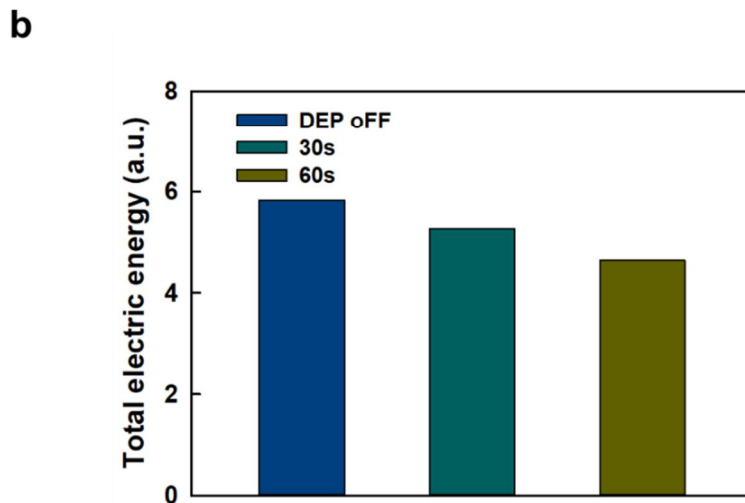
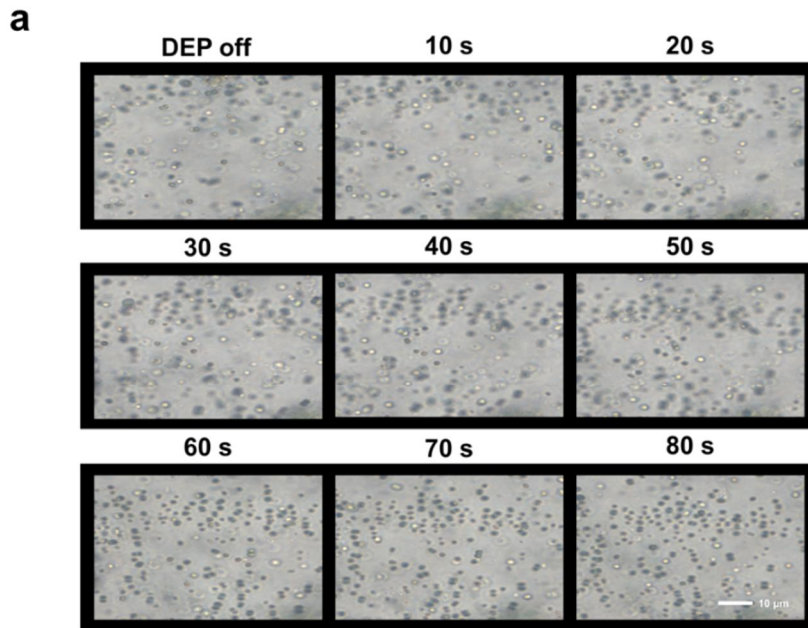


Figure 3.13 Self-alignment of *Synechocystis* under the electric field. (a) Microscopic images of the configurational changes of the cell for 80 s. (b) Total electric energy of the cells .

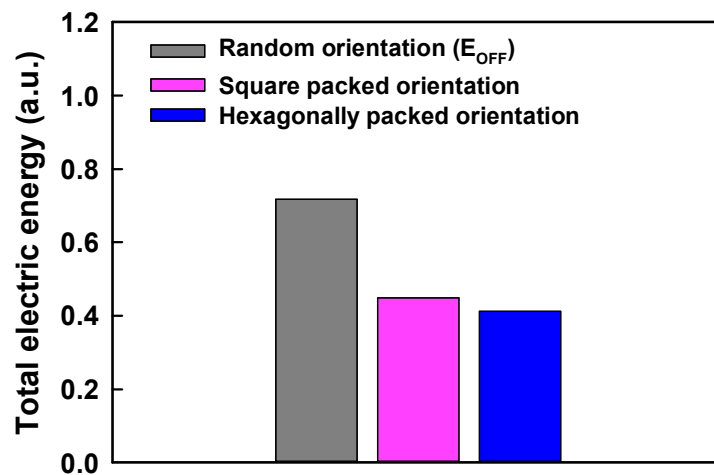


Figure 3.14 Total electric energy with respect to the cell orientation under AC-electric field. The decrease total electric energy is in accordance with the experimental results of cell assembly.

3.5. Conclusion

We have demonstrated the optorheology of the photosynthetic bacterium suspension. Since photosynthesis under the light causes changes of the electrophoretic properties of cells, the rheological properties are affected significantly. Under the electric field, the optorheological change was clearly identified. The light-induced electrons forms electric dipoles and affects the cell dispersion in the suspension. For further understanding of this phenomenon, numerical simulation was carried out using the finite element method. The rheological properties of the living cell suspension can be controlled by using light, which is a new finding for rheological applications.

3.6. Bibliography

- [1] I. Soga, A. Dhinojwala, S. Granick, *Langmuir*, 14 (1998) 1156-1161.
- [2] S. Odenbach, S. Thurm, Magnetoviscous effects in ferrofluids, in: *Ferrofluids*, Springer, 2002, pp. 185-201.
- [3] H.P. Gavin, R.D. Hanson, F.E. Filisko, *Journal of applied mechanics*, 63 (1996) 669-675.
- [4] A. Simmonds, in: *IEE Proceedings D-Control Theory and Applications*, IET, 1991, pp. 400-404.
- [5] H.R. Yun, D.J. Lee, J.R. Youn, Y.S. Song, *Nano energy*, 11 (2015) 171-178.
- [6] F. Wottawah, S. Schinking, B. Lincoln, S. Ebert, K. Müller, F. Sauer, K. Travis, J. Guck, *Acta biomaterialia*, 1 (2005) 263-271.
- [7] E. Eroglu, P.K. Eggers, M. Winslade, S.M. Smith, C.L. Raston, *Green Chemistry*, 15 (2013) 3155-3159.
- [8] M.v. Smoluchowski, *Zeitschrift für physikalische Chemie*, 92 (1918) 129-168.
- [9] H. Ohshima, *Journal of colloid and interface science*, 163 (1994) 474-483.
- [10] M. Planchon, T. Jittawuttipoka, C. Cassier-Chauvat, F. Guyot, F. Chauvat, O. Spalla, *Colloids and Surfaces B: Biointerfaces*, 110 (2013) 171-177.
- [11] S.O. Lumsdon, E.W. Kaler, O.D. Velev, *Langmuir*, 20 (2004) 2108-2116.
- [12] O.I. Bernal, B. Bharti, M.C. Flickinger, O.D. Velev, *Langmuir*, 33 (2017) 5304-5313.

Part II

Biorheological Energy Harvesting System

Chapter 4

Sustainable cyanobacterial flow battery using simultaneous light-dependent and -independent reactions by cellular metabolism

4.1. Introduction

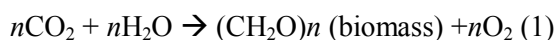
Solar energy is a practical alternative energy resource to fossil fuel yielding minimal environmental footprints. The conversion of light energy into chemical energy by photosynthesis is an essential process for life on Earth. Cyanobacterium, a photoautotroph, has the same electron transport chain as plants. They utilize carbon dioxide as a carbon source for cellular functions such as biosynthesis and respiration. Most of cyanobacteria generate electrons via water splitting in photosystem II complexes [1]. Electrons released from PSII complexes pass through the cytoplasmic membrane connected to the thylakoid membrane, and transport to the exterior through appendage [2].

Biological photovoltaics (BPV) are “living solar cells” that can generate current from the photosynthetic activity of photoautotrophs unlike the microbial fuel cell (MFC) harnessing heterotrophs which need the organic matter continuously [3, 4]. While common photovoltaics (PV) can generate electricity only during the light period, BPV are capable of producing electricity in both dark and light environments. In addition, BPVs are also able to heal light-induced damage of photosynthetic systems. In these respects, BPVs are called a viable system for environmentally-friendly energy generation.

Electrons formed from microorganism are transferred to anode and then moved through an external electric circuit to the cathode, thus producing electricity. The electron transfer takes place via either (1) direct contacts, such as bacteria themselves attached to an electrode or their pili and (2) indirect contacts such as external mediators known as electron shuttles [5-7]. Simultaneously, protons released from cells pass through proton exchange membrane to the cathode chamber, where they are combined with electrons and oxygen to produce water [8, 9]. For example, redox-mediators are employed to transport electrons from photoautotrophs to electrode [10-12]. In general, abiotic electron transfer mediators such as platinum, transition metals or potassium ferricyanide, $K_3[Fe(CN)_6]$, are used in the cathode [13]. Working as a terminal electron acceptor, the abiotic cathodes can transport electrons to oxygen. However, Pt has a limitation due to its cost and feasible toxicity in the substrate solution [9, 14]. Moreover, its catalytic activity decreases with increasing pH [15]. On the other hand, while ferricyanide with transitional iron increases the electron transfer, it needs to be supplied continuously [16, 17]. It has also been reported that ferricyanide reduces the cell viability due to its toxicity [18]. Some attempts have been made to transfer electrons by using biofilm in a batch state [19, 20]. For instance, Bombelli *et al.* [20] allowed cells to settle down onto the electrode during 12 hours, and Sekar *et al.* [21] harvested electrical energy by employing the method of attaching cells to electrodes.

Different from a batch mode, flow based continuous system for energy harvesting enables the separation of power generation and energy storage. One example is Vanadium redox flow battery (VRFB), which is a typical flow cell proposed by Skyllas-Kazacos, converts chemical energy into electrical energy [22]. It takes advantage of two separate electrolyte reservoirs filled with the electrolytes of V^{4+}/V^{5+} and V^{2+}/V^{3+} in sulfuric acid solution. In the VRFB system, the energy capacity is determined by only the size of the electrolyte tanks since it is decoupled with energy generation. Hence, it is receiving a lot of attention these days. However, VRFB requires the use of rare elements which are also corrosive or toxic. Meanwhile, recent studies have adopted photo-biocathode as a terminal electron

acceptor for the oxygen reduction reaction (ORR) in MFC [23-26]. For the device, carbon dioxide was regularly supplied to the cathode compartment by aeration [25, 26]. Under light, cells at the cathode chamber convert carbon dioxide and water into oxygen and biomass and harness electrons supplied from anode. In other words, due to the amplified photosynthetic rate, it acts as a final electron acceptor. The overall biochemical reaction is as follows:



In this reaction, carbon dioxide is a sole carbon source during the process. BPVs can be controlled by managing the amount of carbon dioxide only at the cathode chamber.

We demonstrate a cell-based flow battery, cyanobacterial flow battery (CFB) in this study. The sustainable BPV encompassing two electrolyte reservoirs employed bicarbonate ion to control the concentration of carbon dioxide in cyanobacteria suspension. To transfer electrons from the cyanobacteria (*Synechocystis* sp. PCC 6803) to the anode without using mediators, the path of the cells along the flow streamline and the resulting contact to the electrode were controlled and adopted. The fluid flow of the CFB was analyzed numerically, and the oxygen concentration was evaluated in the modeling.

4.2. Experimental

4.2.1. Bacterial culture conditions and characterization

A wild-type strain of *Synechocystis* sp. PCC 6803 (subsequently called *Synechocystis*) was obtained from Prof. Y.-I. Park's Laboratory at Chung-Nam National University, Daejeon, Korea. The cell was grown on 1% BG-11 agar plates buffered with 0.3% (w/v) sodium thiosulphate ($\text{Na}_2\text{S}_2\text{O}_3$) at 28 °C under a white LED light for 2 weeks. The cells were re-suspended in 1% BG 11 solution, and after one week the cell density was controlled to be 1.5×10^8 cells/ml.

The optical density was adjusted to 1.45 at 680 nm using a UV-Vis spectrometer (Perkin Elmer, USA). In order to check the salt stress of cyanobacteria, the optical density was measured at a light wavelength of 730 nm for cyanobacteria. [27] The morphology of the cells was characterized by using field emission scanning electron microscopy (FE-SEM; JSM-7600F, JEOL Ltd., Japan). Prior to observing the cells, the diluted cell solution was dropped onto a copper stub and coated with platinum for 100 seconds. The cell had a peanut-shaped appearance, and a length of about 2 μm with the type IV pili (**Figure 4.1**).

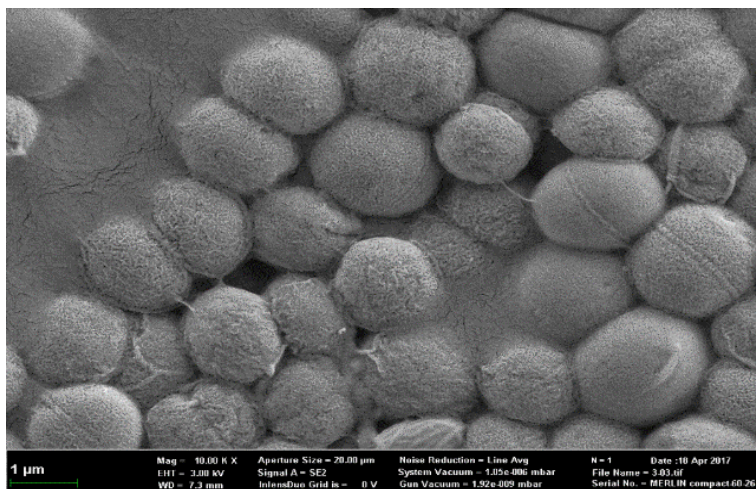


Figure 4.1 Scanning electron microscopy (SEM) of *Synechocystis* sp. PCC 6803 showing extracellular appendages. It is peanut-shaped particle composed of two-partially fused spherical lobes in shape. The scale bar denotes a length of 1 μm.

4.2.2. Solution preparation

Both the anode and the cathode compartments were filled with *Synechocystis* suspension. In order to remove oxygen in the cell solution of the anode compartment, the solution was purged with nitrogen at a gas pressure of 0.03 bar for 10 min. Sodium bicarbonate (NaHCO_3) was added into the cathode cell solution at different concentrations (0, 0.005, 0.01, 0.05, 0.1, 0.2, 0.25 and 0.5 M) as a main carbon source. The dissolved oxygen (DO) of the samples was measured with a DO meter (model PDO-520; UKAS, Taipei, Taiwan), and pH was measured with a pH meter (model AP 63; Fisher, Pittsburgh, PA, USA).

4.2.3. CFB fabrication and measurements

The CFB device was composed of three parts: a membrane (Nafion 117, Dupont USA), an anodic chamber, and a cathodic chamber. Platinum mesh (Ametek, TN, USA) was used as an electrode. The accessible surface of the electrode was ca. $1.95 \times 10^{-4} \text{ m}^2$. The size of the chamber was $1.2 \text{ mm} \times 1.2 \text{ mm} \times 2 \text{ mm}$, and a platinum mesh was placed in the middle of the each chamber. The membrane was fastened between anodic and the cathodic chambers, and fixed by using bolts. The device was connected to the external wires to complete the circuit. The cell suspensions in both external tanks were injected into each chamber through a flexible tube (Tygon E-3603, ACF00001, Saint Gobain, Tokyo, Japan) connected to the sidewall of the chamber. Flow rate was controlled by using a pump.

In order to characterize the photoelectrochemical behavior of the device, the performance was evaluated using a potentiostat (VersaSTAT 3, Princeton Applied Research; Oak Ridge, TN, USA). Under dark and light conditions, polarization curves were acquired by recording the current, I with various load resistances (371, 1.3 k, 3.25 k, 10.7 k, 20.3 k, 35.4 k, 55 k, 121.7 k, 162.5 k, 245.8 k, 0.506 M and 1.016 M Ω). The voltage, V was derived from Ohm's law $V=R_{ext} \cdot I$, and the delivered power, P was given by $P=I^2 R_{ext}$.

To stimulate the photosynthesis reaction of the cells, a halogen lamp (KLS 150H-RC-150E, Kwangwoo, Korea) was used as an artificial light source. The intensity of the light source was measured by using an integrating sphere (Labsphere Co., North Sutton, NH, USA) with a 6-inch diameter monochromator (Acton Research Co., Acton, MA) attached to a photomultiplier tube (Hamamatsu Photonics K.K., Japan). The spectrum of the light source showed strong intensity near the absorption peaks of the microalgae and the full spectrum of visible light (**Figure 4.2**).

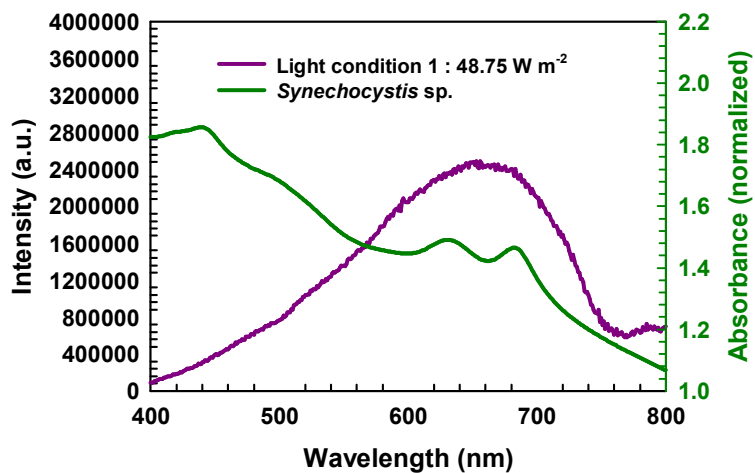


Figure 4.2 Absorption spectrum of *Synechocystis* sp. PCC 6803 and irradiance spectrum of the halogen lamp used in this study. The light source provided a full spectrum of visible light for natural photosynthesis of *Synechocystis* sp. PCC 6803.

4.3. Numerical analysis

Generally, the electrochemical reaction at the cathode is *ca.* 1000 times slower than that at the anode. In other words, the cathode reaction is the so-called rate-determining step (RDS), and the resulting current is generated depending on the oxygen consumption at the cathode. The oxygen concentration in the device was modeled, taking into account the reaction occurring at the cathode. In order to assess the mass transfer of oxygen, the following assumptions were applied: (1) the oxygen produced by cyanobacteria was dissolved in the solution completely; (2) it was consumed on the electrode; and (3) temperature was kept at room temperature (25°C). The governing equation was expressed as the following:

$$\frac{\partial c_i}{\partial t} + \nabla \cdot \mathbf{N}_i = R_i \quad (4)$$

$$\mathbf{N}_i = -D_i \nabla c_i + c_i \mathbf{u} \quad (5)$$

where c_i is the concentration of the oxygen, D_i is the diffusion coefficient of the oxygen (i.e., 1.6×10^{-5} cm²/s), \mathbf{u} is the velocity, and R_i is the reaction rate. It was assumed that the initial concentration of the oxygen at the electrode was zero. The initial concentration of the oxygen at the chamber was set to be 84.856 mol/m³, which was obtained by the experiments (**Figure 4.3**). The oxygen consumption rate was determined by using the ratio of the current at 100 s in the amperometric results. Since the irradiation of light for each cycle was performed for 300 s experimentally, the concentration distribution on the electrode surface was calculated for the same time period.

A numerical scheme was implemented to solve the Stokes equation by using a commercial package, COMSOL Multiphysics 5.3a. The fluid was assumed to be incompressible. The inertia and gravity terms were neglected in the calculation. The corresponding governing equations are

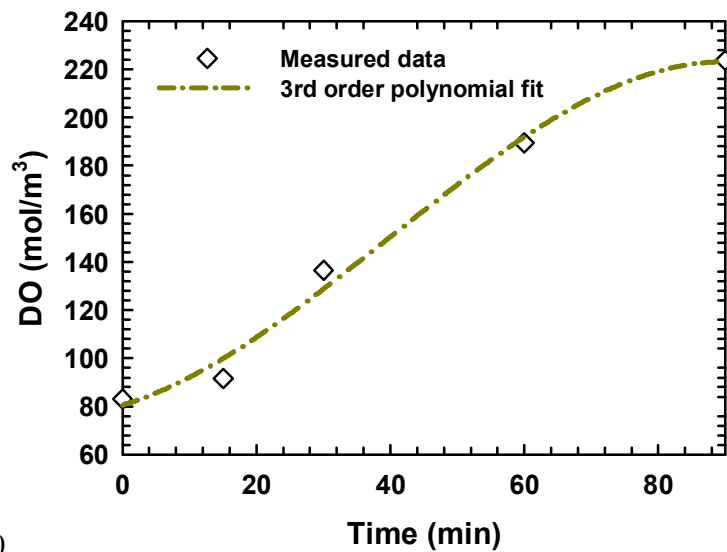
$$0 = \nabla \cdot \left[-p\mathbf{I} + \mu(\nabla \mathbf{u} + (\nabla \mathbf{u})^T) \right] \quad (6)$$

$$\nabla \cdot \mathbf{u} = 0 \quad (7)$$

where p is the pressure, \mathbf{u} is the velocity, and μ is the viscosity of the liquid. Here, the Carreau model was used to model the behavior of non-Newtonian fluid (**Figure 4.4**).

$$\mu = \mu_{\infty} + (\mu_{\infty} + \mu_0)(1 + (\lambda + \dot{\gamma})^a)^{\frac{n-1}{a}} \quad (8)$$

where μ_{∞} is the infinite shear viscosity, μ_0 is the zero shear viscosity, λ is a time constant, $\dot{\gamma}$ is a shear rate, and n is the exponent. The parameters of the Carreau model (**Table 4.1**) were obtained experimentally.



0

Figure 4.3 Dissolved oxygen (DO) variation of *Synechocystis* sp. PCC 6803 with 0.05 M NaHCO₃ during light condition. A polynomial fit with a cubic equation fits to all the data.

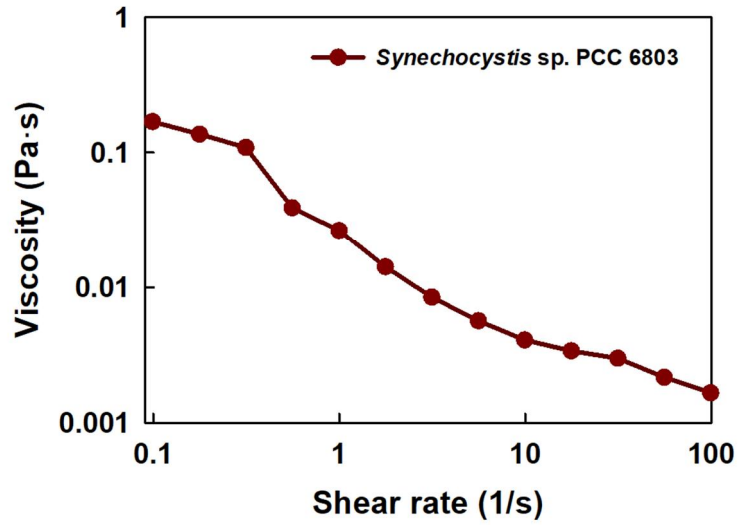


Figure 4.4 Rheological measurements of cell solution under the light. (a) Viscosity in the range of shear rate from 0.1 to 100 s⁻¹. The measured viscosity data were fitted to the Carreau model.

Table 4.1 Parameter list for the Carreau model obtained from the chapter 3.

| Constant name | Symbol | Value | unit |
|--------------------------|--------------|------------------------|------|
| Zero shear viscosity | μ_0 | 0.2172 | Pa·s |
| Infinite shear viscosity | μ_∞ | 2.210×10^{-3} | Pa·s |
| Time constant | λ | 6.358 | s |
| Power law exponent | n | 1.174 | - |

4.4. Results and discussion

4.4.1. Design and construction of CFB

A structural scheme of the sustainable CFB is shown in **Figure 4.4**. The CFB utilizes only cyanobacteria in order to generate electricity via microbial photosynthesis. Both anodic and cathodic half-cells were embedded by *Synechocystis* and the proton exchange membrane (PEM) was placed between the half cells. Illumination was applied from a location approximately 4 cm away from the side of the device. Since *Synechocystis* is capable of extracellular electron transport through direct electron transfer *via* conductive nanowire, the mediator-free electron generation system was employed in this study for a sustainable energy harvesting. Initially, we inoculated cell solution into the chamber from bottom to top by using a pump. The cell suspension flowed at different flow rates, $Q = 0, 0.03, 0.05, 0.1, \text{ and } 0.3 \text{ ml / min}$.

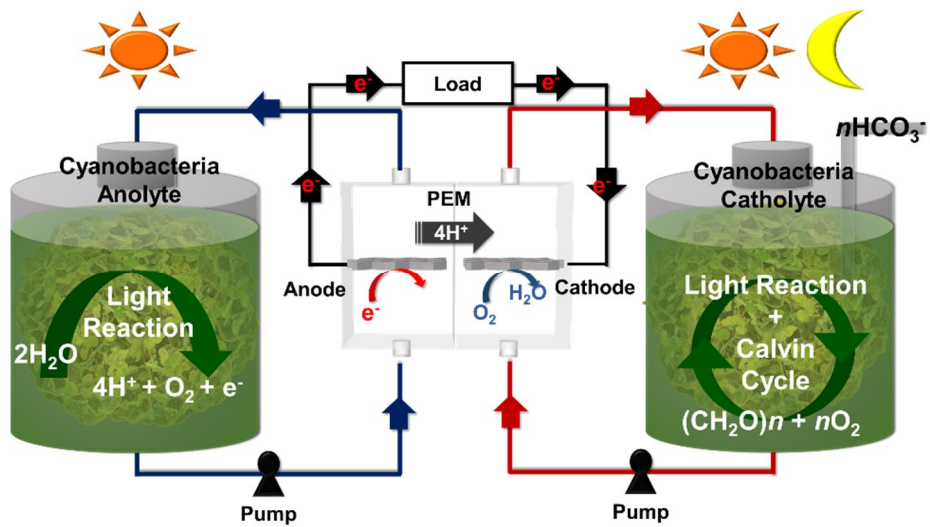


Figure 4.4 Schematic illustration of the CFB introduced in this study. The cyanobacteria embedded energy electrolytes are circulated through the flow system.

4.4.2. Oxygen production at different bicarbonate concentrations

As previously mentioned, photosynthetic organism performs photosynthesis by employing CO_2 as a carbon source and then producing oxygen under light. In general, CO_2 is not dissolved in water readily. In the current study, bicarbonate ion (HCO_3^-) was selected as a carbon source, which has a high dissolution level in water [28]. In addition, bicarbonate ion is absorbed more efficiently to photoautotrophs than CO_2 [29]. Moreover, harnessing HCO_3^- allows us to maintain the pH range of medium from 6.4 to 10.3 [30]. Recently, it was revealed that energy metabolism was affected by HCO_3^- , e.g., the growth of photoautotrophs was enhanced at a certain concentration [31]. To determine the optimal cell condition, we adopted different concentrations of NaHCO_3^- from 0 to 0.5 M and investigated the drift of the dissolved oxygen (DO) and pH variation over time.

Figure 4.5 showed that the DO values increased in all the conditions compared to the initial value. It implies that the presence of NaHCO_3 enhances metabolic activity. However, the DO values did not present a linear proportionality to NaHCO_3 concentration. For instance, the culture with 0.5 M NaHCO_3^- resulted in lower DO value than the others. This is because at a concentration above 0.25 M, cells were significantly affected by osmotic pressure. That is, the highly concentrated chemical inhibits cells from producing oxygen since *Synechocystis* is a fresh water strain [32]. We checked the OD (730 nm) value of the cell solution for 7 days after adding NaHCO_3 to verify the effect of NaHCO_3 (**Figure 4.6**). It was found that the culture with 0.05 M NaHCO_3 had a maximum value of OD, indicating a maximum growth rate of cells. On the contrary, the culture with 0.2 M NaHCO_3 or higher concentration showed relatively low OD values. Moreover, both the OD and pH showed similar trend (**Figure 4.5**). Since a pH value of 8.5 led to the highest specific growth rate [33], the culture with 0.05 M NaHCO_3 was used as a cathodic solution. Before the electrochemical test, light was irradiated for 5 min.

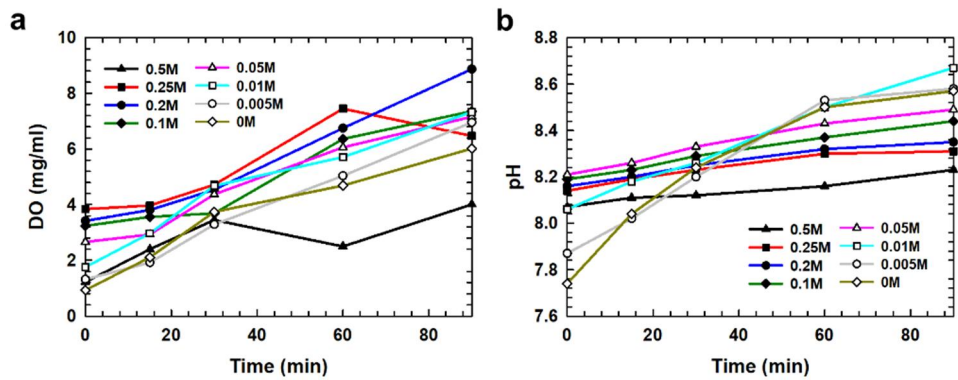


Figure 4.5 Characterization of the culture with different concentrations of sodium bicarbonate (NaHCO₃). (a) Dissolved oxygen (DO) and (b) pH of the cell suspension with respect to time.

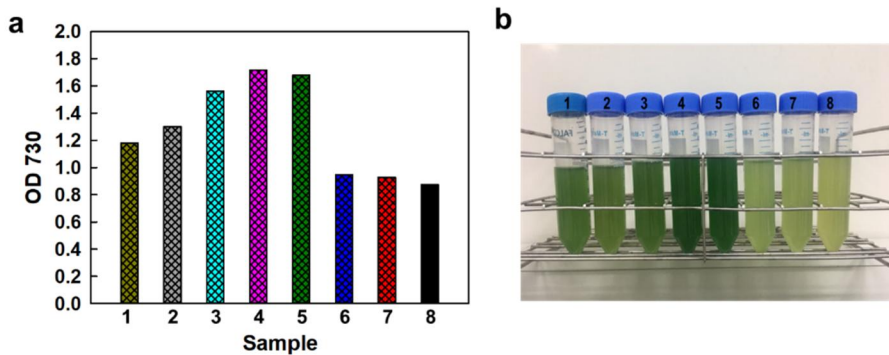


Figure 4.6 Growth of *Synechocystis* sp. PCC 6803 with different concentrations of NaHCO_3 as a carbon source. The data were measured 7 days after supplying NaHCO_3 . (a) Optical density of samples. (b) Real image of samples. (Sample 1: 0 M NaHCO_3 , Sample 2: 0.005 M NaHCO_3 , Sample 3: 0.01 M NaHCO_3 , Sample 4: 0.05 M NaHCO_3 , Sample 5: 0.1 M NaHCO_3 , Sample 6: 0.2 M NaHCO_3 , Sample 7: 0.25 M NaHCO_3 , and Sample 8: 0.5 M NaHCO_3)

4.4.3. Current and power analyses in the batch mode

To validate the concept of this study, we first tested the device in the batch mode. For photo-electrochemical activity measurements, the device was irradiated for 100 s and then in a light/dark cyclic manner per 300 s. The effect of the light/dark period was apparently identified from the amperometric measurements. As shown in Fig. 3a, the cyanobacteria produced electricity as soon as they were exposed to light. An average total current of 177 nA was measured, and the peak power density was $7.6 \mu\text{W}/\text{m}^2$ at $55 \text{ k } \Omega$, where $V \approx 8.97 \text{ mV}$ and $I \approx 838.12 \mu\text{A}/\text{m}^2$ (**Figure 4.7**). As observed in **Figure 4.7**, it was proven that a bioelectrochemical cell consisting of only photosynthetic organisms could be implemented by using HCO_3^- .

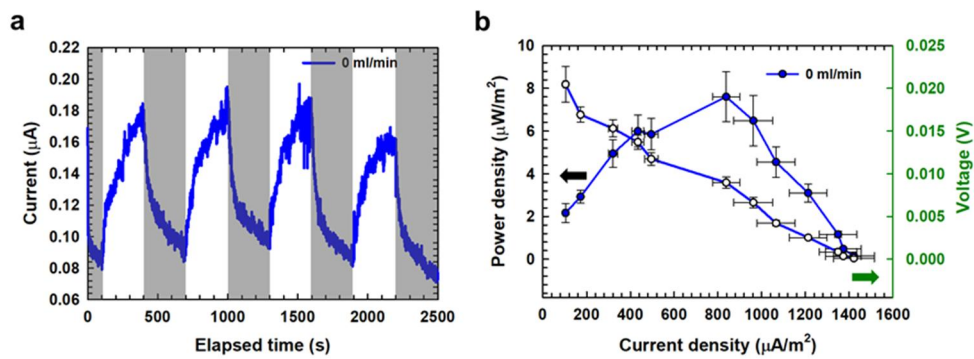


Figure 4.7 Photoelectrochemical behavior of the BPV in the batch mode. (a) Cyclic photo-response measured with respect to time. The light irradiation was imposed after 100 s, and the measurement was made for every 300s light/dark interval. (b) Power density and polarization results of the cell under light.

4.4.4. Effect of flow rate in CFB

We explored the performance of the CFB with respect to the flow rates. In the continuous flow mode, the power generation and energy storage of cell can be separated. The energy capacity is dependent upon the volume of each flow chamber, and the energy efficiency can be maximized by controlling the flow rate. When changing the flow rate as 0.03, 0.05, 0.1, and 0.3 ml / min, the resulting electricity generation is displayed in **Figure 4.8**. In the range of $Q \leq 0.05$ ml / min, the total current increases with increasing the flow rate. It was found that $Q = 0.05$ ml / min was the optimal flow rate to generate the electricity. Compared with the results of the batch mode, the dark and photo response currents were increased by 2.6 and 2 folds, respectively. This phenomenon was caused by combination of two effects: (1) the shear stress acts as a stimulus to cyanobacteria [6], and (2) more cells are supplied to the electrode per unit time, i.e., the enhancement in mass transfer. However, at a flow rate of 0.1 ml / min the amplitude of the photo response and dark currents decreased. In particular, at the flow rate of 0.3 ml / min the photo response and average dark currents were *ca.* 72 and 44 nA, respectively, which were about 48 % and 22 % lower than the results of the batch case. The shear rate ($\dot{\gamma}$) higher than 10^{-2} s^{-1} could have adverse influence on the metabolic activity of the cells. That is, as the flow rate increased from 0 to 0.05 ml / min, the current generation increased due to the synergistic effect of mass transfer and cell stimulation. However, the excessive flow rate acted as a negative cell stimulus, thus reducing the current.

The power and polarization of the cell were analyzed to evaluate the performance of the CFB (**Figure 4.9**). Both curves were prepared by using various external resistances under pseudo-steady state conditions [34]. The power output curve showed a quite similar trend to the chronoamperometric response of a biophotovoltaic device. The continuous operation mode had found to have the enhanced power output compared with the batch mode. The outstanding power output was observed at a flow rate of 0.05 ml / min (i.e., a peak power density of

36.27 $\mu\text{W}/\text{m}^2$), which was 4.8 fold improvement.

A noticeable difference in the power output can arise from the frictional loss, which increases with respect to flow rate. Unlike the batch mode, the fluid flow induced the energy dissipation due to the hydrodynamic resistance [9, 35]. The pressure drop induced by the energy dissipation, Δp can be estimated using the Darcy-Weisbach equation.

$$\Delta p = L \times \frac{f_D}{D_H} \times \frac{\rho \times v^2}{2} \quad (9)$$

where L is the channel length, f_D is the Darcy friction factor, D_H is the hydraulic diameter, ρ is the density of fluid, and v is the mean flow velocity. In particular, the frictional loss occurring at a flow rate of 0.3 ml / min was 6-fold higher than the maximum power output (**Figure 4.10**). As the flow rate increases, the net power can be reduced due to the frictional loss as well as the negative stimulus to the cells. In addition, the maximal power generation was observed when the external load was equal to the internal resistance of the cell. The maximum power output of all the cases was measured at 121.7 k Ω .

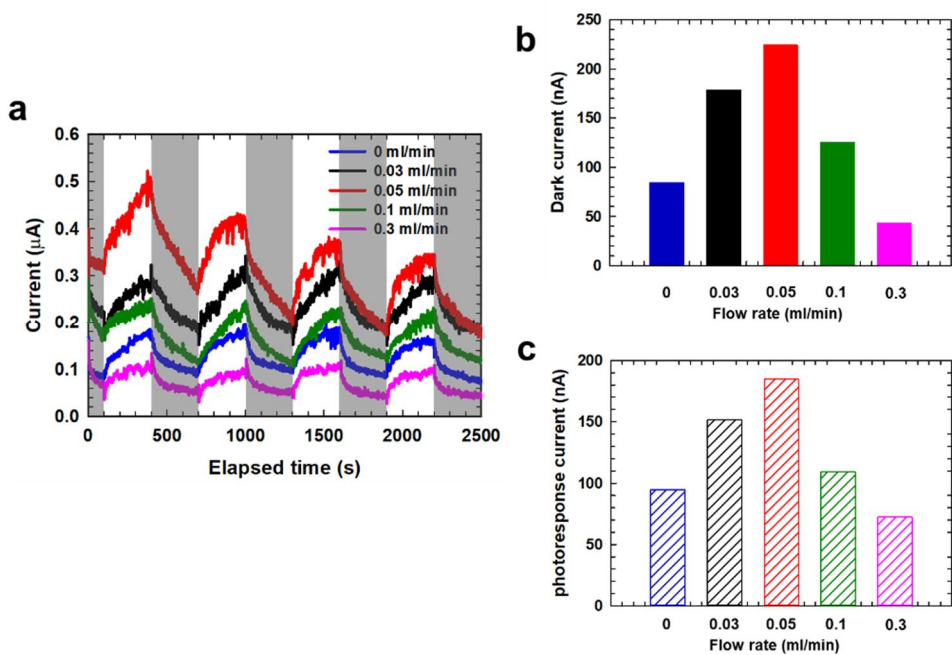


Figure 4.8 Photoelectrochemical behavior of the CFB. (a) Cyclic photo-response of the cell measured using a 510Ω resistance. The light was irradiated after 100 s, and the measurement was made for every 300s light/dark interval. (b) Dark current result and (c) photoresponse current of the cell with respect to the flow rate.

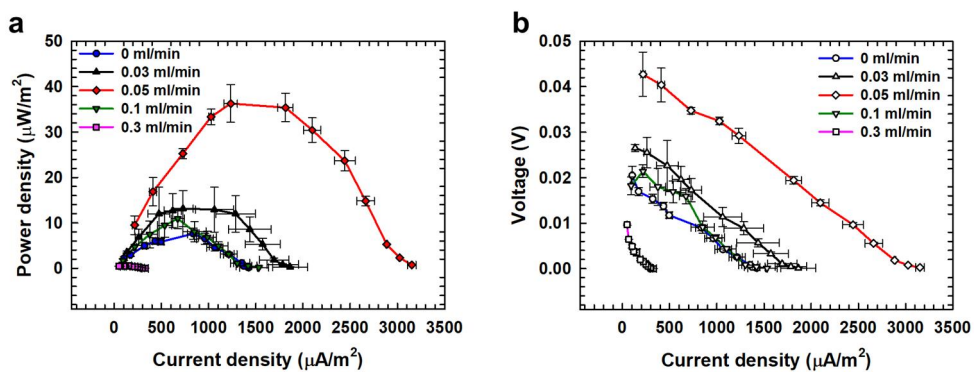


Figure 4.9 Photo-electrochemical performance of the CFB. (a) Power density and (b) polarization results with respect to the flow rate.

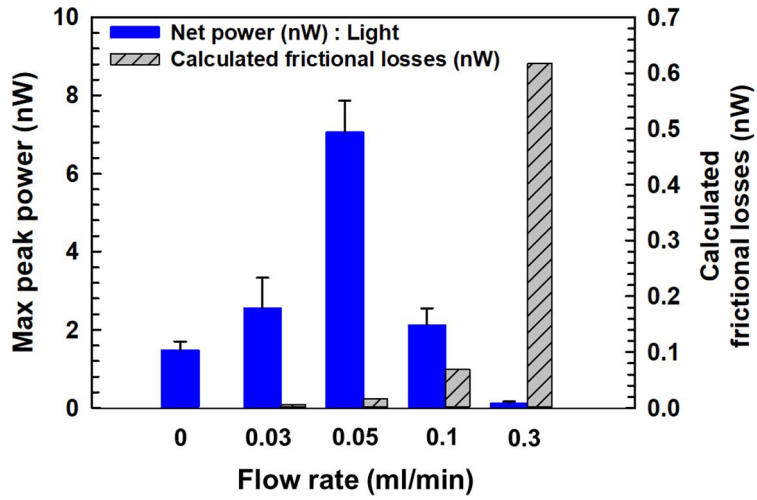


Figure 4.10 Effect of the flow rate on the CFB. The max peak power changes according to the flow rate, and the frictional loss was calculated analytically.

4.4.5. Numerical analysis of the mass transfer effect

Numerical simulation was conducted to understand the mass transfer effect on the cell performance. Since the cell solution has non-Newtonian fluid properties, the viscosity should be considered as a function of the flow rate unlike other aqueous-flow battery studies [36]. In this study the Carreau model was assumed for viscosity of the cell solution (**Figure 4.4**).

Figure 4.11 demonstrates the velocity distribution and the concentration distribution in the device. As the flow rate increased, the mass transfer to the electrode increased (**Figure 4.11a**). Since the current production is proportional to the oxygen consumption in the electrode, the current generation can be modeled by using the oxygen concentration at the electrode. **Figure 4.11b** shows the concentration distribution at 300 seconds after light irradiation. As a result, the trend of oxygen concentration in the electrode was similar to the experimental results. In addition, the concentration changes from 0 to 300 s at each flow rate are shown in **Figure 4.12**.

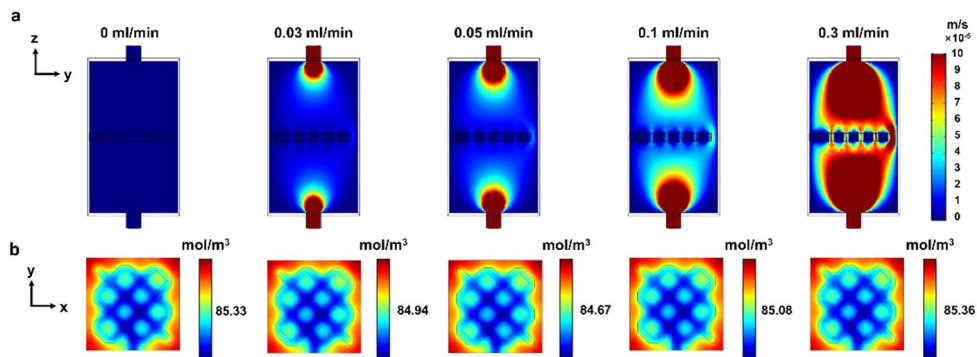


Figure 4.11 Results of numerical analysis for the CFB. (a) Velocity profiles in the cathodic chamber according to the flow rate. (b) Distribution of oxygen concentration on the cathode depending on the flow rate.

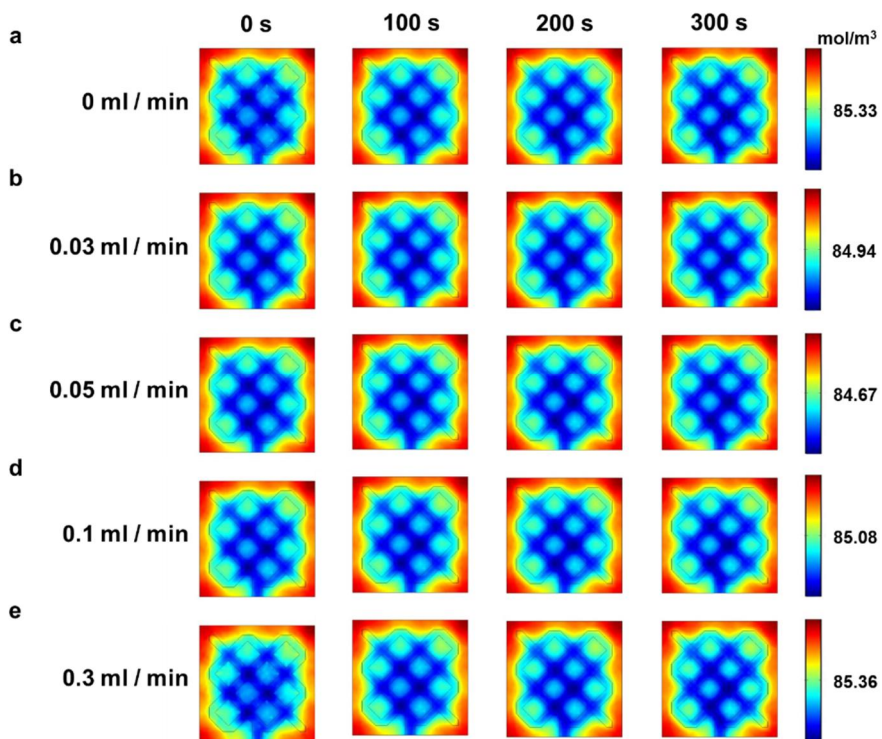


Figure 4.12 Simulation of oxygen concentration profiles of the electrode surface at 0 ml /min (a), 0.03 ml /min (b), 0.05 ml /min (c), 0.1 ml /min (d), and 0 ml /min (e). The results are the concentration profiles of 0 s, 100 s, 200 s, 300 s, and 400 s after light on.

4.5. Conclusion

We have demonstrated a novel CFB containing *Synechocystis* sp. PCC 6803, where bicarbonate ion was employed as an enhancer for photosynthesis. In the batch mode, the device yielded a peak power density of $7.6 \mu\text{W}/\text{m}^2$ without using external mediators. 0.05 M NaHCO_3 was added into the cell culture for the photosynthetic activity of the cyanobacteria. When the device was operated under the optimal flow condition, the peak power density was increased by 4.8 times compared with that of the batch mode. It was shown that the fluid flow in the CFB acted as a stimulus to the cell as well as a material transferring carrier in the device. Numerical simulation of the mass transfer in the CFB was conducted to analyze the effect of the flow rate and on the performance of the cell. The concept of this study can be applied to all kinds of microorganisms based energy systems using carbon sources and light for photosynthesis.

4.6. Bibliography

- [1] J.P. Zehr, S.R. Bench, B.J. Carter, I. Hewson, F. Niazi, T. Shi, H.J. Tripp, J.P. Affourtit, *science*, 322 (2008) 1110-1112.
- [2] D.J. Lea-Smith, P. Bombelli, R. Vasudevan, C.J. Howe, *Biochimica et Biophysica Acta (BBA)-Bioenergetics*, 1857 (2016) 247-255.
- [3] A.J. McCormick, P. Bombelli, R.W. Bradley, R. Thorne, T. Wenzel, C.J. Howe, *Energy & Environmental Science*, 8 (2015) 1092-1109.
- [4] R.A. Soni, K. Sudhakar, R. Rana, *International Journal of Environment and Sustainable Development*, 15 (2016) 313-325.
- [5] C.I. Torres, A.K. Marcus, H.-S. Lee, P. Parameswaran, R. Krajmalnik-Brown, B.E. Rittmann, *FEMS microbiology reviews*, 34 (2010) 3-17.
- [6] D. Vigolo, T.T. Al-Housseiny, Y. Shen, F.O. Akinlawon, S.T. Al-Housseiny, R.K. Hobson, A. Sahu, K.I. Bedkowski, T.J. DiChristina, H.A. Stone, *Physical Chemistry Chemical Physics*, 16 (2014) 12535-12543.
- [7] B. Korth, L.F. Rosa, F. Harnisch, C. Picioreanu, *Bioelectrochemistry*, 106 (2015) 194-206.
- [8] R.W. Bradley, P. Bombelli, S.J. Rowden, C.J. Howe, in, Portland Press Limited, 2012.
- [9] K.L. Saar, P. Bombelli, D.J. Lea-Smith, T. Call, E.-M. Aro, T. Müller, C.J. Howe, T.P. Knowles, *Nature Energy*, 3 (2018) 75.
- [10] T. Yagishita, T. Horigome, K. Tanaka, *Journal of Chemical Technology & Biotechnology*, 56 (1993) 393-399.
- [11] M. Torimura, A. Miki, A. Wadano, K. Kano, T. Ikeda, *Journal of Electroanalytical Chemistry*, 496 (2001) 21-28.
- [12] Y. Zou, J. Pisciotta, R.B. Billmyre, I.V. Baskakov, *Biotechnology and Bioengineering*, 104 (2009) 939-946.
- [13] Z. He, L.T. Angenent, *Electroanalysis: An International Journal Devoted to Fundamental and Practical Aspects of Electroanalysis*, 18 (2006) 2009-2015.
- [14] A.J. Bard, L.R. Faulkner, *Electrochemical Methods*, 2 (2001) 482.
- [15] F. Zhao, F. Harnisch, U. Schröder, F. Scholz, P. Bogdanoff, I. Herrmann, *Environmental science & technology*, 40 (2006) 5193-5199.
- [16] J.K. Jang, I.S. Chang, B.H. Kim, *Journal of Microbiology and Biotechnology*, 14 (2004) 324-329.
- [17] S. Oh, B. Min, B.E. Logan, *Environmental science & technology*, 38 (2004) 4900-4904.
- [18] C. Liu, T. Sun, Y. Zhai, S. Dong, *Talanta*, 78 (2009) 613-617.
- [19] P. Bombelli, M. Zarrouati, R.J. Thorne, K. Schneider, S.J. Rowden, A. Ali, K. Yunus, P.J. Cameron, A.C. Fisher, D.I. Wilson, *Physical Chemistry Chemical Physics*, 14 (2012) 12221-12229.
- [20] P. Bombelli, T. Müller, T.W. Herling, C.J. Howe, T.P. Knowles, *Advanced energy materials*, 5 (2015) 1401299.
- [21] N. Sekar, Y. Umasankar, R.P. Ramasamy, *Physical Chemistry Chemical Physics*, 16 (2014) 7862-7871.

- [22] E. Sum, M. Skyllas-Kazacos, *Journal of Power sources*, 15 (1985) 179-190.
- [23] E.E. Powell, M.L. Mapiour, R.W. Evitts, G.A. Hill, *Bioresource technology*, 100 (2009) 269-274.
- [24] E. Powell, R. Evitts, G. Hill, J. Bolster, *Energy Sources, Part A: Recovery, Utilization, and Environmental Effects*, 33 (2011) 440-448.
- [25] A.G. del Campo, P. Cañizares, M.A. Rodrigo, F.J. Fernández, J. Lobato, *Journal of Power Sources*, 242 (2013) 638-645.
- [26] J. Lobato, A.G. del Campo, F.J. Fernández, P. Cañizares, M.A. Rodrigo, *Applied energy*, 110 (2013) 220-226.
- [27] X. Miao, Q. Wu, G. Wu, N. Zhao, *FEMS microbiology letters*, 218 (2003) 71-77.
- [28] P.-H. Chen, H.-L. Liu, Y.-J. Chen, Y.-H. Cheng, W.-L. Lin, C.-H. Yeh, C.-H. Chang, *Energy & Environmental Science*, 5 (2012) 8318-8327.
- [29] K. Kumar, C.N. Dasgupta, B. Nayak, P. Lindblad, D. Das, *Bioresource technology*, 102 (2011) 4945-4953.
- [30] J.V. Moroney, R.A. Ynalvez, *Eukaryotic cell*, 6 (2007) 1251-1259.
- [31] Y. Zhao, Y. Hou, Z. Liu, S. Chen, F. Chen, *J Proteomics Bioinform*, 9 (2016) 137-143.
- [32] Z. Chi, F. Elloy, Y. Xie, Y. Hu, S. Chen, *Applied biochemistry and biotechnology*, 172 (2014) 447-457.
- [33] B.T. Nguyen, B.E. Rittmann, *Algal Research*, 19 (2016) 363-369.
- [34] B.E. Logan, B. Hamelers, R. Rozendal, U. Schröder, J. Keller, S. Freguia, P. Aelterman, W. Verstraete, K. Rabaey, *Environmental science & technology*, 40 (2006) 5181-5192.
- [35] N.A. Mortensen, F. Okkels, H. Bruus, *Physical Review E*, 71 (2005) 057301.
- [36] W. Wang, Q. Luo, B. Li, X. Wei, L. Li, Z. Yang, *Advanced Functional Materials*, 23 (2013) 970-986.

Chapter 5

Anomalous power enhancement of biophotovoltaic cell

5.1. Introduction

Cyanobacteria are commonly used for producing biomass and chemicals [1]. In recent years, interesting attempts have been made to apply biomimetic strategies to energy harvesting and photofuels of synthetic materials such as ethanol, H₂, etc., based on the cyanobacteria (or plant) process. For instance, bio-electrochemical systems, such as bio-photovoltaic cells (BPV) [2] and microbial fuel cells (MFC), [3-5] have been explored to convert chemical energy to electricity by utilizing photosynthetic organism and heterotrophic bacteria. In one type of BPV, a microbial solar cell generates power from solar energy using only water as an electron source, while MFCs utilize the chemical energy stored in organic matter. For a microbial solar cell, a water splitting reaction occurs during light illumination, followed by the respiratory activities of photosynthetic microbes [6, 7]. In this sense, microbial solar cell is able to harness power from both light dependent reaction (i.e., photophosphorylation) and light independent reaction (i.e., Calvin cycle). A microbial solar cell has particular advantages over MFC for the following reasons: (1) microbial solar cell can directly harness the photosynthesis that has a high quantum efficiency. (2) microbial solar cell utilizes photosynthetic electrons without a mediator. (3) microbial solar cell can be used in aerobic conditions. In addition, microbial solar cell generates power from solar energy using only water as an

electron source, while MFC utilize the chemical energy stored in organic matter. (4) Since the photosynthetic inoculum is quite abundant, the cost of producing a micro solar cell can be low. Therefore, microbial solar cell possess inherently greater potential as an energy source than MFC. However, the power output efficiency of the cells remains near 0.1% [6], which is a big issue to be resolved for the robust and sustainable development of microbial solar cell.

To increase the efficiency of solar energy conversion, it is essential to extract the photosynthetic electrons generated inside the cell to the outside. Bioelectrochemical systems generally employ three different mechanisms of transporting electrons from cell to solid electron acceptors: [8, 9] (1) direct electron transfer using outer-membrane cytochromes coming in contact with a solid electron acceptor; (2) indirect transfer via a soluble electron mediator, and (3) indirect electron transfer via solid components including a biofilm matrix and cellular conductive pili (nanowire). Among these methods, the highest energy efficiency is achieved by extracting the photosynthetic electrons directly. Previous works have shown several new methods of direct extraction of electrons. It was revealed that the biofilm matrix enhanced power output due to its low electrochemical potential losses [4]. Bombelli *et al.* [10] recently showed high power output above 100 mW/m² by using a platform that allows cells to settle down on the anode, without requiring a membrane or mediator. Although this method has a high power output, it takes a long time (24 h) for the cells to settle on the anode after injection. In addition, Kim *et al.* [11] reported the feasibility of generating electricity by directly extracting electrons from photosynthetic electron transport without a mediator. However, since this method utilizes cell individually, it has difficulties in mass production of energy. Ham *et al.* [12] reported self-assembled light-harvesting complexes capable of mimicking the photosynthesis organelle. This method is a bottom up production method, but it has limitation in scale-up. Therefore, some researchers [13, 14] have demonstrated a CNT-biological hybrid system that facilitated the direct extraction of photosynthetic electrons and improved the electron transfer rates. Since these inorganic materials

only promote the transfer of photosynthetic electrons, improvement of cell efficiency is limited.

In this study, we demonstrated a novel bioinorganic hybrid system consisting of *Synechococcus* sp., iron oxide nanoparticles (IONPs) (γ -Fe₂O₃ and Fe₃O₄) and NdFeB (Ni-Ni_xO_y). In the system, nanomaterials can convert light into electricity and transfer the photosynthetic electrons from the photosynthetic cells to external electrode. That is, bioinorganic hybrid system provides synergistic combination of a natural photocatalyst and an artificial photocatalyst that leads to a high performance by forming effective electron transfer conduits to the electrode in a very short time. While most of the biophotovoltaics need quite a long time allowing cells to settle on the anode for mediator-free operation, we can effectively control the position of cells in a short time by using this proposed configuration. We achieved anomalous enhancement in the energy conversion efficiency by using the bioinorganic hybrid system.

5.2. Experimental

5.2.1. Bacterial culture conditions

Synechococcus sp. was obtained from the Korean Collection for Type Cultures (Korea), and cultured in BG11 medium (C3061, Sigma Aldrich) for 28 days before usage. The optical density at 680 nm of the cell concentration was adjusted to 0.84 (5×10^7 cells/ml). *Synechococcus* sp. is well known as a sheathless coccoid cyanobacterium (**Figure 5.1a**). The cell has a rod-shaped appearance, and its size varies from 1 μm to 2 μm .

5.2.2. Characterization of iron oxide nanoparticles

In the current study, we employed two kinds of spinel oxide nanoparticles, maghemite ($\gamma\text{-Fe}_2\text{O}_3$, 544884, Sigma Aldrich) and magnetite (Fe_3O_4 , 637106, Sigma Aldrich), with different ferrimagnetism properties. X-ray diffraction measurements confirmed that the IONPs were composed of single phase $\gamma\text{-Fe}_2\text{O}_3$ and Fe_3O_4 (Fig. S3). SEM observations showed that the size of the IONPs was smaller than 100 nm in diameter. Both materials are known to be more easily photocorroded than $\alpha\text{-Fe}_2\text{O}_3$. Therefore, they have been used more commonly in the field of recording and drug delivery than in the water splitting process. On the other hand, it has been reported that $\alpha\text{-Fe}_2\text{O}_3$ offers significantly higher toxicity for cyanobacteria than $\gamma\text{-Fe}_2\text{O}_3$ and Fe_3O_4 , due to its nanoparticle-induced oxidative stress [15].

Fe_3O_4 is a typical semi-metallic material that has a narrow band gap and a high conductivity of as high as $\sim 10^6 \text{ Sm}^{-1}$, which is ascribed to the electron exchange between Fe^{II} and Fe^{III} centers [16]. $\gamma\text{-Fe}_2\text{O}_3$ is an n-type semiconductor with a low conductivity. While the valence band of $\gamma\text{-Fe}_2\text{O}_3$ can lead to the oxidation of water, the conduction band of $\gamma\text{-Fe}_2\text{O}_3$ is not appropriate for hydrogen evolution.

The band gap energies of the IONPs samples were constructed by employing the Kubelka–Munk method, which uses the correlation between the Kubelka–Munk function and photon energy.[17] The band gap energies (E_g) obtained were determined to be 0.93 and 2.06 eV for Fe_3O_4 and $\gamma\text{-Fe}_2\text{O}_3$, respectively (**Figure 5.1**). A slight shift in the absorption edge in the direction of the high energy side, the so-called ‘quantum size effect’, was identified since the band gap of a semiconductor material is inversely proportional to the particle size [18]. Based on the E_g value, the conduction band (E_{cb}) and valence band potential (E_{vb}) of $\gamma\text{-Fe}_2\text{O}_3$ can be calculated by using the following equations:[19-21]

$$E_{\text{cb}}(\gamma\text{-Fe}_2\text{O}_3) = \chi(\gamma\text{-Fe}_2\text{O}_3) - E^{\text{C}} - 1/2E_g$$

$$E_{\text{NHE}} = - E_{\text{AVS}} - E^{\text{C}} \text{ (4.5 eV vs. NHE)}$$

$$E_{\text{vb}} = E_g - E_{\text{cb}}(\gamma\text{-Fe}_2\text{O}_3)$$

where χ is the absolute electronegativity of $\gamma\text{-Fe}_2\text{O}_3$ (5.88 eV), which is the geometric mean of the electronegativity of the constituent atoms [21], and E^C is the scaling factor associated with conversion of the normal hydrogen electrode scale (NHE) to the absolute vacuum scale (AVS) (~ 4.50 eV vs. NHE) [19, 21]. The E_{cb} and E_{vb} values were estimated to be 0.35 and 1.71 eV, respectively.

For the IONPs solution, a total amount of 0.02 g of IONPs was dispersed in 19.98 ml DI water to obtain a final concentration of 1×10^{-3} g/ml, and sonicated for uniform dispersion.

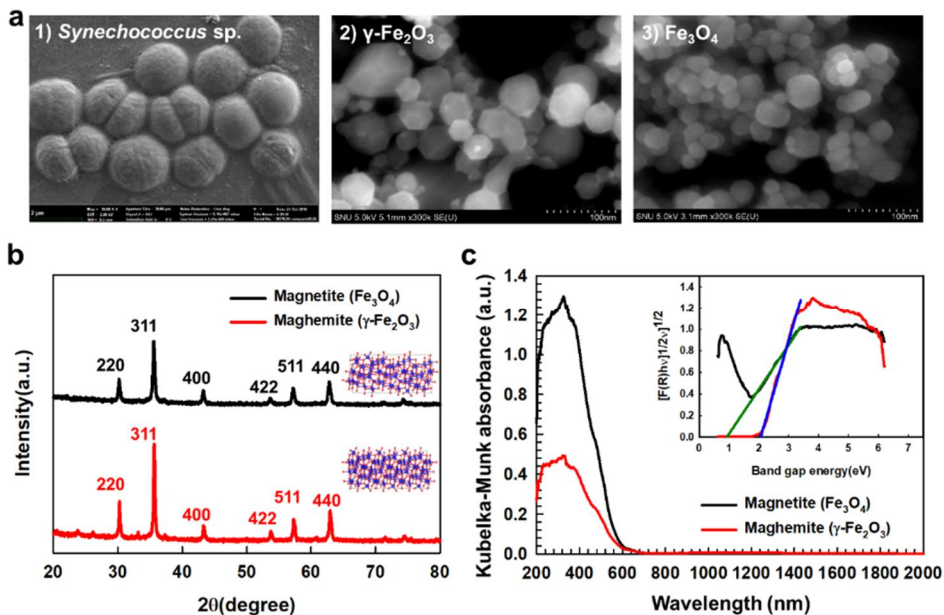


Figure 5.1 Characterization of the IONPs used in the experiment. (a) SEM images of *Synechococcus* sp., $\gamma\text{-Fe}_2\text{O}_3$, Fe_3O_4 . (b) X-ray powder diffraction (XRD) curves of the IONPs. The insets represent the atomic arrangement of magnetite (upper) and maghemite (lower). (c) UV-vis Kubelka-Munk absorbance. The inset is the relation between the band gap energy and $[F(R)h\nu]^{1/2}$ of iron oxide nanoparticles with estimated band gap energy values.

5.2.3. Nanoparticle attachment to *Synechococcus* sp.(cell – IONPs)

Poly-L-lysine solution (P8920, Sigma Aldrich) was used in this study as a cationic binder for linking the IONPs and microalgae. For the preparation of surface-modified IONPs, a small amount of binder was added into 1 ml of IONPs dispersion. Before the attachment of IONPs to the cell, the solution was sonicated using a probe type sonicator. 1 ml of cell suspension was added into 1 ml of IONPs suspension, followed by vortex mixing for 5 min to attach IONPs onto the surfaces of the *Synechococcus* sp.

5.2.4. Membrane electrode assembly (MEA)

The Nafion 117 membrane (180 μm thick) was purchased from Sigma Aldrich. Firstly, the membrane was stored in 0.5 M H_2O_2 at 80 $^\circ\text{C}$ for 1hr, then rinsed with 80 $^\circ\text{C}$ DI water for 1 hr. It was treated with 0.5 M H_2SO_4 for 1 hr at 80 $^\circ\text{C}$, and rinsed with 80 $^\circ\text{C}$ DI water for 1 hr. Platinum layer of about 200 nm thickness was sputtered on the carbon cathode in order to achieve high catalytic activity. The membrane and Pt-coated electrode were bonded via hot pressing. Hot pressing was performed on the membrane and the cathode at 125 $^\circ\text{C}$ for 80 s at a pressure of 5 MPa.

5.2.5. Characterization of cell – IONPs – NdFeB (Ni-Ni_xO_y) complexes

The zeta potentials of microalgae and IONPs were measured using a Zetasizer Nano Series instrument (Malvern Instruments Ltd., UK). For zeta potential measurements, 50 ml of cell suspension was centrifuged at 3,000 rpm for 10 min. The supernatant was removed, and cell was re-suspended in 10 ml of 0.1 M NaNO₃ to remove extra polymeric substances secreted by the algae. The pH of the washed bacterial solution and IONPs were adjusted from 4 to 9 with dilute HNO₃ or NaOH. Bacterial and bacterial – IONPs were fixed in 2% glutaraldehyde solution at 4 °C for 24 hrs. The solution was dehydrated using a series of ethanol (50%, 70%, 90%, 100%). The samples were prepared by placing a drop of suspension onto a copper tape, and dried at 50 °C. The morphology of the samples was characterized by field emission scanning electron microscopy (FE-SEM; MERLIN compact, ZEISS, Germany). Elemental analysis was performed using energy-dispersive X-ray spectroscopy (EDS). UV-vis spectra were obtained using UV Lambda 25 spectrometer (Perkin Elmer, USA). In order to estimate the band gap energies of the prepared samples, the optical properties were obtained by UV-3600 spectrometer (Shimadzu, Japan) with an integrating sphere attachment, using BaSO₄ as a reference. The phase composition of powder was identified using X-ray powder diffraction (XRD; New D8 Advance, Bruker, USA) with CuK α radiation (λ = 0.154056 nm). The composition of material and oxidation state of nickel atoms on the surface of the NdFeB were analyzed using X-ray photoelectron spectroscopy (XPS; AXIS-HSi, KRATOS, Japan).

5.2.6. Bio-photovoltaic device (BPV) fabrication and measurements

The bio-photovoltaic device was composed of three parts: a magnet chamber, an anodic chamber, and a cathodic cover. Four NdFeB permanent magnets (5 mm × 5 mm × 5 mm) were positioned at the top of a platinum mesh (**Figure 5.2**). The magnetic flux density of the magnets was measured to be 0.45 Tesla by using a Tesla meter (TM-701, KANETEC, Tokyo, Japan). The size of the anodic chamber was 11 mm × 11 mm × 7.5 mm, and a platinum mesh (Ametek, TN, USA) was placed in the middle of the anodic chamber. The MEA was fastened between the anodic chamber and cathodic cover, and fixed by using bolts. The bio-photovoltaic device was connected to external wires to complete the circuit. Cell-IONPs suspension was injected into the chamber through a tygon tube connected on the sidewall of the chamber using syringes. The syringes were kept connected throughout all experiments to prevent drying.

In order to characterize the photoelectrochemical properties of the BPV under light and dark environment. Cyclic photoresponse was measured with a 500 Ω resistance. Polarization curves of the BPV and impedance spectrum of the cell – IONPs were acquired using a potentiostat (VersaStat3, Princeton Applied Research, USA). Under dark and light conditions, polarization curves were acquired under pseudo-steady state condition with various load resistances (371, 500, 1.3 k, 3.25 k, 10.7 k, 20.3 k, 35.4 k, 55 k, 121.7 k, 162.5 k, 245.8 k, 0.506 M and 1.016 M Ω). The EIS measurement was made in the frequency range of 100 kHz to 100Hz with an amplitude of 10mV.

In order to trigger photosynthesis of cells in the BPV during the electrochemical experiments, a 150 W halogen lamp (KLS 150H-RC-150E, Kwangwoo, Korea) was used as the light source which provides the full spectrum of visible light with strong intensity near the absorption peak of microalgae (**Figure 5.1** and **Figure 5.3**). The intensity of the light source was measured using an integrating sphere (Labsphere Co., North Sutton, NH, USA) with 6 inch diameter monochromator (Acton Research Co., Acton, MA) attached to a photomultiplier tube (Hamamatsu

Photonics K.K., Japan). The light was illuminated at the side of the bio-photovoltaic device, resulting in an almost parallel angle of incidence on the device.

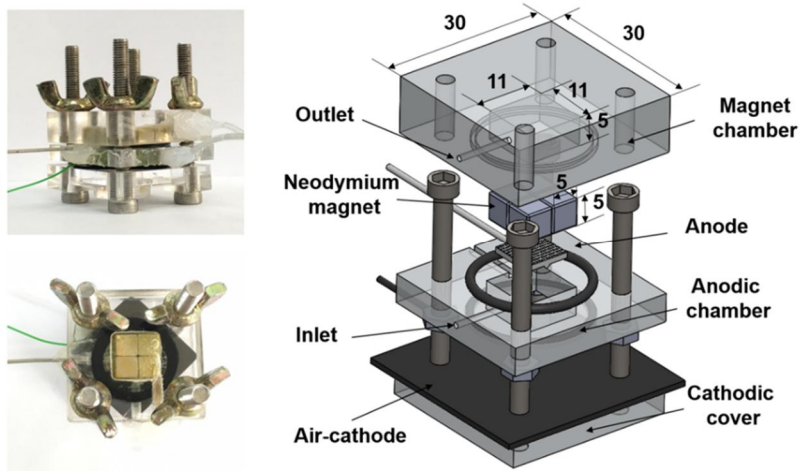


Figure 5.2 Pictures of the bio-photovoltaic device used in the experiment. Detailed dimensions are shown in the schematic illustration of the device and has a unit of mm.

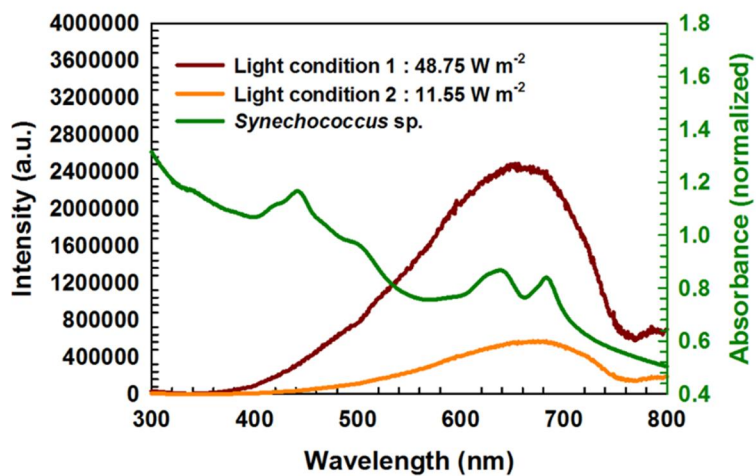


Figure 5.3 Absorption spectrum of *Synechococcus* sp. and irradiance spectrums of the halogen lamp used in this study. The light source provided a full spectrum of visible light for natural photosynthesis of *Synechococcus* sp.

5.3. Results and discussion

5.3.1. A new light-harvesting structure based on biological-inorganic hybrid system

In the current study, we designed a new light-harvesting structure based on the band gap energy and implemented a mediator-free biophotovoltaic (BPV) device with a high power density. A hybrid complex structure composed of *Synechococcus* sp. (exoelectrogenic cyanobacteria) and iron oxide nanoparticles (IONPs) was devised. High power density was achieved by harvesting electrons generated from both corrosion process of NdFeB and photosynthesis of *Synechococcus* sp. By selecting IONPs with appropriate band gap, electrons generated due to corrosion and photosynthesis under light illumination were effectively transferred to anode, which resulted in dramatic enhancement of the power density.

To increase the electron transfer to the anode, close proximity of cell and IONP is essential. In this study, the cell – IONPs complexes were fabricated. Since the surface charges of *Synechococcus* sp. and IONPs are all negative in the range of pH 6 to 9 (**Figure 5.4**), they repulse each other electrostatically. Therefore, we harness a cationic polymer binder to bind them together and form the cell – IONPs complex without any pH adjustment. When the cell – IONPs complexes are injected into the device, they experience the magnetophoretic force by the permanent magnet (NdFeB) placed above the platinum mesh (anode). Subsequently, they are placed in between the NdFeB and the Pt electrode due to ferrimagnetism, and the cell – IONPs – NdFeB complexes are formed in the system.

The schematic of the employed BPV device is displayed in **Figure 5.5**. The entire electrochemical reactions occurring in the cell, which include the electrochemical corrosion process of Ni and the biophotovoltaic process of the cell-IONPs complex, are demonstrated in **Figure 5.5b**. As shown in the SEM image, IONPs were adhered onto the surface of *Synechococcus* sp. (**Figure 5.5c**). To account for effectiveness of

the electron transport through the cell-IONPs complex, two types of iron nanoparticles with different band gaps were employed. The energy bands of the material systems are shown in **Figure 5.5d**. When light illuminates the device, the nickel surface of NdFeB is partially corroded, and turns into nickel oxide (referred to as NdFeB (Ni-Ni_xO_y)) while harvesting electrons from water. That is, the chemical constitution of the NdFeB surface has been partially changed during the experiments (**Figure 5.6**). In addition to the electrons from corrosion process, photosynthetic electrons are generated from the cells and induces water splitting upon light illumination. Since the microbial cells are surrounded by the semiconductive nanomaterials, they can not only behave as high energy electron generators but also act as an electron transfer conduit between the NdFeB (Ni-Ni_xO_y) and the anode [22].

For photo-electrochemical activity measurements, the cell – IONPs – NdFeB (Ni-Ni_xO_y) complexes were embedded in the device that was operated with 500 Ω external load at room temperature. The device was first illuminated for 500 s and then in a light/dark cyclic manner per 300 s. Once the cell-IONPs solution was injected into the device, the electrochemical cell was left alone for 5 min to allow the formation of cell – IONPs – NdFeB complexes and electron-rich biofilms on the anodic surface.

Figure 5.7a shows the photo response of the cell – IONPs (γ-Fe₂O₃, Fe₃O₄) – NdFeB (Ni-Ni_xO_y) in the BPV systems. The results revealed that the amplitude of the photo response current density decreased over time. This phenomenon was probably caused by two effects: (1) accumulation of the oxygen evolved during photosynthesis, which would divert electrons away from the anode; [23, 24] and (2) photoinhibition (photo-damage), which is an inherent feature of natural systems under extended illumination [25-27]. The cell – γ-Fe₂O₃ – NdFeB (Ni-Ni_xO_y) complexes showed an average dark current density of 1.690 A/m², and then a light induced current density of 2.518 A/m² under illumination, representing a relative net current density increase by 67%. On the other hand, the cell – Fe₃O₄ – NdFeB (Ni-Ni_xO_y) complexes yielded a relatively low average dark current density of 0.880

A/m^2 , and then a photo response current density of 1.487 A/m^2 , which implies a net current increase by 59% (**Figure 5.7b and Figure 5.7c**). The difference in current density is attributed to the different electron transport mechanism of IONPs harnessed in this system. When maghemite was used as IONPs, electrons were effectively transferred to the anode. On the other hand, magnetite transfers electrons ineffectively due to corrosion process because of the distinct difference of the bandgap structures with adjacent materials.

In order to investigate the effect of the amount of the complexes on the biophotovoltaic cell efficiency, additional experiments were carried out by injecting a cell – IONPs ($\gamma\text{-Fe}_2\text{O}_3$) solution which has the half concentration (**Figure 5.8**). For *Synechococcus* sp. solution, the optical density at 680 nm of the cell concentration was adjusted to 0.48 (2.46×10^7 cells/ml). For the IONPs solution, a total amount of 0.01 g of IONPs was dispersed in 19.99 ml DI water to obtain a final concentration of 5×10^{-4} g/ml. The two solutions were combined by using the method mentioned in the text. The amount of the complexes in the anode chamber can be roughly estimated by using the cells with similar size to *Synechococcus* sp.. According to the previous study [28], the average size and average dry weights of cyanobacterium *Microcystis aeruginosa* were $(2.29 \pm 0.61) \mu\text{m}$ and $(1.21 \pm 0.09) \times 10^{-11}$ g/cell, respectively. Therefore, 7.243×10^{-4} g of complexes are injected through the anodic chamber assuming that both particle and cells are bound. As a result of I–t measurements, a decreased max peak current density was obtained with average magnitude of 2.72 A/m^2 due to coarser source of the electron generation although the current does not decrease in proportion to the concentration.

Additional experiments were carried out to investigate the effect of the light intensity on the current density (**Figure 5.8**). For measurements, we set two different light conditions with the light intensity of 48.75 and 11.55 W/m^2 (subsequently called as light condition 1 and 2, respectively). The cell – IONPs ($\gamma\text{-Fe}_2\text{O}_3$) – NdFeB ($\text{Ni-Ni}_x\text{O}_y$) complexes were embedded in the device that was operated with 500 Ω external load at room temperature. The device was first illuminated for 500 s and then in a light/dark cyclic manner per 300 s. Under the

light condition 1, the average magnitude of the max peak current density is 4.24 A/m². On the other hand, the average magnitude of the max peak current density is 3.28 A/m² with the light condition 2, which implies reduction of the max peak current density by 33%. This difference in current density means that the light condition 1 is more proper condition than the light condition 2 for high performance.

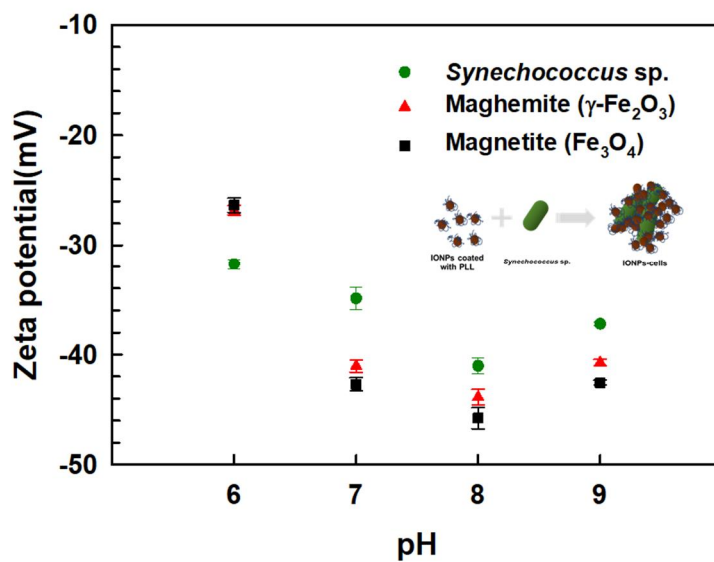


Figure 5.4 Zeta potential of samples. The zeta potentials of *Synechococcus* sp., maghemite, and magnetite were analyzed as a function of pH.

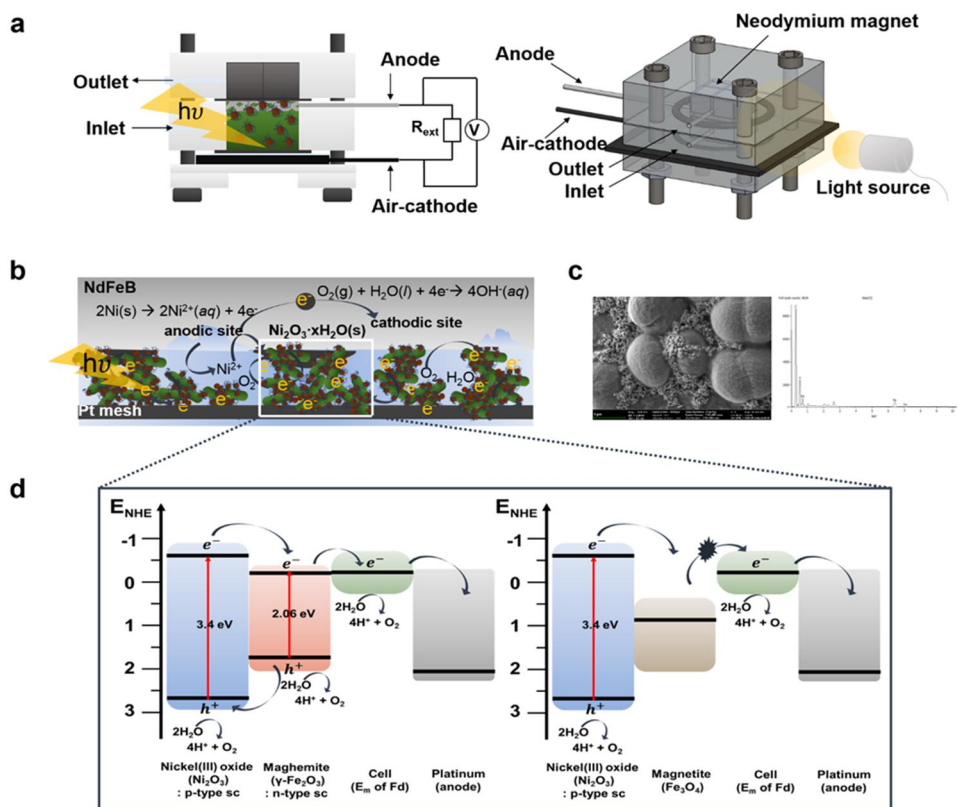


Figure 5.5 Bio-photovoltaic cell proposed in this study. (a) Schematic illustration of the bio-photovoltaic device. (b) Photocurrent generation from the biological-inorganic hybrid system. (c) SEM images of the *Synechococcus* sp. – IONPs complexes and energy-dispersive X-ray spectroscopy (EDS) of the complex. (d) Schematic energy band diagrams for possible electron transfer.

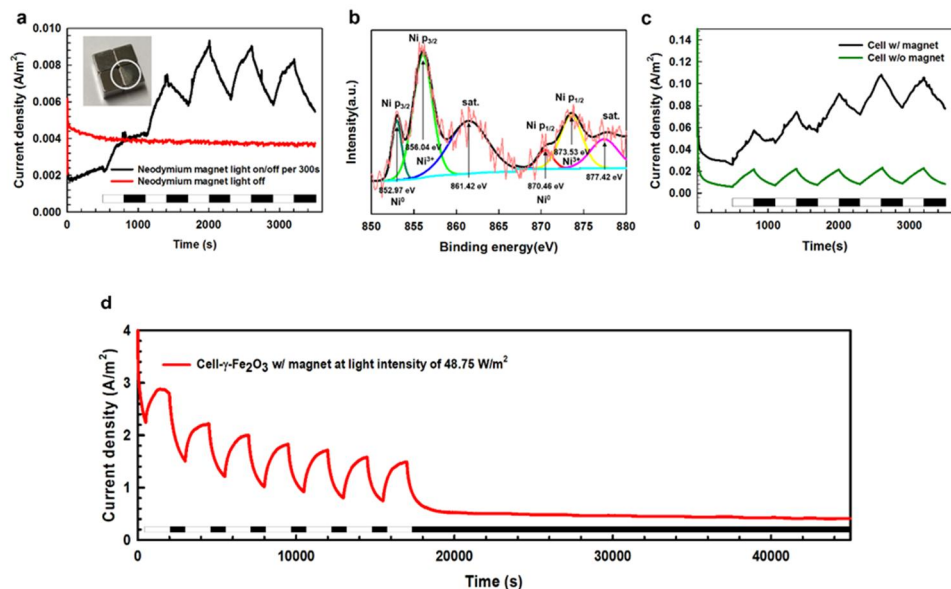


Figure 5.6 The effect of NdFeB on the performance of the electrochemical. (a) Photoresponse of NdFeB. Inset: The observation of NdFeB after the experiments. The intensity of the light source was set to 48.75 W/m^2 . (b) X-ray photoelectron spectroscopy (XPS) spectra of Ni $2p_{3/2}$ for the NdFeB surface. (c) Cyclic photoresponse of cells with magnet and without magnet with the light intensity of 48.75 W/m^2 . (d) Amperometric measurement from cell – IONPs ($\gamma\text{-Fe}_2\text{O}_3$) – NdFeB ($\text{Ni-Ni}_x\text{O}_y$) complexes with 500Ω external load at room temperature. The device was first illuminated for 500 s and then in a light/dark cyclic manner per 1500/1000 s until 18000 s. After 18000 s, the light was not irradiated.

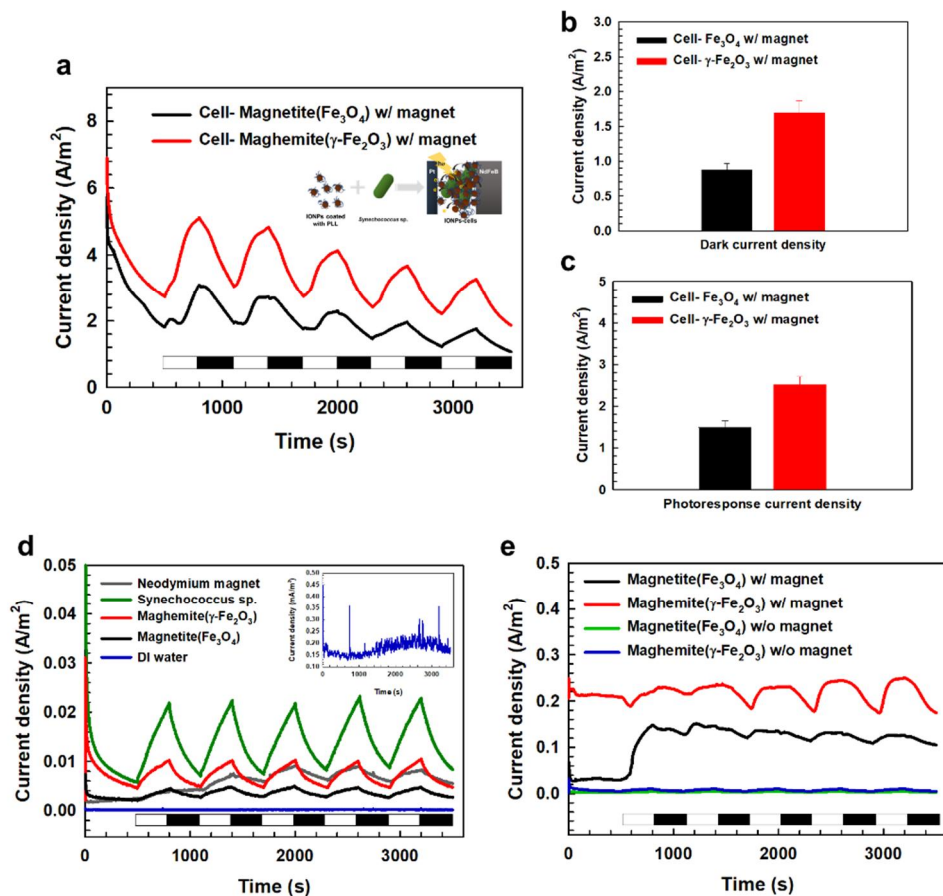


Figure 5.7 Bio-photoelectrochemical behavior of the bio-photovoltaic device with the light intensity of 48.75 W/m^2 . (a) Cyclic photoresponse of the complexes. Inset: the schematic image represents the architecture of the complexes (b) Dark current ($N=5$), (c) Light induced current ($N=5$). (d) Photoresponse of each component. (e) Enhanced photocurrent of the IONPs-NdFeB($\text{Ni-Ni}_x\text{O}_y$) complex. The white and black bars indicate the light and the dark periods, respectively.

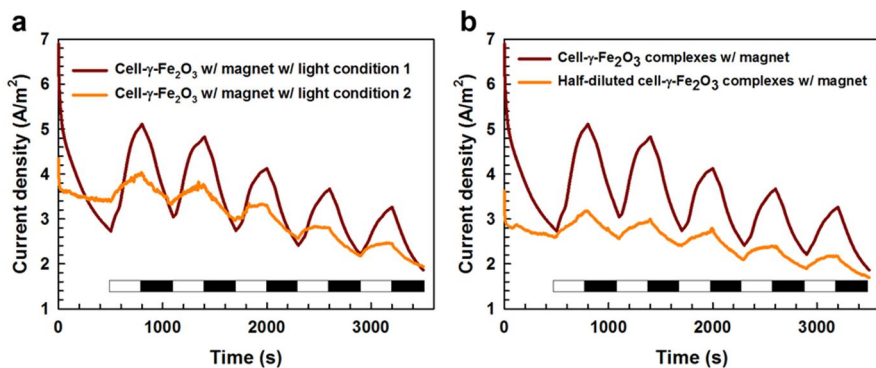
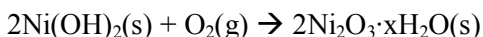
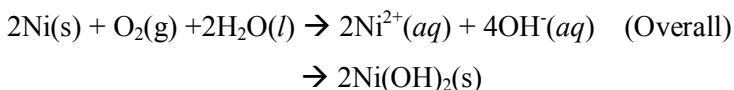
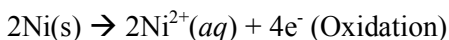


Figure 5.8 Bio-photoelectrochemical behavior of the bio-photovoltaic device. (a) Cyclic photoresponse of the cell – IONPs (γ -Fe₂O₃) – NdFeB (Ni-Ni_xO_y) complexes under different light conditions. (b) Cyclic photoresponse of the cell – IONPs (γ -Fe₂O₃) – NdFeB (Ni-Ni_xO_y) complexes with different concentration. The intensity of the light source was set to 48.75 W/m². Inset: Absorption spectra of the cell solution.

5.3.2. Characterization of the new light-harvesting structure

To investigate the contribution of the cyanobacteria, IONPs ($\gamma\text{-Fe}_2\text{O}_3$, Fe_3O_4), and NdFeB ($\text{Ni-Ni}_x\text{O}_y$) to the overall electrochemical performance during the light/dark cycling, separate experiments with each component were conducted under the same condition (**Figure 5.7d**). It was clear that there was no light response in the case of DI water during the light/dark cycles, and the other samples showed photo response currents. In particular, the *Synechococcus* sp. was found to have the highest photocurrent density of 0.022 A/m^2 . This can be explained by the exoelectrogenic property of bacterial biofilm for *Synechococcus* sp.. It has been reported that bacterial biofilms reduce the electrochemical potential losses due to the enhanced charge transfer rates of the biofilms [6, 23, 29]. In other words, the generated electrons are efficiently transferred to the anode via an indirect electron transfer mechanism.

NdFeB was employed in this study to pull the cell-IONPs complexes using the magnetic force. In general, nickel is highly resistant to corrosion. However, the metal corrosion is accelerated when nickel is exposed to oxygen, humidity, and especially ambient light. The corresponding experimental results showed the corrosion process (**Figure 5.6**). Under the light condition, the surface corrosion arose partially, thus generating the photo response current. The corrosion process of nickel surface under the light condition follows the mechanism below:



During the process, incipient hydrous oxides (IHOs) are formed in the pre-monolayer oxidation process on the heterogeneous metal surface. IHOs, active site

metal atoms, act as the effective oxidant for the catalytic/electrocatalytic reactions [30-33].

Following the process, the nickel surface turned into nickel oxide in part. In order to investigate the oxidation state of the surface, XPS analysis was carried out (**Figure 5.6**). Chemical state of nickel on the surface of the NdFeB is determined by the binding energies (BEs) of the Ni 2p_{3/2} peak. The main feature of the Ni 2p_{3/2} peak is located at 852.98 eV for Ni⁰, whereas the main feature of the Ni 2p_{3/2} peak is located at 856.04 eV for Ni³⁺. Previous research has supported that the BEs of 852.6 and 856.1 eV are assigned to Ni 2p_{3/2} XPS spectra for Ni⁰ and Ni³⁺, respectively [34]. The surface of the NdFeB (subsequently referred to as NdFeB (Ni-Ni_xO_y)) is comprised of Ni(III) oxide or Ni⁰ moieties at a rate of about 4 to 1. As a result, the surface shows good electrical conductivity ($\sim 10^7$ Sm⁻¹), acting as a p-type semiconductor.

Nickel ion is released from the metal surface during the corrosion process and are converted to nickel oxide by hydroxide ion and oxygen in the aqueous solution. Amperometric I-t measurements were performed on the biophotovoltaics in order to evaluate the long-term chemical stability of complexes and the overall device lifetime since a trace amount of Ni ions may affect photoactivity of cell. About 7.243×10^{-4} g of cell – IONPs (γ -Fe₂O₃) – NdFeB (Ni-Ni_xO_y) complexes were embedded in the device that was operated with 500 Ω external load at room temperature. For measurements, we set the light intensity as 48.75 W/m². The device was first illuminated for 500 s and then in a light/dark cyclic manner per 1500/1000 s until 18000 s. After 18000 s, the light was not irradiated in order to investigate the chemical stability of this system.

In first operation for 3500 s, the current is sharply decreased with a photoresponse current density of 0.915 A/m². In the following 6 cycles, the average photoresponse current density is 0.82 A/m² and decreases by 1.64×10^{-2} A/m² per cycle. After 18000 s, the dark current density showed stable baseline of 0.45 A/m² and did not show any light responses, as expected. That is, at the beginning of the experiment, the photoresponse current was not generated as much as the current

decreased, but which does not indicate that the system is unstable. In addition, the current does not drop rapidly after the first cycle due to the formation of biofilm providing a stable current path.

Nickel ion is an essential component of the [Ni-Fe] hydrogenase. It has been reported that the nickel supplementation plays important roles in the metabolism of bacteria [35, 36]. Nickel ion is likely to inhibit electron transport [35, 37] and induce severe chlorophyll degradation due to the displacement of Mg^{2+} from chlorophyll located at the antenna complex of photosystem II [38]. However, the concentration of nickel ion used for the energy harvesting is below the tolerable level [36, 39, 40]. Furthermore, the stimulation of nickel ion to cyanobacteria can lead to an enhancement in the activity of ferredoxin by increasing the electron transfer rate due to the surface and quantum size effects of nanoparticles [41, 42]. In addition, the presence of the magnetic field in cyanobacteria enhanced growth and photosynthetic activity of the cyanobacteria and/or microalgae with activation of light excitation in the photosynthetic electron transfer system, resulting in enhancement of photocurrent [43]. Thus, significantly enhanced photo response current was observed in the experiments (**Figure 5.6**). The total current density generated by cell – NdFeB was 0.087 A/m^2 under light illumination, which was 4 times enhancement in total current density compared with the control. Since NdFeB is a permanent alloy magnet, IONPs stick to NdFeB by the magnetophoretic force. The total current density of $\gamma\text{-Fe}_2\text{O}_3$ -magnet was 0.238 A/m^2 during the light period. The value was increased by about 24 times compared with that of $\gamma\text{-Fe}_2\text{O}_3$. Since the NdFeB ($\text{Ni-Ni}_x\text{O}_y$) acts as a p-type semiconductor, it forms a p-n junction with $\gamma\text{-Fe}_2\text{O}_3$. The inner electric field developed at the interface between the NdFeB ($\text{Ni-Ni}_x\text{O}_y$) and $\gamma\text{-Fe}_2\text{O}_3$ let the NdFeB ($\text{Ni-Ni}_x\text{O}_y$) region have a negative charge, while the $\gamma\text{-Fe}_2\text{O}_3$ region a positive charge. This heterojunction can be excited by light with proper photon energy to the band gap of nickel oxide and $\gamma\text{-Fe}_2\text{O}_3$. The generated electrons move towards the positive field, and the holes flow towards the negative field. On the other hand, the electron-hole separations are driven by the internal electric fields. According to the band edge position, the conduction band of

$\gamma\text{-Fe}_2\text{O}_3$ is lower than that of nickel oxide, which implies that the $\gamma\text{-Fe}_2\text{O}_3$ acts as an electron sink. Therefore, the photogenerated holes of the $\gamma\text{-Fe}_2\text{O}_3$ flow into the valence band of nickel oxide that induces enhanced charge separation. The enhancement of charge transfer is ascribed to the inner electric field assisted charge transfer, which reduces the probability of electron-hole recombination [20, 44, 45]. Thus, the highly increased current can be harvested from the $\gamma\text{-Fe}_2\text{O}_3$ – magnet during the light illumination. In addition, the total current density of Fe_3O_4 -magnet (i.e., 0.138 A/m^2) was increased by 34.5% compared with that of Fe_3O_4 . The narrow optical band gap allows Fe_3O_4 to act as an electron acceptor and transfer conduit that suppresses the electron-hole recombination of nickel oxide. This is also one of the main reasons for the enhancement of the photo response current.

The anomalous increment in the photocurrent observed in the presence of the intricate networks of the complexes implies that the cell – IONP ($\gamma\text{-Fe}_2\text{O}_3$, Fe_3O_4) works as an electron conduit between the $\text{NdFeB}(\text{Ni-Ni}_x\text{O}_y)$ and electrode. That is, the cell-IONPs complexes offer a direct electron pathway to the anode. The IONPs bound with cells facilitate the long-range electron transfer, and the generated biofilm also induces an indirect electron transfer to the electrode. They all serve as not only the electron generator but also the electron linkage. As a result, the current production was enhanced although the electron path was lengthened. **Figure 5.9** shows the results of the light induced current density. The total current density of the cell – IONPs ($\gamma\text{-Fe}_2\text{O}_3$, Fe_3O_4) – $\text{NdFeB}(\text{Ni-Ni}_x\text{O}_y)$ complexes was increased by a hundredfold compared with that of *Synechococcus* sp.

Since the possible electron transport pathway between the thylakoid membranes and the exterior of the *Synechococcus* sp. was not defined, the midpoint potential (E_m) of ferredoxin of the *Synechococcus* sp. was used for the energy band structure [46]. **Figure 5.5** demonstrates a schematic of the energy band structure. As expected, the $\gamma\text{-Fe}_2\text{O}_3$ and $\text{NdFeB}(\text{Ni-Ni}_x\text{O}_y)$ complex constructs a p-n junction, and thus yields effective electron flow towards the $\gamma\text{-Fe}_2\text{O}_3$. An energy barrier for electron transfer does not exist between the $\gamma\text{-Fe}_2\text{O}_3$ and the *Synechococcus* sp., since the E_{cb} level of the $\gamma\text{-Fe}_2\text{O}_3$ is close to the E_m of the cell. However, there is an energy barrier

between the Fe_3O_4 and the cell because the E_{cb} level gap between the Fe_3O_4 and the cell is about 0.5 V. Therefore, the cell – $\gamma\text{-Fe}_2\text{O}_3$ – $\text{NdFeB (Ni-Ni}_x\text{O}_y)$ has a higher photocurrent than that of the cell – Fe_3O_4 – $\text{NdFeB (Ni-Ni}_x\text{O}_y)$ since the E_{cb} is similar to E_{m} of the cell and it produces the electron itself. On the other hand, since the E_{cb} level of Fe_3O_4 is lower than the E_{m} of cell, electron hopping is more difficult in Fe_3O_4 than $\gamma\text{-Fe}_2\text{O}_3$. However, it can form a pseudo-conductive biofilm itself due to its high conductivity and transfer the electron through the anode effectively.

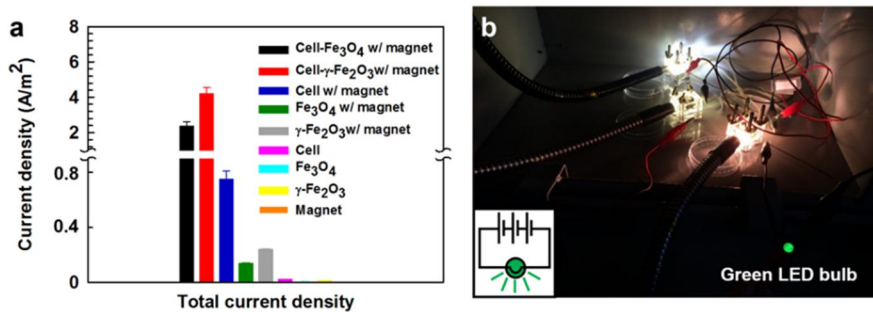


Figure 5.9 Bio-photoelectrochemical activities of the samples used. (a) Photocurrent density results. (b) Snapshot of the bio-photovoltaic device. The conventional green LED bulb was turned on using the harvested energy.

5.3.3. Photoelectrochemical activity of the BPV

Power output and polarization results were evaluated to characterize the performance of the electrochemical cell with the different cell – IONP complexes under light and dark conditions. Both curves were recorded by connecting various external resistances under the pseudo-steady state conditions [4]. It turned out that the cell – $\gamma\text{-Fe}_2\text{O}_3$ – NdFeB (Ni-Ni_xO_y) provided outstanding performances, i.e., peak power densities of 0.806 and 0.235 W/m² during the light and dark periods, respectively (**Figure 5.10**). The maximum power densities acquired with cell – Fe₃O₄ – NdFeB (Ni-Ni_xO_y) were 0.534 and 0.06W/m² during the light and dark periods, respectively. The power conversion efficiency η was 1.653% for cell – $\gamma\text{-Fe}_2\text{O}_3$ – NdFeB (Ni-Ni_xO_y) and 1.095% for cell – Fe₃O₄ – NdFeB (Ni-Ni_xO_y). Under light illumination, cell – $\gamma\text{-Fe}_2\text{O}_3$ – NdFeB (Ni-Ni_xO_y) and cell – Fe₃O₄ – NdFeB (Ni-Ni_xO_y) showed much higher average power density than those in the dark period by 3 and 9 times, respectively,. These results indicate that the power output originates from combination of the natural photosynthesis and artificial photosynthesis of the cell – IONPs – NdFeB (Ni-Ni_xO_y).

Figure 5.11 presents the Nyquist plots for cell – IONPs ($\gamma\text{-Fe}_2\text{O}_3$ and Fe₃O₄) – NdFeB (Ni-Ni_xO_y) under light and dark conditions. The inset shows the equivalent electrical circuit obtained by the parametric analysis. Here, R_s is the solution resistance, R_{ct} represents the charge transfer resistance, and CPE is a constant phase element of the solution-electrode interface. It was found that the R_{ct} decreased when light was on. This result indicated that the light illumination enhanced the electrochemical activity of the cell – IONPs ($\gamma\text{-Fe}_2\text{O}_3$ and Fe₃O₄) – NdFeB (Ni-Ni_xO_y). Because the shape of the graph indicates that the cell – $\gamma\text{-Fe}_2\text{O}_3$ – NdFeB (Ni-Ni_xO_y) has higher kinetic activity than the cell – Fe₃O₄ – NdFeB (Ni-Ni_xO_y), the enhancement of electro-kinetics is induced by the synergistic combination effect of the natural and artificial photocatalysts. In order to prove the feasibility of the device, 3 electrochemical devices were connected in series, and a conventional green LED bulb was turned on in a short time under light illumination (**Figure 5.9**).

The experimental result supported that the biophotovoltaic cell fabricated in this study could be employed as a robust power source for various electronic applications.

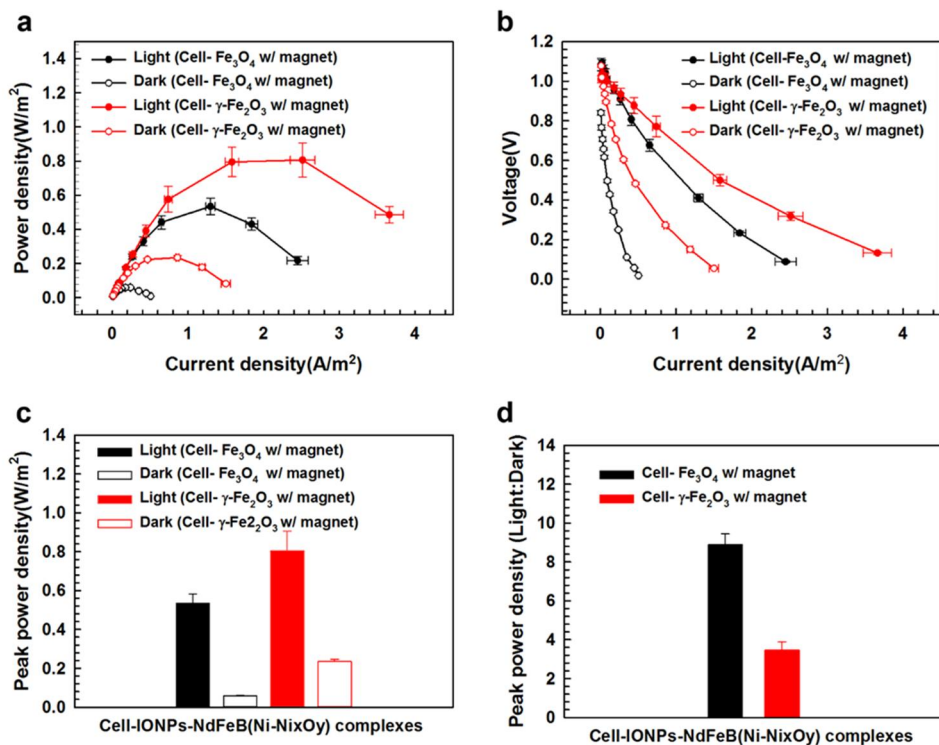


Figure 5.10 Photoelectrochemical performance of the bio-photovoltaic device with the light intensity of 48.75 W/m^2 . a) Power density results. b) Polarization curves of the device. c) Average peak power densities of the complexes ($N=3$). d) Ratio between the light and dark peak power densities.

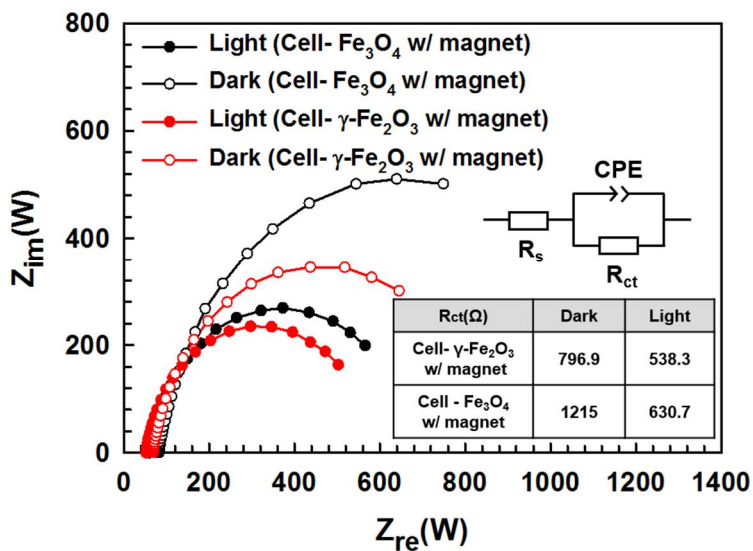


Figure 5.11 Nyquist plot of the cell – IONPs (γ - Fe_2O_3 and Fe_3O_4) – NdFeB ($\text{Ni-Ni}_x\text{O}_y$) complexes. The intensity of the light source was set to 48.75 W/m^2 at the light condition. The inset shows the equivalent circuit model, and the table lists the charge transfer resistance obtained from the modelling.

5.3.4. Comparison with other biophotovoltaic devices

For more in-depth understanding of the photo response results, additional experiments were carried out with a 1,000-fold concentrated cell solution (**Figure 5.12**). The average current density of 0.041 A/m^2 was generated, which was only about two-fold increment instead of 1,000-fold enhancement. The result was compared with other (sub)cellular biophotochemical studies in literature as listed in [47, 48]. It was revealed that the current study offered the highest current and power density among the relevant studies by controlling the electron transfer mechanism and cell position in a systematic manner.

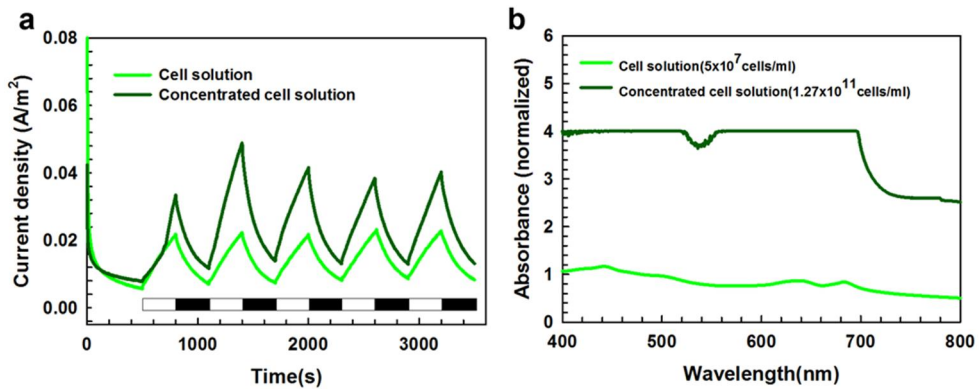


Figure 5.12 Experimental results with a 1,000-fold concentrated cell solution a) Photoresponse current measured with different cell solutions with the light intensity of 48.75 W/m^2 . The white and black bars indicate the light and dark periods. b) Absorption spectra of the cell solution and concentrated cell solution.

5.4. Conclusion

From the experimental evidence presented in this paper we conclude that a novel complex (*Synechococcus* sp. – IONPs (γ -Fe₂O₃, Fe₃O₄) – NdFeB (Ni-Ni_xO_y)) that can produce remarkably high bioelectrochemical energy. The hybrid system is capable of generating electrons by splitting water and transporting them to the electrode via very effective electron conduits. Different electron transport mechanisms were evaluated by changing the combination of materials and experimental conditions. We anticipate that this work could open a pathway for sustainable and robust photo-bioelectrochemical energy harvesting by employing proper material systems and microorganisms through materials science and biological energy engineering.

5.5. Bibliography

- [1] N. Quintana, F. Van der Kooy, M.D. Van de Rhee, G.P. Voshol, R. Verpoorte, *Applied microbiology and biotechnology*, 91 (2011) 471-490.
- [2] P. Bombelli, R.W. Bradley, A.M. Scott, A.J. Philips, A.J. McCormick, S.M. Cruz, A. Anderson, K. Yunus, D.S. Bendall, P.J. Cameron, *Energy & Environmental Science*, 4 (2011) 4690-4698.
- [3] X. Jiang, J. Hu, E.R. Petersen, L.A. Fitzgerald, C.S. Jackan, A.M. Lieber, B.R. Ringeisen, C.M. Lieber, J.C. Biffinger, *Nature communications*, 4 (2013).
- [4] B.E. Logan, B. Hamelers, R. Rozendal, U. Schröder, J. Keller, S. Freguia, P. Aelterman, W. Verstraete, K. Rabaey, *Environmental science & technology*, 40 (2006) 5181-5192.
- [5] Y. Yang, G. Sun, M. Xu, *Journal of Chemical Technology and Biotechnology*, 86 (2011) 625-632.
- [6] A.J. McCormick, P. Bombelli, A.M. Scott, A.J. Philips, A.G. Smith, A.C. Fisher, C.J. Howe, *Energy & Environmental Science*, 4 (2011) 4699-4709.
- [7] M. Rosenbaum, U. Schröder, *Electroanalysis*, 22 (2010) 844-855.
- [8] X. Li, T. Liu, K. Wang, T.D. Waite, *Environmental science & technology*, 49 (2015) 1392-1399.
- [9] C.I. Torres, A.K. Marcus, H.-S. Lee, P. Parameswaran, R. Krajmalnik-Brown, B.E. Rittmann, *FEMS Microbiology Reviews*, 34 (2010) 3-17.
- [10] P. Bombelli, T. Müller, T.W. Herling, C.J. Howe, T.P. Knowles, *Advanced energy materials*, 5 (2015).
- [11] L.H. Kim, Y.J. Kim, H. Hong, D. Yang, M. Han, G. Yoo, H.W. Song, Y. Chae, J.C. Pyun, A.R. Grossman, *Advanced Functional Materials*, 26 (2016) 7679-7689.
- [12] M.-H. Ham, J.H. Choi, A.A. Boghossian, E.S. Jeng, R.A. Graff, D.A. Heller, A.C. Chang, A. Mattis, T.H. Bayburt, Y.V. Grinkova, *Nature chemistry*, 2 (2010) 929-936.
- [13] J.P. Giraldo, M.P. Landry, S.M. Faltermeier, T.P. McNicholas, N.M. Iverson, A.A. Boghossian, N.F. Reuel, A.J. Hilmer, F. Sen, J.A. Brew, *Nature materials*, 13 (2014) 400-408.
- [14] N. Sekar, Y. Umasankar, R.P. Ramasamy, *Physical Chemistry Chemical Physics*, 16 (2014) 7862-7871.
- [15] C. Lei, L. Zhang, K. Yang, L. Zhu, D. Lin, *Environmental Pollution*, 218 (2016) 505-512.
- [16] N.N. Greenwood, A. Earnshaw, (1984).
- [17] R. López, R. Gómez, *Journal of sol-gel science and technology*, 61 (2012) 1-7.
- [18] S. Singh, R. Swarnkar, R. Gopal, *Bulletin of Materials Science*, 33 (2010) 21-26.
- [19] D. Channei, S. Phanichphant.
- [20] X. Lin, J. Xing, W. Wang, Z. Shan, F. Xu, F. Huang, *The Journal of Physical Chemistry C*, 111 (2007) 18288-18293.
- [21] Y. Xu, M.A. Schoonen, *American Mineralogist*, 85 (2000) 543-556.
- [22] R. Nakamura, F. Kai, A. Okamoto, K. Hashimoto, *Journal of Materials Chemistry A*, 1 (2013) 5148-5157.
- [23] H. Lee, S. Choi, *Lab on a Chip*, 15 (2015) 391-398.

- [24] Y. Zou, J. Pisciotta, R.B. Billmyre, I.V. Baskakov, *Biotechnol Bioeng*, 104 (2009) 939-946.
- [25] J.O. Calkins, Y. Umasankar, H. O'Neill, R.P. Ramasamy, *Energy & Environmental Science*, 6 (2013) 1891-1900.
- [26] S.B. Powles, *Annual Review of Plant Physiology*, 35 (1984) 15-44.
- [27] P. Sarvikas, M. Hakala-Yatkin, S. Dönmez, E. Tyystjärvi, *Journal of experimental botany*, 61 (2010) 4239-4247.
- [28] W. Hu, in, University of Missouri-Columbia, 2014.
- [29] J.-Y. Nam, H.-W. Kim, K.-H. Lim, H.-S. Shin, *Environmental Engineering Research*, 15 (2010) 71-78.
- [30] L. Burke, *Platinum Metals Review*, 38 (1994) 166-173.
- [31] L. Burke, G. Bruton, J. Collins, *Electrochimica acta*, 44 (1998) 1467-1479.
- [32] X. Shi, D. Simpson, M. Walters, C. Pettit, D. Roy, *Journal of The Electrochemical Society*, 161 (2014) H583-H592.
- [33] D.E. Simpson, K.E. Juda, D. Roy, *Electrocatalysis*, 9 (2018) 86-101.
- [34] C.D. Wagner, G. Muilenberg, *Handbook of X-ray photoelectron spectroscopy*, Perkin-Elmer, 1979.
- [35] P. Azeez, D. Banerjee, *Toxicological & Environmental Chemistry*, 30 (1991) 43-50.
- [36] M.J. Huertas, L. López-Maury, J. Giner-Lamia, A.M. Sánchez-Riego, F.J. Florencio, *Life*, 4 (2014) 865-886.
- [37] S. Chillappagari, A. Seubert, H. Trip, O.P. Kuipers, M.A. Marahiel, M. Miethke, *Journal of bacteriology*, 192 (2010) 2512-2524.
- [38] D. Carrieri, G. Ananyev, A.M.G. Costas, D.A. Bryant, G.C. Dismukes, *International Journal of Hydrogen Energy*, 33 (2008) 2014-2022.
- [39] C. Dupont, D. Johnson, K. Phillippy, I. Paulsen, B. Brahmsha, B. Palenik, *Applied and environmental microbiology*, 78 (2012) 7822-7832.
- [40] I.B. Rodriguez, T.-Y. Ho, *Scientific reports*, 4 (2014) 4445.
- [41] A. Gadhe, S.S. Sonawane, M.N. Varma, *International Journal of Hydrogen Energy*, 40 (2015) 4502-4511.
- [42] J. Wang, W. Wan, *Bioresource technology*, 99 (2008) 8864-8868.
- [43] M. Hirano, A. Ohta, K. Abe, *Journal of fermentation and bioengineering*, 86 (1998) 313-316.
- [44] M. Long, W. Cai, J. Cai, B. Zhou, X. Chai, Y. Wu, *The Journal of Physical Chemistry B*, 110 (2006) 20211-20216.
- [45] Z. Zhang, C. Shao, X. Li, C. Wang, M. Zhang, Y. Liu, *ACS applied materials & interfaces*, 2 (2010) 2915-2923.
- [46] K. Wada, R. Masui, H. Matsubara, L. Rogers, *Biochemical journal*, 252 (1988) 571-575.
- [47] Min Jung Kim, Seoung Jai Bai, Jae Ryoun Youn, Young Seok Song, *Journal of Power Sources*, 412 (2019) 201-310.
- [48] A.J. McCormick, P. Bombelli, R.W. Bradley, R. Thorne, T. Wenzel, C.J. Howe, *Energy & Environmental Science*, 8 (2015) 1092-1109.

Chapter 6

A broadband multiplex living solar cell

6.1. Introduction

We are faced with a grave energy crisis as the quantity of fossil fuels are going down. Under this circumstance, solar energy has been used as an alternative source of energy that is environmentally sustainable. In particular, biological photovoltaics (BPV) so-called “living solar cells” have emerged promising technologies that generate electricity from the photosynthetic organisms which convert solar energy into chemical energy by photosynthesis. One of the photosynthetic organisms, cyanobacteria, has the same electron transport chain as the plant. They utilize water, light, and carbon dioxide to produce electron, releasing electrons to the exterior *via* a type IV pili, known as highly conductive [1]. In BPV, the electrons generated from the photosynthetic bacteria can be transferred to the anode through an external electrical circuit to the cathode, thus producing electricity. Simultaneously, hydrogen secreted from cells are passed through the proton exchange membrane (PEM) to the cathode chamber, where the two electrons are combined with the protons and oxygen to convert water at the cathode.

A particularly advantages of BPV have been reported for the following reasons: (1) BPV generate electricity in both light and dark period whereas photovoltaics (PV) produce electricity only in light period [2]. (2) BPV produce power from solar energy using only water as an electron source, while microbial fuel cell (MFC) use heterotrophic bacteria to produce the chemical energy stored in organic matter [3]. (3) BPV can directly harness the photosynthesis having a high quantum efficiency. (4) BPV rely on living organisms as self-healing different from other (semi-)PV. (5)

The cost of producing BPV can be low since photosynthetic bacteria are abundant and environmental friendliness. Therefore, BPV possess inherently promising technology for generating renewable energy.

To increase the efficiency of solar energy conversion, current researches have focused on immobilizing cell onto the electrode. Bombelli *et al.* [4] allow cells to settle onto the electrode for 12h in order to facilitate biofilm for reducing electrochemical potential losses. In addition, Bombelli *et al.* [5] developed a microfluidic device BPV that operate without requiring a membrane or mediator. They permit cells to settle on the anode for 24h after injection, yielding high power density above 100 mW/m². Moreover, Sekar *et al.* designed the cell immobilized on a carbon nanotube (CNT) modified electrode in order to enhance direct electron transfer [6]. These approaches have the disadvantage of being time consuming. Therefore, a different strategy is needed to improve the performance of BPV.

In recent research, a study combining MFC and PV has been developed [7]. Qian *et al.* reported solar-assisted microbial photoelectrochemical system which is composed of hematite nanowire-arrayed photoelectrode, and *Shewanella oneidensis* MR-1. The enhanced photocurrent was attributed both the MR-1 cells and photoanode. MR-1 cells are capable of producing electricity by consuming organic matter and hematite photoanode has ability to collect the electron and produce electron by water splitting. In addition, cells thrive on the surface of the electrode and the morphology of the cells was not contaminated. Moreover, our previous work [3] reported the feasibility of generating electricity by combining BPV and nanoparticle. Boosting power efficiency of BPV was obtained by using only light and water *via* a long electron transfer conduit to the electrode.

Recently, enhanced cultivation methods of photosynthetic organisms were reported by utilizing the wavelength specific back scattering from the metal nanoparticles due to the localized surface plasmon resonance (LSPR) effect [8, 9] or by shifting the UV-A radiation to blue light by fluorescent material [10]. LSPR is the localized resonant oscillation of plasmon arose from a strong coupling

between light and the sufficient free electrons in the metal nanoparticle, which has a great potential in energy issue due to its characteristic decay mechanisms that include the far-field scattering effect [11]. Those two approaches have a common purpose in the way of boosting the specific wavelength range of the light source which is the favorable spectral region for the photosynthetic organism growth.

In this respect, a considerable strategy can be established to further enhance the performance of the combined BPV-PV system. That strategy is to fully utilize the broadband wavelength (300 - 700 nm) of the light, including to enhance the favorable spectral region (390 - 500 nm and 600 - 700 nm) for photosynthesis, for generating the electrical energy with high efficiency. This broadband electricity production is expected to be feasible by introducing a photoelectrode made of a plasmonic hybrid nanostructure (semiconductor/metal).

Zinc oxide nanorods (ZnO NR) have recently got great attention as complementary structure in solar cells for increasing the light harvesting efficiency, due to the high light scattering effect in the visible wavelength range (390-700 nm) and thus the longer effective optical path length [12, 13]. Moreover, ZnO NR is the preferred electrode for solar cells due to a wide and direct bandgap and high carrier mobilities [14]. Meanwhile, plasmonic-enhanced photovoltaic cells have been also actively studied to improve the energy conversion efficiency by using metal nanoparticles such as gold nanoparticles (Au NP) and silver nanoparticles (Ag NP) [15-18]. As mentioned above, LSPR can be decayed via characteristic decay mechanism such as near-field enhancement, far-field scattering, hot-electron injection (or plasmonic induced charge separation, PICS), plasmon-induced resonant energy transfer (PIRET) and plasmonic heating [18]. In the sense, plasmonic-enhanced BPV-PV (cell / ZnO NR / metal) can take advantage of PICS, far-field scattering and near-field enhancement aided by the hybrid nanostructure, for increasing the current production.

In this study, an anomalously enhanced bioinorganic photovoltaic cell was successfully demonstrated based on the broadband multiplex living solar cell (Cell

/ ZnO NR / Au NP) system, by making the best use of the hybrid nanostructure (ZnO NR /Au NP) as an electric energy boosting photoanode. In our system, electrons were generated in multiple paths including (i) the photosynthesis of the cells (390-500 nm, 600-700 nm) (ii) intraband transition in Au NP due to the LSPR (around 520 nm), and interband transition in (iii) ZnO NR (below 364 nm) in the almost full spectral range of the light source (300-800 nm), which led to the highly efficient system (**Figure 6.1**). Furthermore, the photosynthetic activities of the cells were extremely enhanced with the effect of the strong far-field scattering from ZnO NR / ITO and ZnO NR / Au NP / ITO, compared to bare ITO anode. It is noteworthy that the introduced novel broadband multiplex living solar cell would enable to enhance solar energy harvesting efficiency.

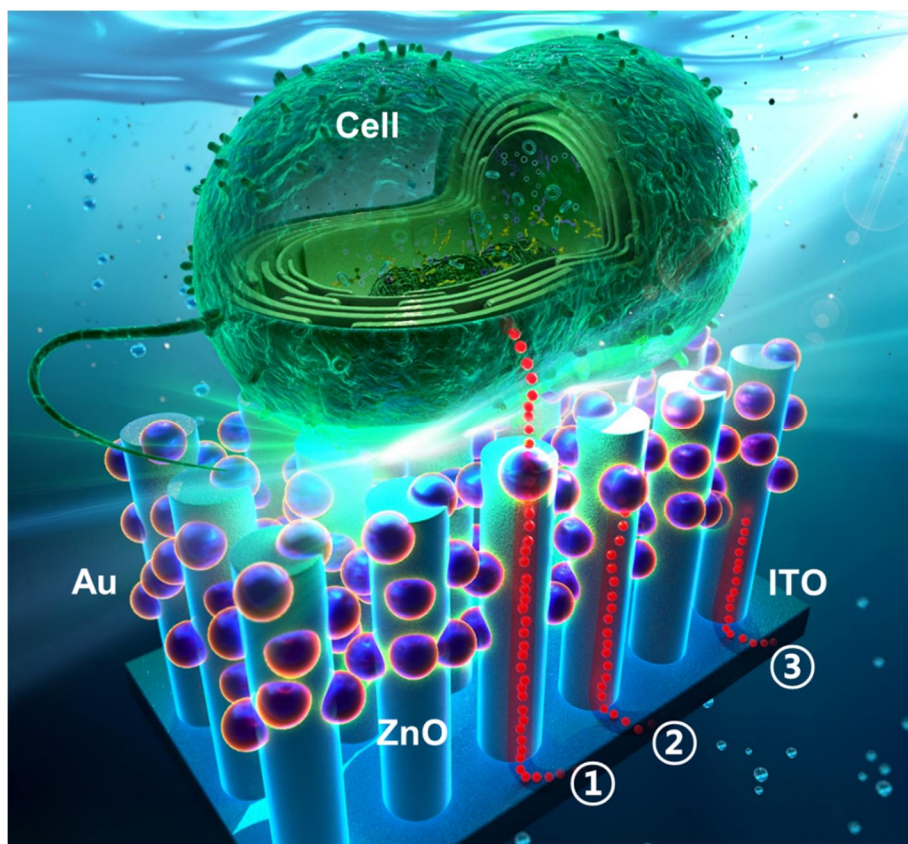


Figure 6.1 Schematic illustration of the broadband multiplex living solar cell proposed in this study. Photocurrents are generated from multiple mechanism simultaneously: (1) the photosynthesis of the cell, (2) hot-electron generation from Au NP (PICS), and (3) interband transition in ZnO NR.

6.2. Experimental

6.2.1. Bacterial culture conditions and characterization

A wild-type strain of *Synechocystis* sp. PCC 6803 (subsequently called *Synechocystis*) was obtained from Prof. Y.-I. Park's Laboratory at Chung-Nam National University, Daejeon, Korea. The cell was grown on 1% BG-11 agar plate buffered with 0.3% (w/v) sodium thiosulphate ($\text{Na}_2\text{S}_2\text{O}_3$) at 28 °C for 2 weeks. The cells were re-suspended in 1% BG-11 freshwater solution (C3061, Sigma Aldrich). *Synechocystis* is well known as a coccoid cyanobacterium (**Figure 6.2**) and its size varies from 1 to 3 μm .

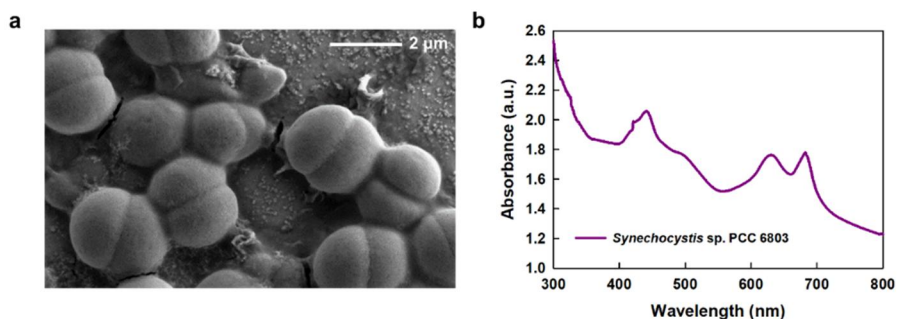


Figure 6.2 Characterization of the cell. (a) Scanning electron microscopy (SEM) of *Synechocystis* sp. PCC 6803 showing two-partially fused spherical lobes in shape, about 1 to 3 μm in diameter. The scale bar denotes a length of 2 μm. (b) Absorption spectrum of *Synechocystis* sp. PCC 6803. It denotes that both chlorophyll (Chl) a and b accumulate in the light in a *Synechocystis* sp. PCC 6803 strain.

6.2.2. Preparation of nanostructured anodes

ZnO NR / ITO anode was fabricated by using the hydrothermal growth of ZnO NR on the ITO glass and then ZnO NR / Au NP / ITO anode was fabricated by the following photochemical reduction of Au NPs on the surfaces of ZnO NR of ZnO NR / ITO anode. Details on the processes are explained in literature [19, 20]. Briefly, the hydrothermal growth was conducted in two steps, seeding and growth. First, a glass substrate was cleaned with acetone, DI water and isopropyl alcohol in order. For the seeding step, seed solution (zinc acetate ($\text{Zn}(\text{C}_2\text{H}_3\text{O}_2)_2$) dissolved in ethanol, 0.03 M) was spin-coated on the ITO glass three times at 2000 rpm for 10 s, followed by annealing at 250 °C for 20 min to remove residual solvent and form crystal seeds. For the growth step, the seed-coated ITO glass was immersed in the growth solution (zinc nitrate hexahydrate ($\text{Zn}(\text{NO}_3)_2 \cdot 6\text{H}_2\text{O}$) and hexamethylenetetramine ($\text{C}_6\text{H}_{12}\text{N}_4$) dissolved in DI water, 0.03 M) at 90 °C for 2 h and rinsed several times. Then, for the photochemical reduction, ZnO NR / ITO was immersed in chloroauric acid (HAuCl_4) aqueous solution (3 mM) and irradiated with an UV lamp (UVT series, DongSeo, Chungnam, Korea) for 2 h.

6.2.3. Characterization of Materials

The morphology of the samples was characterized by field emission scanning electron microscopy (FE-SEM; MERLIN compact, ZEISS, Germany). The phase composition of electrode was identified using X-ray powder diffraction (XRD; New D8 Advance, Bruker, USA) with $\text{CuK}\alpha$ radiation ($\lambda = 0.154056$ nm). UV-vis spectra were obtained using UV Lambda 25 spectrometer (Perkin Elmer, USA).

6.2.4. Angle-dependent light scattering measurement

Figure 6.3 illustrates an experimental set-up of the angle-dependent light scattering measurement. The sample, a halogen lamp, and optical instruments are fixed on a motorized rotation stage. The edge of the sample was illuminated using a halogen lamp, an aperture, a convex lens, and a slit. The spectrum of the light scattered by the sample was measured by a spectrometer (Maya 2000, Ocean Optics Inc.) with automatic rotation of the stage.

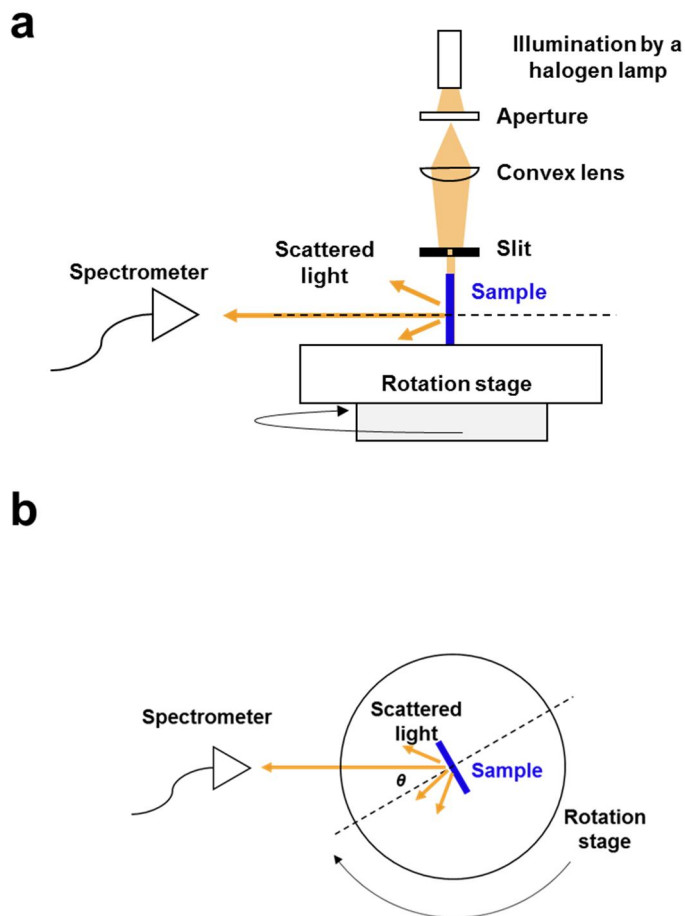


Figure 6.3 Schematic illustration of far-field scattering measurement. The schematic images show (a) side view and (b) top view of the optical set-up, respectively. The scattered light was detected by the spectrometer with respect to the rotating angles.

6.2.5. Membrane electrode assembly (MEA)

The Nafion 117 membrane (274674, Sigma Aldrich) was stored in 0.5 M hydrogen peroxide (H_2O_2) at 80 °C for 1hr, then soaked with 80 °C DI water. It was stored in 0.5 M sulfuric acid (H_2SO_4) for 1 hr at 80 °C, and rinsed with 80 °C DI water. Platinum was sputtered on the carbon cathode about 200 nm thickness in order to achieve high catalytic activity. The membrane and Pt-coated electrode were bonded *via* hot pressing. Hot pressing was conducted on the membrane and the cathode at 125 °C for 80 s at a pressure of 5 MPa.

6.2.6. Device fabrication

The device was composed of three parts: a photoanode, an anodic chamber, and a MEA. The size of the anodic chamber was 11 mm × 11 mm × 5 mm, and a photoanode was placed in the bottom of the anodic chamber. The MEA was placed between the anodic chamber and cathodic cover, and all components were fixed by using bolts. The device was connected to external electrical circuit to complete the circuit. Cell solution was injected into the anodic chamber through a flexible tube (Tygon E-3603, ACF00001, Saint Gobain, Tokyo, Japan) connected on the sidewall of the chamber using a 3ml disposable plastic syringe. In order to prevent drying, the flexible tubes were kept clamped throughout all experiments. The schematic image of the device is shown in **Figure 6.4**.

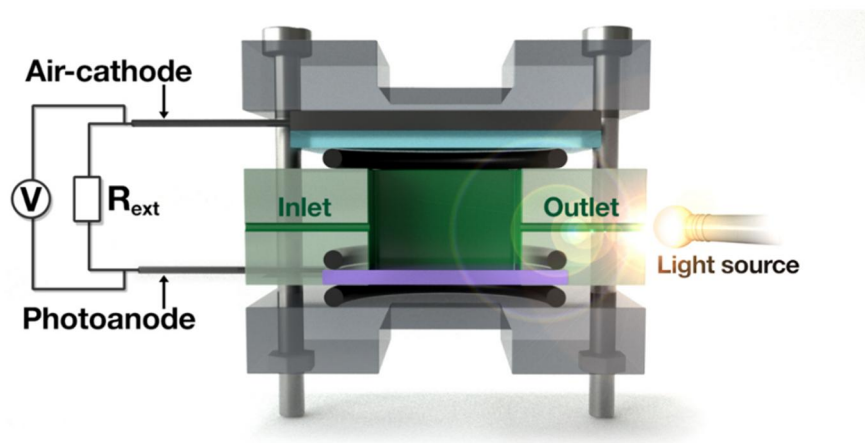


Figure 6.4 Schematic image of the device. The device is consist of three parts: a photoanode, an anodic chamber, and a MEA. The light is irradiated to the side of the anodic chamber with an intensity of 48.75 W/m^2 .

6.2.6. Electrochemical measurements

All electrochemical experiments were conducted using a potentiostat (VersaStat3, Princeton Applied Research, USA) at the room temperature. Under light condition, polarization curves were acquired by recording the current, I , under pseudo-steady state condition with various load resistances (72.4, 114.1, 271.5, 0.587 k, 0.803 k, 1.26 k, 2.97 k, 8.12 k, 12.94 k, 32.1 k, 1.002 M Ω). The voltage, V , was derived from Ohm's law $V=R_{ext}\cdot I$ and the delivered power, P , is given by $P= I^2R_{ext}$. The amperometric response measured as a function of time with 510 Ω under alternative light and dark conditions.

In order to stimulate the photosynthetic activity of cells, a 150 W lamp (KLS 150H-RC-150E, Kwangwoo, Korea) was used as the light source which provides the full spectrum of visible light with strong intensity (**Figure 6.5**). The intensity of the light source was characterized using an integrating sphere (Labsphere Co., North Sutton, NH, USA) with 6 inch diameter monochromator (Acton Research Co., Acton, MA) attached to a photomultiplier tube (Hamamatsu Photonics K.K., Japan).

To characterize the redox activity of the photoanode, cyclic voltammogram (CV) was performed in a solution containing 50 mM potassium ferricyanide and a supporting electrolyte of 0.1 M KCl. First, a photoanode was placed in a jig filled with a 0.1 M KCl solution, and a measurement was conducted. Then, the electrode was cleaned with DI water, and placed in a jig filled with a 50 mM ferricyanide/0.1 M KCl solution. The potential bias range was set between -0.2 V and 0.2 V, while the scan rate was 0.05 V/s.

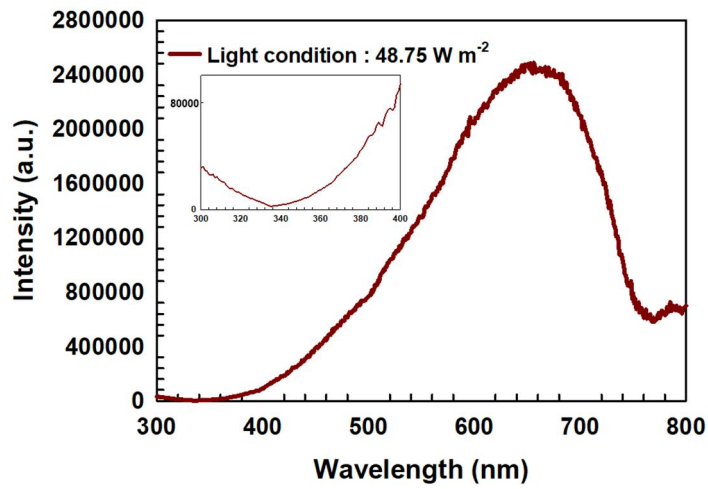


Figure 6.5 Irradiance spectrums of the halogen lamp used in this study. The light source provided a full spectrum of visible light for natural photosynthesis of *Synechocystis* sp. PCC 6803

6.2.7. Viability test

The flow cytometric analysis was conducted by using a BD Accuri C6 Flow Cytometer (BD Biosciences, San Jose, CA, USA). The cell solution of before and after the experiment was employed. Assessment of bacterial viability by using the LIVE/DEAD[®] Bacterial Viability Kit (Thermo Scientific, Rockford, IL, USA) was applied to estimate both viable and total counts of bacteria. Two nucleic acid stains (the green-fluorescent SYTO 9 stain for live cells and the red-fluorescent propidium iodide stain for dead cells) were added into 1ml of cell solution for 1.5 μ L each and incubated for 15 min at room temperature. 10 μ L of the microsphere suspension was added to the stained cell sample. Then, the sample was analyzed by flow cytometry. In addition, the cell / ZnO NR / Au NP / ITO electrode after an operation was employed for viability test by using a fluorescent optical image. After an operation, electrode was rinsed gently with PBS buffer and stained the green-fluorescent SYTO 9.

6.3. Results and discussion

6.3.1. Characterization of the photoanode

The cross-section view of the SEM images for the fabricated ZnO NR and Au NP / ZnO NR on the ITO glass are shown in **Figure 6.6a** and **Figure 6.6b**, respectively. The Au NP are well-deposited on the surfaces of the ZnO NR, and the average diameter of the Au NP is about 30 nm. The average diameter and length of the ZnO NR are about 80 nm and 800 nm, respectively. These values were used for constructing the geometric model for the numerical simulation. Absorption spectra of the photoanodes shown in **Figure 6.6c** indicate that ZnO NR absorb great amount of the UV-region light due to their large band gap (3.4 eV) [19] and that Au NP absorb great amount of the light around the resonance peak of 520 nm due to the LSPR phenomenon.

The X-ray diffraction patterns of pristine ZnO NR and those decorated with Au NP were shown in **Figure 6.6d**. The measurements have been done for a 2θ diffraction angle scans between 20° and 80° on multilayer structures deposited on ITO glass. The asterisk “*” indicates the position of the ITO substrate. It can be clearly seen that all diffraction peaks in the samples correspond to the standard diffraction of a hexagonal ZnO crystal (JCPDS 79-0206). The XRD patterns of corresponding ZnO NR exhibited reflection peaks at 31.66° (100), 34.46° (002), 36.37° (101), 47.67° (102) and 62.91° (103). For the Au NP / ZnO NR, additional peaks corresponding to face-centred cubic Au structure ((1 1 1) and (2 0 0)) were clearly observed at $2\theta = 38.25$ and 45.34° [21, 22]. From the XRD pattern, it can be inferred that the (002) peak for the microcrystallites of the ZnO grows preponderantly, indicating ZnO-NR preferred anisotropic growth along the [001] direction of the ITO substrate [23, 24]. The crystallite size of Au NP was calculated from the broadening of XRD peaks, are about 30.89 nm using the Scherrer equation. The result was in consonance with the SEM data.

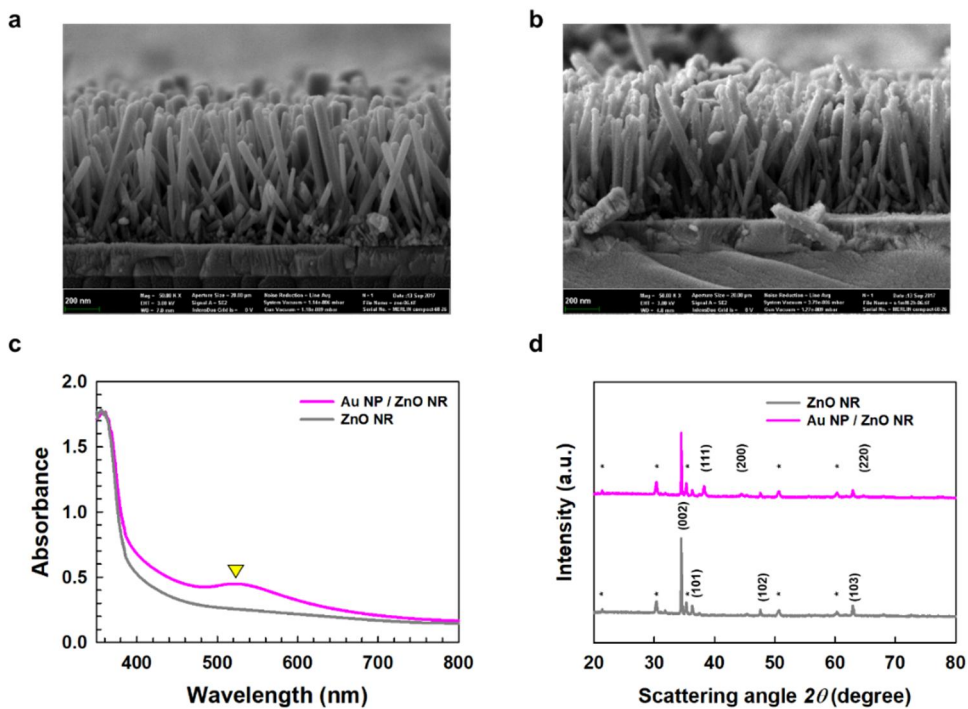


Figure 6.6 Characterization of the photoanode. SEM images of the fabricated (a) ZnO NR, and (b) Au NP / ZnO NR. (c) Absorption spectrum of the photoelectrodes: ZnO NR and Au NP / ZnO NR. (d) X-ray powder diffraction (XRD) curves of the ZnO NR grown on an ITO substrate (*) Au NP / ZnO NR grown on an ITO substrate (*).

6.3.2. Photoelectrical properties of photoanode

The deposition of Au NP onto the surface of the ZnO NR greatly alters a fast interfacial charge transfer process and affects an effective separation of photo-generated electron–hole pairs [25]. In order to verify that the as-synthesized ZnO NR and ZnO NR loaded with Au NP may have potential application in high-performance electrochemical photoanode, the samples were configured as electrodes to evaluate their electrochemical behavior of $[\text{Fe}(\text{CN})_6]^{3-/4-}$ redox activity (**Figure 6.7a**). As a control, a scan was first carried out with bare ITO electrode in 0.1 M KCl in the range 0.2 to -0.2 V (**Figure 6.7a**, dashed gray curve). The photoelectrochemical measurements of ZnO NR and Au NP / ZnO NR photoanode in the presence of the $[\text{Fe}(\text{CN})_6]^{3-/4-}$ as a mediator were first performed under light irradiation at a scan rate of 0.05 V/s in a potential range of 0.2 to -0.2 V. The peak current of the ZnO NR flat electrode was about 51 μA , while the peak current from the Au NP / ZnO NR electrode was about 96 μA . That is, the electrochemical surface area of Au NP / ZnO NR electrode is 1.88-fold larger than that of the ZnO NR. From the curves, it can be seen that the inclusion of Au NP increased the electroactive surface area of the electrode. This results indicated that Au NP / ZnO NR electrode displays a higher rate of electrode reaction [26].

The photoelectrochemical behavior of the aforementioned two samples was characterized under alternate light–dark conditions in **Figure 6.7b**. For the measurements, the electrodes were assembled in order as shown in **Figure 6.4**. It is apparently demonstrated that the photo-induced current is drastically increased when the light is on. The photocurrent was exhibited in three steps [27-29]: (i) The photo-induced current increased drastically due to the separation and quick transfer of photoinduced charges upon illumination. (ii) The photo-induced current decreased rapidly by the recombination of the photoinduced charges. (iii) The photo-induced current reached a steady state that balance of generation and recombination of photogenerated charges was achieved. The Au NP / ZnO NR

electrode shows enhanced amperometric responses as compared with ZnO NR electrode, suggesting that Au NP promote the photoelectrochemical properties of ZnO NR under the light. These results are consistent with those obtained using the CV as shown in **Figure 6.7a**.

The enhanced photocurrent of Au NP / ZnO NR / ITO electrode could be attributed to the increased visible light-harvesting efficiency via LSPR effect. In other words, this effect can be ascribed to the additional electrons injected from Au NP to ZnO NR in the visible light region. The additional electrons can be generated in Au by two ways: (i) the intraband excitation (LSPR-induced hot electrons or Landau damping) in the conduction band, and (ii) the interband excitation from the d-band to the conduction band [30]. Intraband excitation occurs around the LSPR resonant wavelength and the efficient interband excitation generally needs the absorption of photon with energy above 2.4 eV (517 nm) [31]. When ZnO is in contact with Au, Schottky junction is formed at the interface. Typical Schottky barrier at ZnO-Au interface is only about 0.9 eV, which is similar to the light energy with wavelength of ~ 1377 nm [32]. In the meantime, the LSPR-induced energetic electrons from Au have the sum energy of Fermi level and the incident photon [33]. Therefore, the electrons with higher energy than the Schottky barrier can be effectively separated from Au and be injected into the conduction band of the ZnO, which is called PICS [34]. However, the main contribution to the additional electrons is due to the LSPR-induced hot electrons, owing to the large energy difference between the d-band and the Fermi level (2.3 eV for Au) which requires much higher photon energy for interband excitation to overcome the Schottky barrier [35]. Moreover, plasmon-induced resonant energy transfer (PIRET) can produce the additional electrons as well, by transferring the excited LSPR energy from Au NP to the semiconductor. In other words, LSPR decays by exciting e^-h^+ pairs in the semiconductor when the LSPR resonance band overlaps with the band edge of the semiconductor [33].

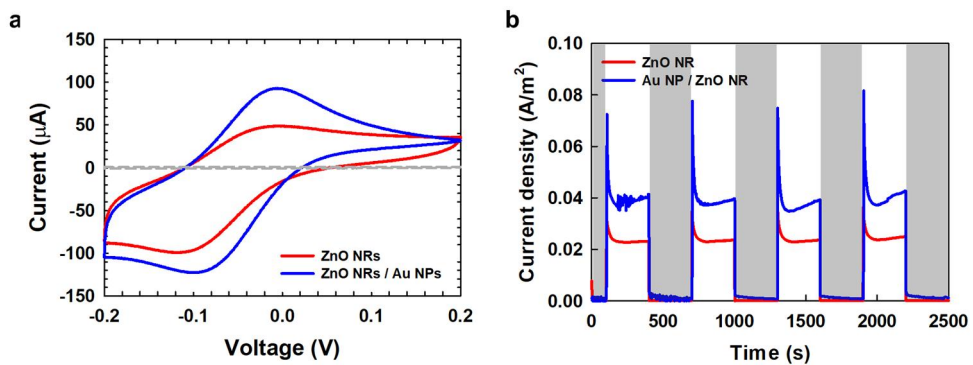


Figure 6.7 Electrochemical property of fabricated photoanode. (a) Cyclic voltammograms of the photoanode in the presence of the solution containing 50 mM potassium ferricyanide and a supporting electrolyte of 0.1 M KCl. (b) Cyclic photo-response of the photoanode measured with a 510 Ω resistance in DI water. The light irradiation started when 100 s elapsed, and the measurement was made for 300s light/dark interval.

6.3.3. Current and power analyses of the broadband multiplex living solar cell

For photo-response measurements, a device loaded with *Synechocystis* was operated at 510 Ω under alternative light and dark conditions. As a control, the device composed of an ITO glass as a photoanode was firstly examined to demonstrate the photo-activity of the *Synechocystis* (**Figure 6.8**). During light–dark cycles, the dependence of the light on the electricity generation is displayed, suggesting that *Synechocystis* is capable of transporting electron to exterior without any mediator. In contrast to PV, *Synechocystis* provide current during dark period, so-called ‘dark current’ [4]. The average dark and photo response current are about 426.4 nA and 264.4 nA, respectively. That is, *Synechocystis* enables sustainable current generation in both dark and light condition. Moreover, the intensity of the light source is appropriate for the *Synechocystis* to produce current, resulting from the stable current generation during alternative light and dark conditions.

Power output and polarization results were evaluated to characterize the performance of the electrochemical cell under light condition (**Figure 6.9**). Both curves were recorded by connecting various external resistances under the pseudo-steady state conditions [3]. We injected cell into the chamber composed of ITO electrode, ZnO NR electrode, and Au NP / ZnO NR electrode, respectively. It turned out that the anomalously amplified in performances were obtained in both two electrodes compared to that of cell /ITO. The maximum power density acquired with cell / Au NP / ZnO NR was 6.148 mW/m² under light irradiation. In addition, peak power densities of 4.178 and 0.353 mW/m² are obtained by cell / ZnO NR and cell / ITO, respectively. The results demonstrated that power density was increased by 11.8 and 17.3 times compared to that of cell /ITO.

As mentioned above, the electrons were generated in multiple paths in our broadband multiplex living solar cell. The paths include the photosynthesis of the cells, LSPR-induced hot electron injection and interband transition in ZnO NR. The

possible electron flows are represented with the arrows in a schematic energy band diagram (**Figure 6.9d**), where the midpoint redox potential of ferredoxin of the *Synechocystis* sp. and the typical energy levels of Au, ZnO and ITO were used for the energy band structure [32, 36]. With the irradiation, the photogenerated electrons in the cells can be injected into Au NP or into ZnO NR directly. Meanwhile, the LSPR-induced hot carriers in Au NP with higher energy than Schottky barrier height can be injected into the conduction band of ZnO NR and be separated efficiently through the PICS. The other path is through the direct interband excitation of valence electrons in ZnO NR. Therefore, all the electrons generated from cells and photoelectrode can be subsequently transferred to the external circuit.

The one of the main reasons for the power enhancement is pigment accumulation of photosynthetic organisms due to photoanode. *Synechocystis* have two elemental chlorophyll (Chl) pigments, mainly chlorophyll a (Chl a) and chlorophyll b (Chl b). In general, Chl a is located in Photosystem I and Photosystem II, while Chl b located within the antenna complex [9]. Chl a absorbs the violet blue - blue wavelengths of light (*ca.* 390 - 450 nm) and orange to far-red (*ca.* 600 - 700 nm), whereas Chl b absorbs violet blue to green blue light (*ca.* 390 - 500 nm) and yellow to red light (*ca.* 600 nm - 680 nm).

Generally, ZnO NR demonstrate the high light scattering effect in the full visible wavelength range (390 - 700 nm) due to its high dielectric constant and Au NP also give the far-field scattering effect. In this regard, the nanostructured photoanode can provide the enhanced light energy in the favorable spectral regions for *Synechocystis* to boost the current generation with the photosynthesis. Therefore, the far-field scattering effects by the nanostructures were investigated (**Figure 6.10**).

Figure 6.10 shows the polar plot of the far-field scattering in the overall spectral by each photoanode obtained with the measurement. It was revealed that ZnO NR basically highly enhance the light scattering in the positive z-direction and Au NP

further enhance the scattering as one of the LSPR decay mechanism. Meanwhile, bare ITO show almost negligible scattering effect compared to ZnO NR / ITO and Au NP / ZnO NR / ITO. For this reason, the hybrid plasmonic photoanode (Au NP / ZnO NR / ITO) manifested the best performance in the photocurrent generation. The scattering tendencies with respect to the wavelength were also measured to certainly confirm the working spectral range of the photoanodes for the light trapping. **Figure 6.10** verifies that the two nanostructured photoanodes are beneficial to the far-field scattering in the overall spectral range contrary to the bare ITO. For the further investigation, the whole spectra of the scattered light by the photoanodes were plotted as well (**Figure 6.11a**). Since the amount of scattering is directly affected by the light source intensity, the measured scattering intensity was divided by the light source intensity for the fair comparison between ZnO NR and Au NP / ZnO NR (**Figure 6.11b**). The results show that ZnO NR acts as the great scatterer in the full visible wavelength range and Au NP further amplify the light scattering of the incident light over the whole wavelength, especially over the preferential spectral region for the photosynthesis of the cell, as expected. Those scattering effects can be basically explained with the Mie scattering by the ZnO NR and Au NP, and the further enhancement of scattering by ZnO NR / Au NP compared to ZnO NR can be explained with LSPR-induced far-field scattering by Au NP. In the meantime, the intensity of the scattered light by the bare ITO is extremely low like the noise level, so the result is not plotted.

To compare the ability to generate electricity for each condition, the photoresponse measurements were conducted during light-dark cycles (**Figure 6.12**). A distinct difference in current generation was observed for each condition. In particular, there was a considerable difference depending on the presence or absence of cells. The photo-induced current without cell was obtained about 6.4 and 4.3 μA for Au NP / ZnO NR and ZnO NR electrodes, respectively. In the presence of cell, the photoresponse current was achieved about 12.8 and 7.3 μA for Au NP / ZnO NR and ZnO NR electrodes, respectively. It is apparently

demonstrated that hybrid structure provides benign spectral regions for *Synechocystis* to improve the current generation during photosynthesis. Moreover, our broadband multiplex living solar cell is able to generate current in the dark period, compared to other PV which are driven solely by the light period.

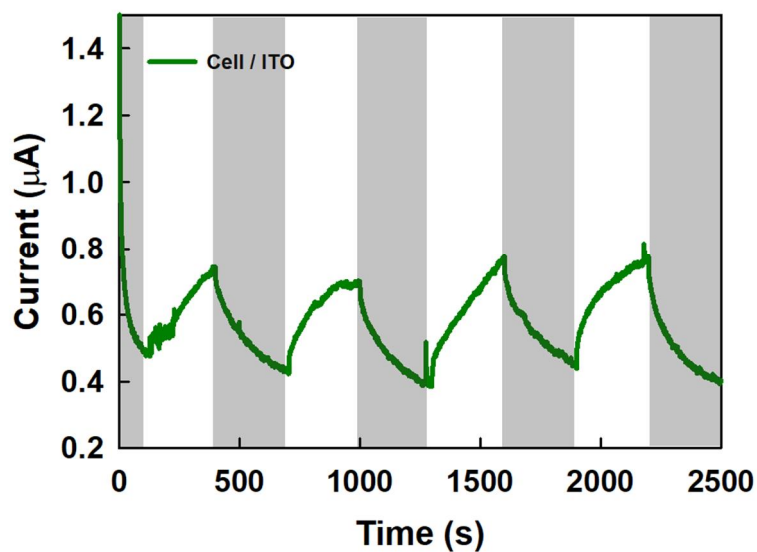


Figure 6.8 Bio-photoelectrochemical behavior of the bio-photovoltaic device loaded with *Synechocystis* sp.. Cyclic photo-response of the cyanobacteria flow cell measured with a 510 Ω resistance. The light irradiation started when 100 s elapsed, and the measurement was made for every 300s light/dark interval.

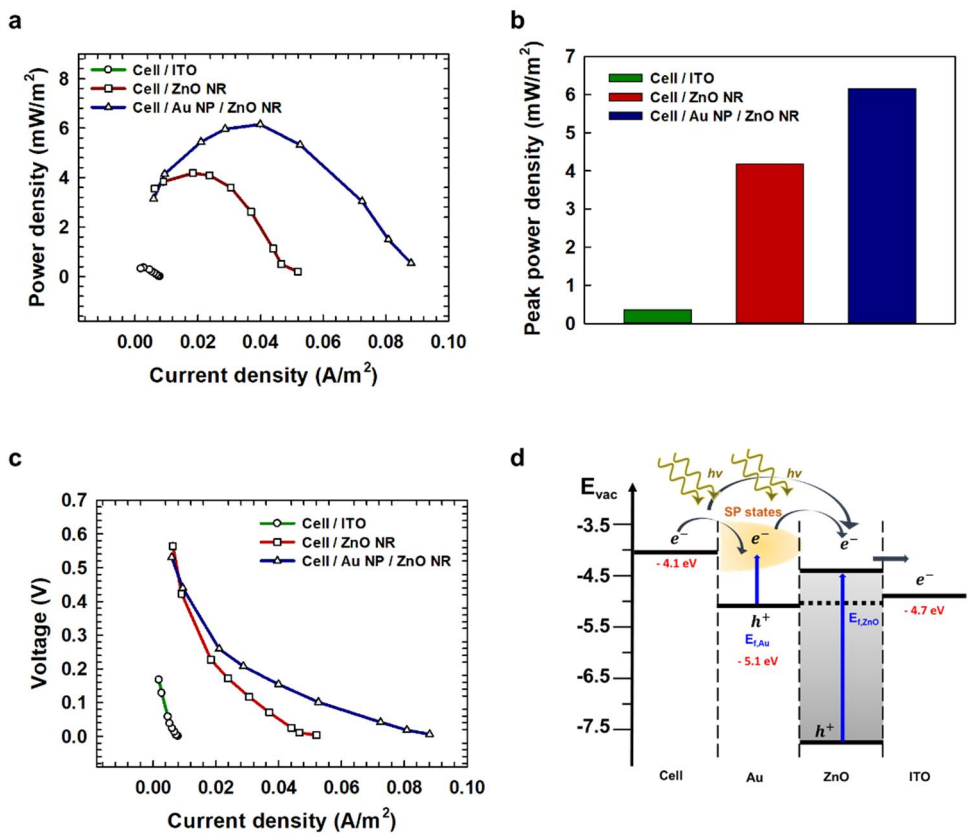


Figure 6.9 Photo-electrochemical performance of the broadband multiplex living solar cell. (a) Power density results. (b) Peak power densities of the systems. (c) Polarization curves of the device. (d) Schematic energy band diagrams of the photoanode complex for electron transfer. The arrows in the figure indicate possible flow of electrons.

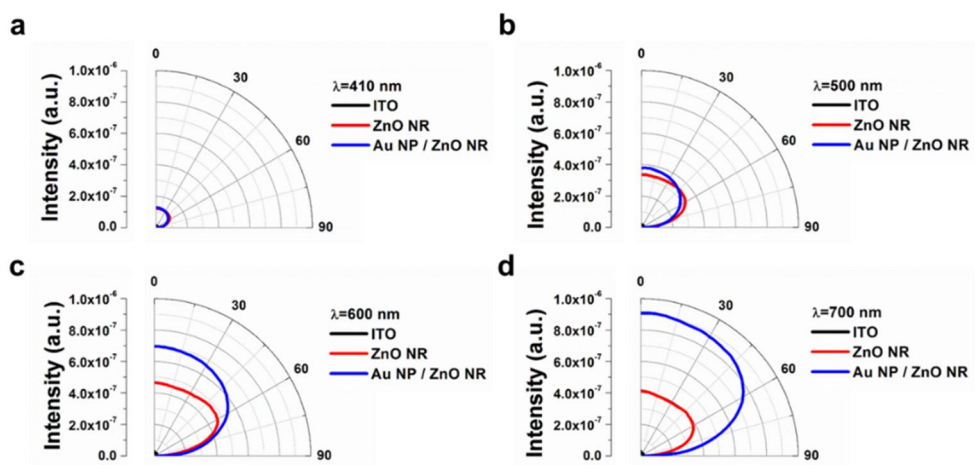


Figure 6.10 Polar plots with respect to structure and wavelength. Scattered light intensity by three different photoanode structures at the wavelength of (a) 410 nm, (b) 500 nm, (c) 600 nm and (d) 700 nm, respectively.

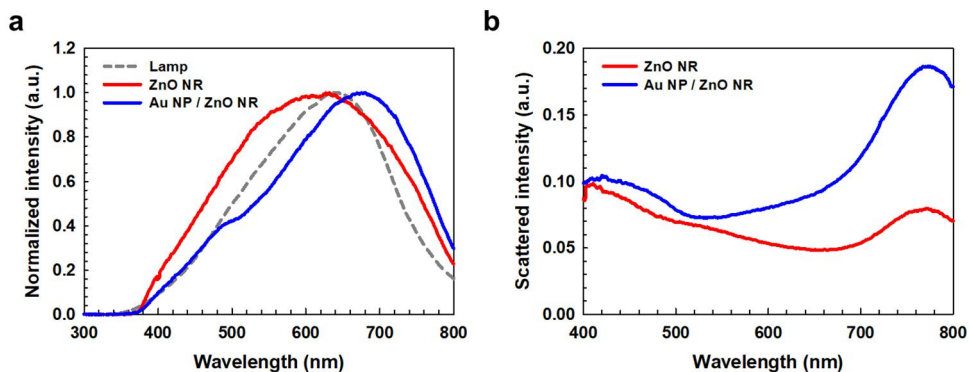


Figure 6.11 Far-field scattering effect depending on the wavelength. (a) Normalized intensity of the halogen lamp (black), and the scattered light by ZnO NR (red) and Au NP / ZnO NR (blue) with respect to the wavelength. Notice that both ZnO NR and Au NP / ZnO NR show far-field scattering effect in the full range of the light source. (b) Comparison of the scattered light intensity by Au NP / ZnO NR and ZnO NR with respect to the wavelength. The light intensity was obtained by dividing each scattered light intensity by the halogen lamp intensity at each wavelength.

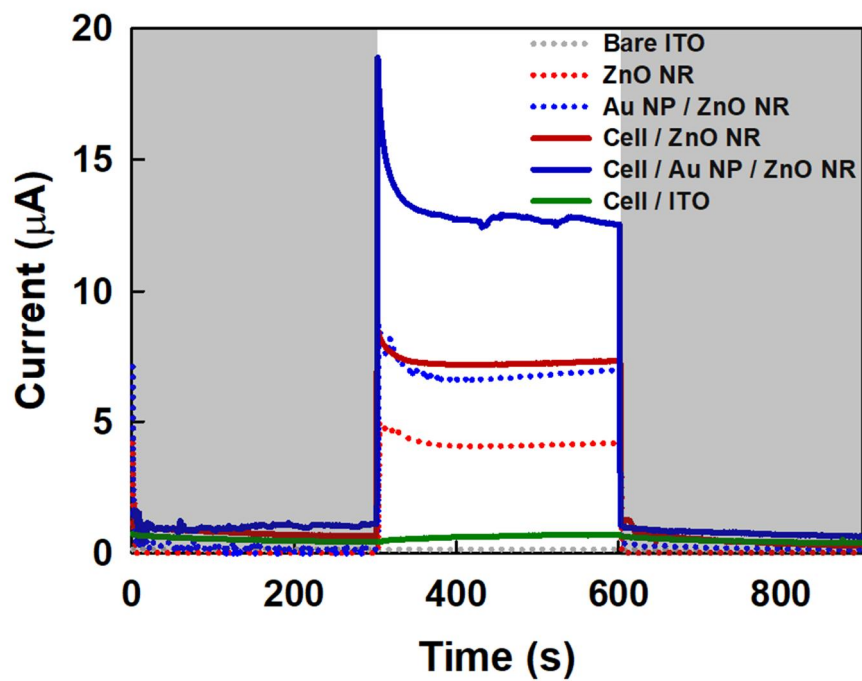


Figure 6.12 Bio-photoelectrochemical behavior of the electrochemical cell. Cyclic photo-response of the cyanobacteria flow cell measured with a 510 Ω resistance. The light irradiation started when 300 s elapsed, and the measurement was made under a 300 s light – 300 s dark cycle.

6.3.4. Viability of the *Synechocystis* onto the electrode

The viability results of both before and after the experiments are shown in **Figure 6.13**. For the viability test, the cell solution after the operation was collected. The concentration of viable cell for both before and after the experiments are is about 4×10^9 and 3.6×10^9 cells/ml, respectively. There is not a statistically significant difference between the groups ($P = 0.066$). Moreover, the device was disassembled and the electrode was gently washed for post analysis. The fluorescent image is obtained from the cell onto the electrode after the operation. The result shows that cells are widely covered by the surface of the electrode. In other words, it is demonstrated that cell is viable onto the photoanode after the operation. Since the gap between individual ZnO NR (less than 500 nm) is a diminutive area, cell (1 - 2 μm) did not penetrate into the electrode, indicating that the contamination of cell is not occurred (**Figure 6.14**) [7].

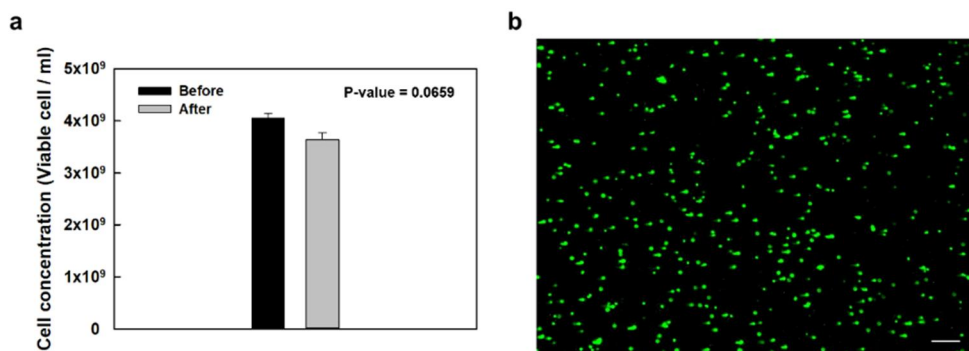


Figure 6.13 Viability test. (a) Concentration of viable cell. There is not a statistically notable difference between two groups. (b) A fluorescent optical image of the *Synechocystis* on the Au NP / ZnO NR electrode after an operation. Scale bar denotes 10 μm .

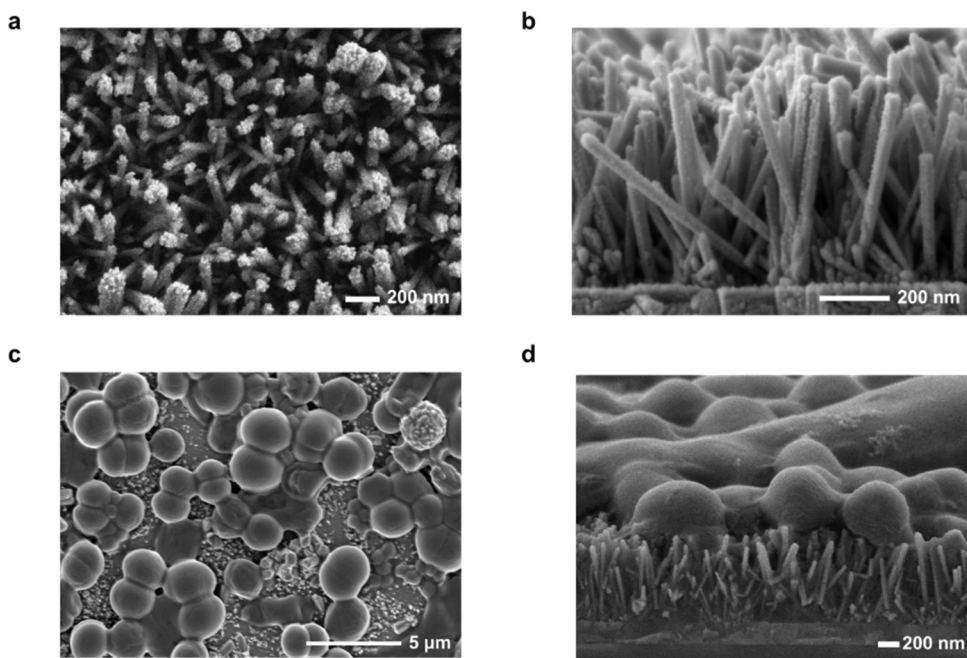


Figure 6.14 SEM image of the electrodes utilized in this experiments. SEM image of the Au NP / ZnO NR on the ITO substrate: (a) top view (b) side view. SEM image of the cell / Au NP / ZnO NR nanowires on the ITO substrate: (c) top view (d) side view. The bacteria thrives onto the electrode.

6.3.5. Broadband multiplex living solar cell

In the meantime, the working spectral range of the light source is different for each path due to the different origin of the photogenerated electrons. The schematic diagram in **Figure 6.15** exhibits the working mechanisms with respect to the wavelength. As expected with the strategy, our combined system is being activated at almost full spectrum of the light source including ultraviolet and visible ranges by utilizing both biophotovoltaic and photovoltaic effects simultaneously. To sum up the diagram, *Synechocystis* is actively working at the two favorable visible regions (390 - 500 nm and 600 - 700 nm) due to the two elemental chlorophyll (Chl) pigments. The photosynthetic activity is exceptionally enhanced, aided by the light trapping and the far-field scattering throughout the suspended cells by the hybrid plasmonic photoanode. Moreover, ZnO NR and Au NP harvest the light energy at the ultraviolet region (below 364nm) and the *Synechocystis*-inactive visible region (around 520 nm) through the interband excitation and the Landau damping of LSPR, respectively.

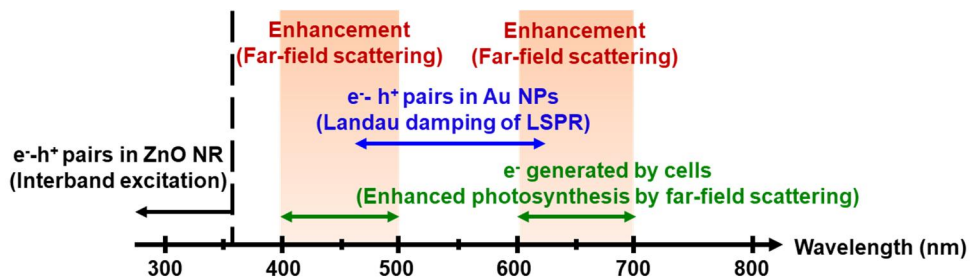


Figure 6.15 Broadband multiplex living solar cell. The schematic diagram describing the working mechanisms of the hybrid plasmonic photoanode for the electron generation with respect to the wavelength.

6.4. Conclusion

In this study, we suggest a novel light harvester that consists of *Synechocystis* and Au NP / ZnO NR. The robust photoactivity of *Synechocystis* was achieved with bi-functional electrode containing Au NP / ZnO NR by accumulating favorable spectral region for the photosynthesis. In our system, the performance of living solar cell was extensively enlarged by both biophotovoltaic and photovoltaic effects. ZnO NR enhanced the light scattering in the positive z-direction where the cell is placed. In addition, Au NP further lift the far-field scattering aided by the LSPR effect. Moreover, the viability test confirmed that cell is viable onto the electrode even after operation. This unprecedented hybrid system would enable to introduce a new pathway of enhanced performance of the biophotovoltaics.

6.5. Bibliography

- [1] D.J. Lea-Smith, P. Bombelli, R. Vasudevan, C.J. Howe, *Biochimica et Biophysica Acta (BBA)-Bioenergetics*, 1857 (2016) 247-255.
- [2] K.L. Saar, P. Bombelli, D.J. Lea-Smith, T. Call, E.-M. Aro, T. Müller, C.J. Howe, T.P. Knowles, *Nature Energy*, 3 (2018) 75.
- [3] Min Jung Kim, Seoung Jai Bai, Jae Ryouon Youn, Young Seok Song, *Journal of Power Sources*, 412 (2019) 201-310.
- [4] P. Bombelli, M. Zarrouati, R.J. Thorne, K. Schneider, S.J. Rowden, A. Ali, K. Yunus, P.J. Cameron, A.C. Fisher, D.I. Wilson, *Physical Chemistry Chemical Physics*, 14 (2012) 12221-12229.
- [5] P. Bombelli, T. Müller, T.W. Herling, C.J. Howe, T.P. Knowles, *Advanced energy materials*, 5 (2015) 1401299.
- [6] N. Sekar, Y. Umasankar, R.P. Ramasamy, *Physical Chemistry Chemical Physics*, 16 (2014) 7862-7871.
- [7] F. Qian, H. Wang, Y. Ling, G. Wang, M.P. Thelen, Y. Li, *Nano letters*, 14 (2014) 3688-3693.
- [8] M.D. Ooms, Y. Jeyaram, D. Sinton, *Applied Physics Letters*, 106 (2015) 063902.
- [9] E. Eroglu, P.K. Eggers, M. Winslade, S.M. Smith, C.L. Raston, *Green Chemistry*, 15 (2013) 3155-3159.
- [10] H.D. Amrei, R. Ranjbar, S. Rastegar, B. Nasernejad, A. Nejadbrahim, *Journal of applied phycology*, 27 (2015) 67-74.
- [11] N. Zhang, C. Han, X. Fu, Y.-J. Xu, *Chem*, (2018).
- [12] R. Gao, Z. Liang, J. Tian, Q. Zhang, L. Wang, G. Cao, *RSC Advances*, 3 (2013) 18537-18543.
- [13] V. Strano, E. Smecca, V. Depauw, C. Trompoukis, A. Alberti, R. Reitano, I. Crupi, I. Gordon, S. Mirabella, *Applied Physics Letters*, 106 (2015) 013901.
- [14] J.T.D. Ty, H. Yanagi, *Japanese Journal of Applied Physics*, 54 (2015) 04DK05.
- [15] C. Clavero, *Nature Photonics*, 8 (2014) 95.
- [16] S. Mubeen, J. Lee, W.-r. Lee, N. Singh, G.D. Stucky, M. Moskovits, *ACS nano*, 8 (2014) 6066-6073.
- [17] A. Dabirian, N. Taghavinia, *ACS applied materials & interfaces*, 7 (2015) 14926-14932.
- [18] W.R. Erwin, H.F. Zarick, E.M. Talbert, R. Bardhan, *Energy & Environmental Science*, 9 (2016) 1577-1601.
- [19] M. Wu, W.-J. Chen, Y.-H. Shen, F.-Z. Huang, C.-H. Li, S.-K. Li, *ACS applied materials & interfaces*, 6 (2014) 15052-15060.
- [20] H.M. Kim, J.R. Youn, Y.S. Song, *Nanotechnology*, 27 (2016) 085704.
- [21] V. Perumal, U. Hashim, S.C. Gopinath, R. Haarindraprasad, K. Foo, S. Balakrishnan, P. Poopalan, *Scientific reports*, 5 (2015) 12231.
- [22] J. Guo, J. Zhang, M. Zhu, D. Ju, H. Xu, B. Cao, *Sensors and Actuators B: Chemical*,

199 (2014) 339-345.

[23] S. Kahraman, H. Çakmak, S. Çetinkaya, F. Bayansal, H. Çetinkara, H. Güder, *Journal of Crystal Growth*, 363 (2013) 86-92.

[24] X. Wang, X. Zhang, W. Cheng, H. Shao, X. Liu, X. Li, H. Liu, J. Wu, *Nanoscale research letters*, 9 (2014) 109.

[25] F. Xiao, F. Wang, X. Fu, Y. Zheng, *Journal of Materials Chemistry*, 22 (2012) 2868-2877.

[26] E.H. Umukoro, M.G. Peleyeju, A.O. Idris, J.C. Ngila, N. Mabuba, L. Rhyman, P. Ramasami, O.A. Arotiba, *RSC Advances*, 8 (2018) 10255-10266.

[27] Z. Kang, X. Yan, Y. Wang, Y. Zhao, Z. Bai, Y. Liu, K. Zhao, S. Cao, Y. Zhang, *Nano Research*, 9 (2016) 344-352.

[28] Z. Kang, X. Yan, Y. Wang, Z. Bai, Y. Liu, Z. Zhang, P. Lin, X. Zhang, H. Yuan, X. Zhang, *Scientific reports*, 5 (2015) 7882.

[29] M. Wang, L. Sun, Z. Lin, J. Cai, K. Xie, C. Lin, *Energy & Environmental Science*, 6 (2013) 1211-1220.

[30] C. Jia, X. Li, N. Xin, Y. Gong, J. Guan, L. Meng, S. Meng, X. Guo, *Advanced Energy Materials*, 6 (2016) 1600431.

[31] P. Reineck, D. Brick, P. Mulvaney, U. Bach, *The journal of physical chemistry letters*, 7 (2016) 4137-4141.

[32] T. Bora, H.H. Kyaw, S. Sarkar, S.K. Pal, J. Dutta, *Beilstein journal of nanotechnology*, 2 (2011) 681.

[33] S.K. Cushing, N. Wu, *The Electrochemical Society Interface*, 22 (2013) 63-67.

[34] T. Tatsuma, H. Nishi, T. Ishida, *Chemical science*, 8 (2017) 3325-3337.

[35] L. Wu, G.M. Kim, H. Nishi, T. Tatsuma, *Langmuir*, 33 (2017) 8976-8981.

[36] H. Bottin, B. Lagoutte, *Biochimica et Biophysica Acta (BBA)-Bioenergetics*, 1101 (1992) 48-56.

Korean Abstract

태양 에너지는 환경오염 배출이 없는 대표 재생에너지원으로 기존 화석 연료에 대한 실질적인 대체 에너지원이다. 이와 관련하여, 광합성 유기체를 이용하여 빛 에너지를 전기 출력으로 변환하는 생물학적 광전변환 시스템(BPV)이 최근 친환경 기술로 주목받고 있다. 그러나 지금까지 연구된 생물학적 광전변환 시스템은 낮은 효율성에 머물렀다. 본 연구에서는 바이오유변학 지식에 기반한 다양한 생물학적 광전변환 시스템을 설계함으로써 기존 시스템의 한계를 극복하고자 하였다.

생물학적 광전변환 시스템에 대한 예비 연구인 바이오유변학 시스템은 2장과 3장에 기술하였다. 2장에서 광전변환 시스템에 사용할 적절한 세포를 선택하기 위해 체외고분자물질(EPS)을 사용하여 광합성 유기체를 조작하는 방법을 제시하였다. 우리는 광합성 유기체로부터 체외고분자물질을 추출하고 제한된 미세 유체 장치에서 세포 집중과 크기에 따른 분리를 통해 체외고분자물질의 비뉴턴 유변학적 특성을 연구했다. 세포는 '자체 분비된 물질'에서 '자가 정렬'을 보였으며, 자발적인 분류가 실험적으로 확인되었다. 3장에서 빛에 의한 점도 조작의 새로운 가능성을 제시하는 광합성 유기체의 광 유변학을 소개하였다. 광합성 유/무에 따라 광합성 유기체의 표면 물성 변화를 제타 전위 측정, 임피던스 분석을 통해 확인했으며 결과를 콜로이드 이론에 적용하여 점도와의 연관성을 밝혔다. 광합성은 용액 중 세포의 유효 위상 부피를 증가시켜 분산에 직접적인 영향을 주었고 세포 용액의 점도 증가를 유발하였다.

4장에서는 바이오유변학 지식에 기초한 생물학적 흐름 전지를 설계 및 제작하였다. 이는 지속 가능한 방식으로 광합성 유기체를 사용하여

태양 에너지를 전환하는 새로운 방향을 제시한다. 시아노박테리아의 광합성 활성은 탄산수소 이온을 사용하여 조절하였고, 전기 화학 에너지를 포함하는 세포 현탁액은 유동 시스템을 통해 순환시켰다. 이것은 세포의 신진대사를 조작함으로써 생태 친화적인 에너지 전환 시스템을 구현할 수 있다는 점에서 주목할만하다.

생물학적 광전변환 시스템의 성능을 향상하기 위해 5, 6장에서는 바이오 - 무기 복합체가 도입된 광전변환 시스템을 설계하였다. 5장에서는 높은 발전 성능을 위해 전극에 긴 전자 전달 도관을 생성하고자 *Synechococcus* sp. - 철 산화물 나노 입자 - 네오디뮴 철 붕소 자석 촉물을 설계하였다. 이것은 자체 제작된 전자 전달 통로뿐만 아니라 전자 생산 통로 역할을 하였고 약 1.653%의 효율을 가지며 상용 녹색 LED 전구를 켤 수 있었다. 6장에서는 *Synechocystis* sp. / 금 나노 입자 (Au NP) / 산화 아연 나노 로드 (ZnO NR) / ITO 로 구성된 광대역을 사용하는 바이오 - 무기 복합체 광전변환 시스템을 제안하였다. 하이브리드 나노 구조 (Au NP / ZnO NR)는 광대역 영역에서 원거리 산란 효과를 통해 세포의 광합성 기작을 자극함으로써 기존보다 약 17.3배 증폭된 변환 성능을 유도하였다.

본 학위 논문에서 수행한 연구들은 생물학적 광전변환 시스템의 새로운 접근 방법을 제안하며 지속 가능한 에너지 하베스팅의 가능성을 제시한다.

주요어: 바이오유변학적 시스템, 광합성 유기체, 점탄성 유체, 미세 유체 공학, 광 유변학, 생물학적 광전변환 시스템 (BPV), 생물학적 흐름 전지, 바이오 - 무기 복합체

학 번: 2014-31051